UNIVERSITY OF CALIFORNIA, SAN DIEGO

Nanomaterials Design

for Thermal Energy Conversion Technologies

A dissertation submitted in partial satisfaction of the

requirements for the degree Doctor of Philosophy

in

Materials Science and Engineering

by

Jaeyun Moon

Committee in Charge:

Professor Renkun Chen, Chair
Professor Sungho Jin, Co-Chair
Professor Ami Berkowitz
Professor Ratneshwar Lal
Professor Jie Xiang

2014

The dissertation of Jaeyun Moon is approved, and it is acceptable in quality and form for publication on microfilm:

Co-Chair

Chair

University of California, San Diego

2014

DEDICATION

Dedicated to my loving parents and family

who have always shown unfailing love and support

TABLE OF CONTENTS

LIST OF FIGURES

LIST OF TABLES

ACKNOWLEDGEMENTS

I would like to express the deepest appreciation to my committee chair Professor Renkun Chen for teaching and supporting me during my graduate studies. I have learned from him not only the scientific knowledge but also how to think like scientists and how to be self-motivated and self-inspired. He continually and convincingly conveyed a spirit of adventure in regard to research and scholarship. Without his guidance and persistent help this dissertation would not have been possible.

I truly appreciate Professor Sungho Jin for providing me all the valuable advice and guidance as my co-advisor. He has provided a bright vision and encouraged me to be a passionate scientist.

I also would like to thank my committee members, Prof. Sungho Jin, Prof. Ami Berkowitz, Prof. Ratnesh Lal, Prof. Jie Xiang for helpful discussions and suggestions on my dissertation.

I am also really grateful to Prof. Sungho Jin, Prof. Zhaowei Liu, Justin(Tae Kyoung Kim) and Bryan VanSader for the collaboration work on solar thermal project. It has been a great experience working on a challenging project with smart and passionate people. I also deeply appreciate to Prof. Jie Xiang and Dr. Ji-Hun Kim for the successful collaboration on nanowire thermoelectrics and to Prof. Ami Berkowitz and Phi Nguyen for the great collaboration on thermoelectric nanocomposites. I have learned not only lots of knowledge and experiment skills from valuable discussions with them but also the joy

of working together. I feel extremely fortunate and privileged to have worked with all of my colleagues in UC San Diego.

I am indebted to all of Chen's group members, Matt Wingert, Edward Dechaumphai, Jianlin Zheng, Sahngki Hong and Shuang Cui, who are really good friends of mine as well as my labmates. It was a great pleasure discussing and working with them. They will always remain dear to me.

Completing my PhD degree is probably the most challenging activity of my life so far. The best and worst moments of my doctoral journey have been shared with many people. It has been a great joy to spend several years with my good friends in UC San Diego. I would truly like to thank: Dr. Sunyoun Noh, Guipeun Kang, Joohwan Kim, Geuntak Lee, Dr. Jinkyu Han, Sejung Kim, Joonhong Park, Kimoon Um, Yoona Kim, Jihye Baek, Youngjin Kim, Sungje Byun, Asuelim Kim, Sungwoon Kim, Hyojung Yoon, Tae Kyoung Kim, Dr. Chulmin Choi, and Dr. Yongsung Hwang in UC San Diego. My friends in Korea, Hami Lee Mihyun Kang, Soyoung Hong and other friends from Hanyang University deserve my sincerest thanks. Their friendship and assistance have meant more to me than I could ever express. My friends from high school, Jihyun Ha, Joohee Kim, Jaeyoung Ahn, Sungsin Park and Jeongpil Byun were sources of laugher, joy and support during the past few years.

Lastly, I cannot express my gratitude and love enough for my parents, my brother, my sister-in-law and lovely niece Jay. Without their unlimited love, support and prayer, I would not be here.

Chapter 2, in full, is a reprint of the material as it appears in *Nano Letters*, Volume 13, 2013. Jaeyun Moon, Ji-Hun Kim, Zack C.Y. Chen, Jie Xiang and Renkun Chen. The dissertation author was the primary researcher and first author of this paper.

Chapter 3, in full, is a reprint of the material as it is in press in *Nano Energy*. Jaeyun Moon*, Dylan Lu*, Bryan VanSaders, Tae Kyoung Kim, Seong Deok Kong, Sungho Jin, Renkun Chen and Zhaowei Liu. The dissertation author was the primary researcher and first author of this paper.

Chapter 4, in full, is currently being prepared for submission for publication in *Advanced Energy Materials*. Jaeyun Moon*, Tae Kyoung Kim*, Bryan VanSader*, Chulmin Choi, Zhaowei Liu, Sungho Jin, and Renkun Chen. The dissertation author was the primary researcher and first author of this paper.

VITA

1999 Bachelor of Engineering in Materials and Metallurgical Engineering, Hanyang University, Republic of Korea

2001 Master of Engineering in Materials Science and Engineering, Hanyang University, Republic of Korea

2014 Doctor of Philosophy in Materials Science and Engineering, University of California, San Diego

LIST OF PUBLICATIONS

1. Edward Dechaumphai, **Jaeyun Moon**, Matthew C. Wingert, Renkun Chen, "Phononic and Electronic Engineering in Nanowires for Enhanced Thermoelectric Performance" in *Semiconductor Nanowires: From Next-Generation Electronics to Sustainable Energy*, Royal Chemistry of Society, London, UK (In press, 2014)

2. **Jaeyun Moon**, Dylan Lu, Bryan VanSaders, Tae Kyoung Kim, Seong Deok Kong, Sungho Jin, Renkun Chen, Zhaowei Liu, "High Performance Multi-scaled Nanostructured Spectrally Selective Coating for Concentrated Solar Power" *Nano Energy* 8 238-246 (2014)

3. **Jaeyun Moon**, Tae Kyoung Kim, Bryan VanSaders, Chulmin Choi, Zhaowei Liu, Sungho Jin, Renkun Chen, "Black Oxide Nanoparticles as Durable Solar Absorbing Material for High-Temperature Concentrating Solar Power System", *Advanced Energy Materials* (Submitted, 2014)

4. Tae Kyoung Kim, **Jaeyun Moon**, Bryan VanSaders, Dong Won Chun, Jae-Young Jung, Gang Wang, Renkun Chen, Zhaowei Liu, Yu Qiao, Sungho Jin, "Si-Si Boride Core-Shell Nanoparticles with Improved Oxidation Resistance for High Temperature Applications", *Nano Energy* (Accepted, 2014).

5. Edward Dechaumphai, Dylan Lu, Jimmy J. Kan, **Jaeyun Moon**, Eric E. Fullerton, Zhaowei Liu, Renkun Chen, "Ultralow Thermal Conductivity of Multilayers with Highly Dissimilar Debye Temperatures", *Nano Letters* 14 (5) 2448–2455 (2014)

6. Edward Dechaumphai, Joseph L. Barton, Joseph R. Tesmer, **Jaeyun Moon**, Yongqiang Wang, George R. Tynan, Russell. P. Doerner, Renkun Chen "Near-Surface Thermal Characterization of Plasma Facing Components Using the 3-omega Method", *Journal of Nuclear Materials* 455(1) 56-60 (2014)

7. **Jaeyun Moon**, Ji-Hun Kim, Zack C.Y. Chen, Jie Xiang, Renkun Chen, "Gate-Modulated Thermoelectric Power Factor of Hole Gas in Ge–Si Core–Shell Nanowires", *Nano Letters* 13 1196–1202 (2013).

8. Phi K. Nguyen, K H Lee, **Jaeyun Moon**, S I Kim, K A Ahn, L H Chen, S M Lee, R K Chen, S Jin, A E Berkowitz "Spark erosion: a high production rate method for producing $Bi_{0.5}Sb_{1.5}Te_3$ nanoparticles with enhanced thermoelectric performance", *Nanotechnology* 23 415604 (2012).

9. Matthew C. Wingert, Zack C. Y. Chen, Edward Dechaumphai, **Jaeyun Moon**, Ji-Hun Kim, Jie Xiang, Renkun Chen, "Thermal Conductivity of Ge and Ge–Si Core–Shell Nanowires in the Phonon Confinement Regime", *Nano Letters,* 11 5507–5513 (2011).

10. Chang Huhn Lee, **Jaeyun Moon**, Kyu Whan Chong, Hyung Dong Woo, Seog Hee Kang, Kyung Seok Oh, Seok Woo Hong, Jae Cheol Lee, "Novel Methods for Identification and Analysis of Various Yield Problems in Semiconductor Manufacturing", *Advanced Semiconductor Manufacturing Conference* 185-190 (2006).

11. **Jaeyun Moon**, Hanshin Choi, Hyungjun Kim, Changhee Lee, "The effects of heat treatment on the phase transformation behaviors of plasma-sprayed stabilized zirconia thermal barrier coating", *Surface and coatings technology* 155 1-10 (2002).

12. **Jaeyun Moon**, Hanshin Choi, Changhee Lee, "Cooling rate effect on phase transformation of plasma sprayed partially stabilized zirconia", *Journal of materials science letters* 20 1611-1613 (2001).

ABSTRACT OF THE DISSERTATION

Nanomaterials Design

for Thermal Energy Conversion Technologies

by

Jaeyun Moon

Doctor of Philosophy in Materials Science and Engineering

University of California, San Diego, 2014

Professor Renkun Chen, Chair

Professor Sungho Jin, Co-Chair

Climate change is mainly caused by carbon dioxide emission, at least 90% of which results from the fossil fuel consumption to meet the world's growing energy need. Hence, development and deployment of renewable energy is of paramount importance and becoming increasingly urgent for human society. Recently, the utilization of thermal energy conversion technologies is gradually prevailing for clean energy production due to their unique functions, such as dispatchability. In this thesis, advanced nanostructured materials for applications in two thermal energy conversion technologies, thermoelectrics and concentrating solar power, are discussed. The approaches to improve materials'

functionalities pertaining to these two technologies are proposed and experimentally demonstrated.

Semiconductor nanowires have been attractive as efficient thermoelectric materials, since small diameter of nanowires induces phonon-boundary scattering to reduce thermal conductivity. Also low-dimensional quantum confinement effect has been predicted to drastically increase the power factor. In Chapter 2 of the thesis, thermoelectric power factor of intrinsic Ge-Si core-shell nanowires is investigated. The nanowires consist of intrinsic Ge core and Si shell, however, free holes are accumulated inside the Ge core due to the Fermi level pinning effect at the epitaxial core-shell interface.. This unique doping mechanism avoids the introduction of ionized dopants while obtaining a sufficiently high electrical conductivity. As a result, it provides an opportunity to enhance the carrier mobility with reduced ionized impurity scattering. The carrier concentration in core/shell nanowires has also been readily controlled by a gate voltage in a field effect transistor configuration. The field effect modulation allows one to conveniently probe the thermoelectric properties within a wide range of carrier concentrations without the use of chemical doping. The Seebeck coefficient of nanowires follows the behavior of bulk Ge as the Ge core diameter reduces down to 11nm. Based on these results, the power factor is strongly related to carrier mobility, which is enhanced in the Ge-Si nanowires compared to the bulk Ge .

In Chapter 3 and 4, solar absorbing materials for Concentrating Solar Power (CSP) are discussed. CSP is becoming a significant renewable energy technology around the world, and yet the cost reduction is still needed in order to compete with traditional power plants. As higher operating temperature leads to higher energy conversion

efficiency and cost reduction, the development of high temperature CSP system has been actively pursued. With regards to CSP receivers, light absorbing coatings and spectrally selective coatings (SSCs) of solar receivers are a critical component enabling high-temperature and high-efficiency operation of CSP systems.

In Chapter 3, a multi-scaled approach is employed to efficiently improve the light absorption. To demonstrate the feasibility of the fractal nanostructures, semiconductor powders with particle sizes ranging from ~10 nm to ~10 μm are fabricated using a spark erosion process, which is a scalable power production method. Optical measurement results on the multi-scaled structure show high solar absorptivity (~90-95%) and <30% infrared emissivity near the peak of 500℃ black body radiation.

In Chapter 4, black oxide cobalt oxide nanoparticles are synthesized via hydrothermal process and employed as a light absorbing material for the high-temperature CSP receivers. The black oxide nanopowders are embedded in SiO_2 dielectric matrix. The surface texturing is created by utilizing sacrificial polymer stamps and beads. All of the coating samples are fabricated using a scalable spray coating method. The thermal absorption efficiency of the cobalt oxide layers is ~ 88.2% and ~85.4% for coatings with and without the textured surface respectively. Furthermore, the performance of coating shows no degradation after a long-term(1000-hour) aging test at 750 ^{o}C in air. These results point out that the cobalt oxide light absorbing coatings with surface texturing via a scalable process can be readily applicable for future high temperature CSP systems.

CHAPTER 1 : Introduction - Principles of Thermal Energy Conversion Technologies

Global warming is now almost universally accepted as a serious problem caused by human activities, mainly burning fossil fuels. World power demand is expected to increase up to 30TW by 2050 from the current power consumption ~16TW in 2010. Approximately 90% of the world's power is generated by consuming fossil fuels or from nuclear reactions. It has become increasingly obvious that carbon dioxide gases (greenhouse gases) produced from burning fossil fuel is the cause of the global warning.[1] Therefore, a lot of efforts for coming up with the solutions to the problem. By understanding the fundamentals of energy conversion between different forms of energy, such as nuclear energy, chemical energy, electromagnetic energy, mechanical energy, thermal energy and electrical energy, the suitable and efficient technologies can be developed. Recently, thermal energy utilization has been considered to be an important part of renewable energy, because there are numerous types of heat energy, such as geothermal energy and solar thermal energy. In addition, since the most of power plants are thermal power stations and a large portion of energy was lost during energy generation, the waste heat recovery is also an important issue.

Among various renewable energy resources, solar energy is by far the largest exploitable natural resource because the solar energy irradiating the surface of the Earth (1.3×10^5 TW) is huge and exceeds the current global human energy consumption ($1.6 \times$

10^{1} TW in 2010) [2]. There are two main technologies to convert solar energy to electricity: one is photovoltaic solar cell and the other is concentrating solar power (CSP). The CSP utilizes solar heat energy to run turbine engines in thermal power plants instead of burning fossil fuels.

In this section, the introduction of the thermoelectrics (in 1.1) and the CSP technology (in 1.2) will be briefly given, including a conventional thermoelectric history, a limitation of conventional thermoelectrics, recent research trends and CSP system configuration, advantages and disadvantages of CSP.

1.1 Overview of Thermoelectrics

1.1.1 History and Applications of Thermoelectrics

Thermoelectrics is a solid state physics technology to convert heat to electricity or reversely to heat up or cool down using electricity. According to 'Estimated U.S. energy Use in 2013', approximately ~60% of total energy has been wasted by a heat during electricity generation in thermal power plants or a transportation. [3] In order to solve green gases and global warming problems, thermoelectric technology can play an important role by recovering waste heat from transportation, industrial use and energy generation process, thus leading to reduce the consumption of fossil fuels which is the major source of CO_2 emission. Furthermore, thermoelectric can be used to directly harvest the Sun's energy via solar thermoelectrics. While the traditional solar thermal technology produces electricity from a heat by using heat engines, the solid state heat engines consisting of thermoelectric generators convert a temperature gradient induced by the Sun to electrical

power[4-7]. Since the amount of solar energy is immense, the application of solar thermoelectrics is also a promising approach.

The phenomenon of thermoelectricity has been known as Seebeck, Peltier and Thomson effects, which were discovered in the early 1800s. In the 1950s, the research and development of bulk homogeneous thermoelectric materials began and led to a commercial thermoelectric power generation and cooling devices. [8] From 1920~1970, the study of thermoelectricity was applied for use in valuable technologies, primarily cooling as well as power generation. However, by the end of the 1960's the progress had slowed with some discussion that the upper limit of the figure of merit, ZT, might be near 1 and many research programs were dismantled.

In early 1990s, Hicks and Dresselhaus pioneered the idea that quantum confinement of carriers in low-dimensional materials could dramatically improve the thermoelectric figure of merit ZT by controlling power factor ($S^2\sigma$)[9, 10]. Although these two papers triggered active research of nanostructured thermoelectric materials, many achievements of the thermoelectric performance improvement were caused by reducing lattice thermal conductivity. Therefore, there are still many discussions about the low dimensionality and nanostructures for a quantum confinement effect could play in improving thermoelectrics. High performances (ZT>1) in thermoelectrics with quantum dot structures, hierarchical thermoelectric materials and nanostructured thermoelectric materials have been reported and ZT_{max} trend in last decades is shown in Figure 1.1. As Figure 1.1 demonstrated, the recent improvements were obtained by nanostructuring of thermoelectric materials. For example, the nanostructured BiSbTe that is a traditional

thermoelectric material improved ZT from ~1.0 to ~1.4 and the hierarchical structure of PbTe has recently exhibited a large enhancement of ZT by ~2.2.

Besides bulk thermoelectrics, the semiconductor nanowire-based thermoelectrics have been considered to be attractive thermoelectric materials, because the low thermal conductivity of nanowires induced by phonon- boundary scattering provides a good opportunity for high thermoelectric performance. In 2008, Hochbaum and Chen have reported that rough Si nanowires could remarkably reduce the thermal conductivity and Si nanowires became attractive as a promising thermoelectric material.

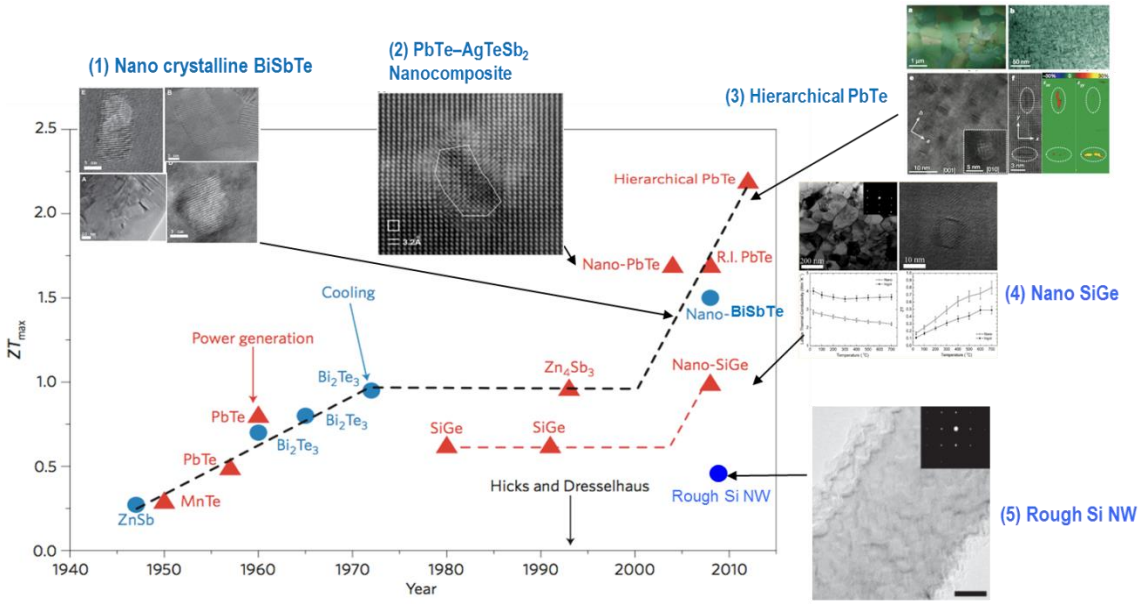

Figure 1.1 ZT_{max} trend of nanostructured thermoelectric materials (1)Nano crystalline BiSbTe[11] (2)PbTe-AbTeSb$_2$ Nanocomposite[12] (3) Hierarchical PbTe[13] (4) Nano SiGe[14] and (5) Rough SiNWs [15](copyright AAAS [11, 12], Nature Publishing Group[13, 15], American Chemical Society[14])

Even though the thermoelectrics efficiency was not sufficient to replace a conventional heat engines and refrigerators, the reliability and simplicity (no mechanical parts) of thermoelectricity have enabled niche applications, such as a power generation

for space probes[16], a waste heat recovery in automobiles[17] and in energy industrial processes to electronic cooling and heating[18].

1.1.2 The figure of merit, ZT, and TE efficiency

Thermoelectric materials are generally evaluated using the dimensionless figure of merit ZT which is given by the following equation.

$$ZT = \frac{S^2 \sigma T}{\kappa} \qquad (1.1)$$

where S is the Seebeck coefficient (thermopower), σ is the electrical conductivity, κ is the thermal conductivity and T is the absolute temperature. The Seebeck coefficient S is a material property and defined as the magnitude of the created thermo voltage in a material with a temperature gradient. A high electrical conductivity is required to avoid Joule heating, while a low thermal conductivity maintains a large temperature gradient. For conventional thermoelectric materials, the ZT is ~1 at T=300K. Since the ZT is strongly related to power generation efficiency, a higher ZT leads to a higher overall efficiency of energy conversion. The relation between ZT and thermoelectric efficiency is shown as the following equation.

$$\eta_{TE} = \frac{(T_H - T_C)(\sqrt{1+ZT_{avg}}+1)}{T_H\left(\sqrt{1+ZT_{avg}} - {T_C}/{T_H}\right)} = \eta_C \frac{(\sqrt{1+ZT_{avg}}+1)}{\left(\sqrt{1+ZT_{avg}} - {T_C}/{T_H}\right)} \qquad (1.2)$$

where η_{TE} is thermoelectric efficiency, η_C is Carnot efficiency, T_C is the cold and T_H is the hot temperature at the end of the sample and T_{avg} is defined as $(T_H-T_C)/2$.[19] Figure 1.3 clearly shows a significance of the figure of merits to improve thermoelectric efficiency.

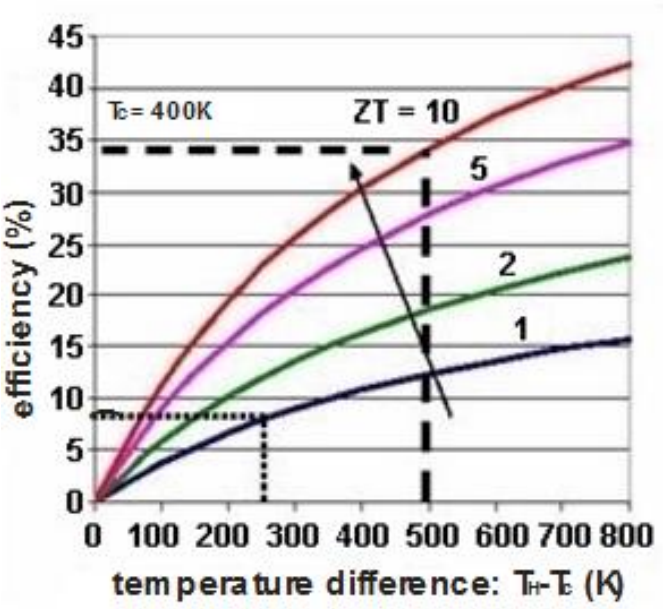

Figure 1.2 Relationship between ZT and efficiency of thermoelectric materials[20]

1.1.3 Conventional Thermoelectrics

As mentioned in the previous chapter, the thermoelectrics is a solid state device to convert thermal energy into electricity and vice versa, which is governed by Seebeck effect and Peltier effect. Seebeck effect is that when a temperature gradient is created along a semiconductor material, electrons or holes diffuse from one end to the other end. If the electrons move from the hot side to the cold side of the material, a positive electromotive force (emf) is generated in the material. Conversely, if the holes diffuse from the hot side to the cold side of the material, a negative voltage is created along the material. The open circuit electromotive force, V is developed between two ends of the materials and given by $V=-S(T_H-T_C)$, where S is the Seebeck coefficient, T_H is the hot side temperature and T_C is the cold side temperature. Figure 1.3 (a) displays the schematic illustration of a thermoelectric module for power generation.

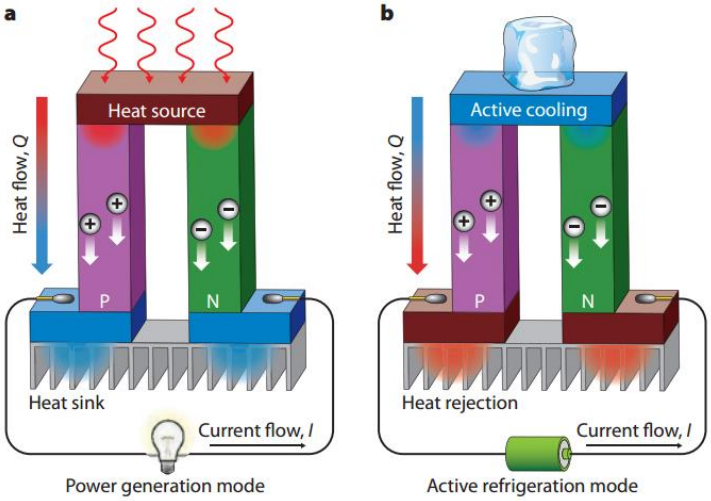

Figure 1.3 Schematic illustrations of a thermoelectric module for (a) power generation (Seebeck effect) and (b) active refrigeration (Peltier effect).[21] (copyright Royal Chemistry of Society)

Peltier effect is the opposite phenomenon of Seebeck effect and related to thermoelectric cooling. The potential difference between two dissimilar materials can produce the temperature gradient, which the schematic diagram was illustrated in Figure 1.3 (b). The Peltier heat generated between two different materials per unit time Q is equal to

$$Q = (\Pi_A - \Pi_B)I \qquad (1.3)$$

where Π_A and Π_B is the Peltier coefficient of A and B materials and I is the electrical current. The Peltier coefficients represent that how much heat (Q) flows by an electrical current (I). In other words, the Peltier coefficient is the thermal energy carried by unit charge.

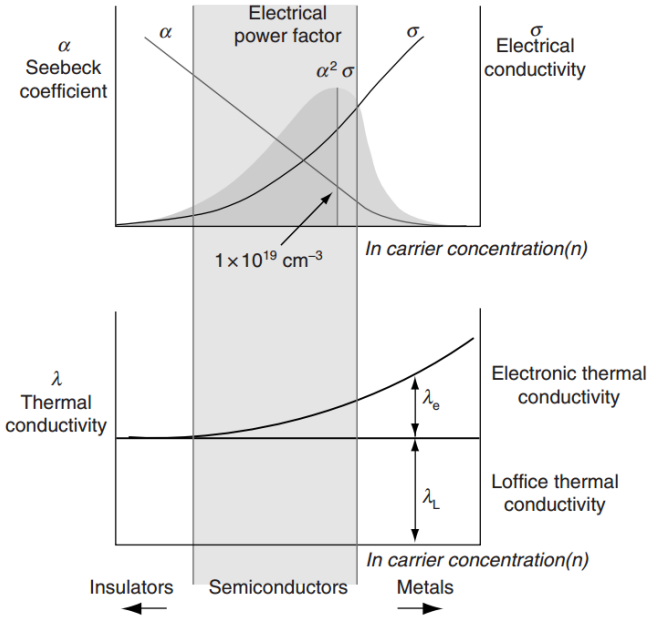

Figure 1.4 Schematic dependence of electrical conductivity, Seebeck coefficient, power factor, and thermal conductivity on concentration of free carriers.[22] (copyright Royal Chemistry of Society)

In order to increase the figure of merits defined in Equation 1, the power factor ($S^2\sigma$) should be maximized while keeping the low total thermal conductivity κ_T ($\kappa_E+\kappa_L$: κ_E =electronic thermal conductivity, κ_L=lattice thermal conductivity). However, the interdependency between the constituent parameters of ZT retards the improvement of thermoelectric performance. As shown in Figure 1.4, all of S, σ and κ_E are functions of carrier concentration. As the carrier concentration increases, S decreases but σ oppositely increases. Since κ_E is defined as an amount of heat transferred by carriers, κ_E is also dependent on the carrier concentration. Therefore, the optimum carrier concentration in semiconductor materials exists obtaining the highest thermoelectric power factor is ~10^{19}

cm^{-3}. Only independent parameter is the lattice thermal conductivity (κ_L), as shown in the bottom graph of Figure 1.4.

Hence, one of the promising approaches to enhance the thermoelectric performance is the reduction in the lattice thermal conductivity (κ_L). In addition, a large number of research have been investigated to increase the thermoelectric power factor as well. These two approaches will be briefly discussed in next sections

1.1.4 Reduction of Lattice Thermal Conductivity

The lattice thermal conductivity is defined as the conductivity of heat carried by phonons, which are quantized vibrational modes of crystalline lattice. The classical kinetic lattice thermal conductivity can be described in Equation 1.4:

$$\kappa_L = \frac{1}{3} C_l v_g l \quad (1.4)$$

where C_l is the specific heat if the Debye model is used, v_g is the group velocity of phonon and l is the mean free path, which is the average traveling length of phonons between two consecutive diffuse scattering events. The effective mean free path is determined by combining all of various phonon scattering mechanisms. Phonons are mainly scattered by lattice imperfections (defects), grain boundaries, impurities such as dopants, electrons and other phonons. [19, 23] Each scattering mechanism can be described by a relaxation rate $1/\tau$ and the relationship between the effective relaxation time (τ) and the mean free path(l) can be found from $l = v_g \tau$. The Matthiessen's rule, which shows a good approximation to combine multiple influences by the scattering sources, is shown as Equation 1.5,

$$\frac{1}{\tau_T} = \frac{1}{\tau_U} + \frac{1}{\tau_I} + \frac{1}{\tau_B} + \frac{1}{\tau_{ph-e}} \qquad (1.5)$$

where τ_T is a total relaxation time, τ_U, τ_I , τ_B, $\tau_{ph\text{-}e}$ are relaxation times affected by phonon-phonon scattering, phonon-impurity scattering, phonon-boundary scattering and phonon-electron scattering, respectively. While τ_U is strongly related to the ambient temperature, τ_I and τ_B are determined by material microstructures that can be readily engineered. For the reduction of the lattice thermal conductivity, nanostructured materials have been produced by introducing impurities and grain boundaries into a material.

As mentioned in 1.1.1.1 section and showed in Figure 1.1, many of the recent dramatic improvements of thermoelectric performance(ZT) were achieved by optimally nanostructuring thermoelectric and increasing phonon scattering, thus reducing the lattice thermal conductivity. For example, the research on hierarchical structured PbTe thermoelectric materials has been reported and demonstrated how efficient the optimal nanostructuring can cause phonon scattering leading the enhancement of the figure of merit ZT.[13] In this study, the various scale scattering sources, such as atomic scale alloy doping, nanosized precipitates and mesocale grain boundaries(Figure 1.5(a)), were introduced. Consequently, more broadband phonon scattering can be attained (Figure 1.5(b)), thus leading ZT of 2.2 at 915K.

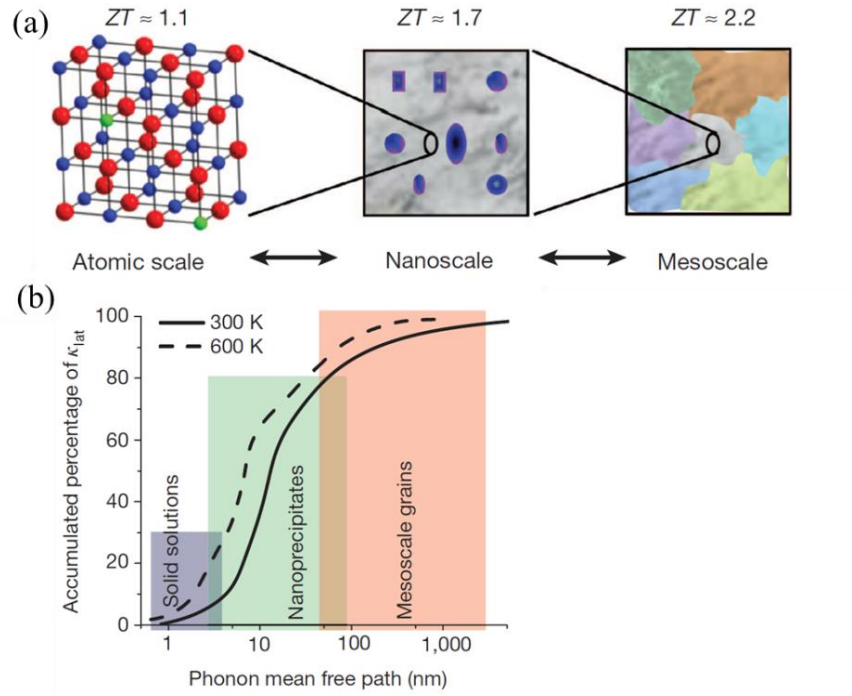

Figure 1.5 The effect of all-length-scale hierarchical structures on thermoelectric performance. (a) Maximum attainable ZT values for the particular length scales[13] (b) Contributions of phonons with different mean free paths to the cumulative κ_L value for PbTe [13, 24]. (copyright Nature Publishing Group)

1.1.5 Enhancement of Power Factor

Although the reduction of lattice thermal conductivity has been regarded as an efficient way to increase the thermoelectric performance due to the independency of κ_L, the concept of a minimal lattice thermal conductivity has been pointed out[16, 25-27] and used to estimate the theoretical maximum ZT of various materials[28]. From the prior studies, the minimal thermal conductivity of most semiconductor materials was calculated to be ~0.25 $Wm^{-1}K^{-1}$. In other words, in order to achieve better thermoelectrics performance, not only the reduction of thermal conductivity but also the power factor enhancement is strongly required.

One promising idea is the modulation doping of semiconductor, which refers that the electrons are provided from the ionized dopants in a spate region from carriers (electrons). Modulation doping has been used for electronic or photonic devices and many applications have been demonstrated by employing 2-dimensioanl electron gas (2DEGs)[29, 30] and nanowires [31]. Introduction of modulation doping to thermoelectrics is originated with that the electrical conductivity is determined by the carrier mobility as well as the carrier concentration. The electrical conductivity is defined as well-known Equation 1.6.

$$\sigma = ne\mu \qquad (1.6)$$

where σ is the electrical conductivity, n is the carrier concentration, e is the electrical charge and μ is the carrier mobility. Hence, the mobility improvement can increase the electrical conductivity while maintaining the optimum number of carrier, in other words, without altering the carrier concentration.

Several research of the modulation doping for obtaining better thermoelectric performance in a Si-Ge materials system[32, 33] or a Pb-Te alloy system[34] have been performed. Gang Chen's group demonstrated that modulation-doped Si-Ge alloy nanocomposites showed the enhanced power factor due to the improved mobility. Figure 1.6(a) displays the schematic diagram of the modulation doping of thermoelectrics. They uniformly mixed two different compositional powders, $Si_{95}Ge_5$ for a matrix and $Si_{70}Ge_{30}P_3$ for doping a matrix and separating the ionized dopants, and the mixture was compacted by a hot pressing machine. After consolidation, the grain morphologies and composition were shown in Figure 1.6(b)-(d) which refer that the composition difference between two different powders were still maintained and mixed uniformly. The electron

transferred from the $Si_{70}Ge_{30}P_3$ designed grains to $Si_{95}Ge_5$ and the carriers were separated from their parent atoms (ionized dopants). Furthermore, the thermal conductivity was also kept low because of the reduced thermal conductivity of the nanoparticles. [33]Consequently, the maximum ZT of ~1.3 at 900°C was achieved and it is ~30-40% enhanced compared to the equivalent uniform compositional sample.

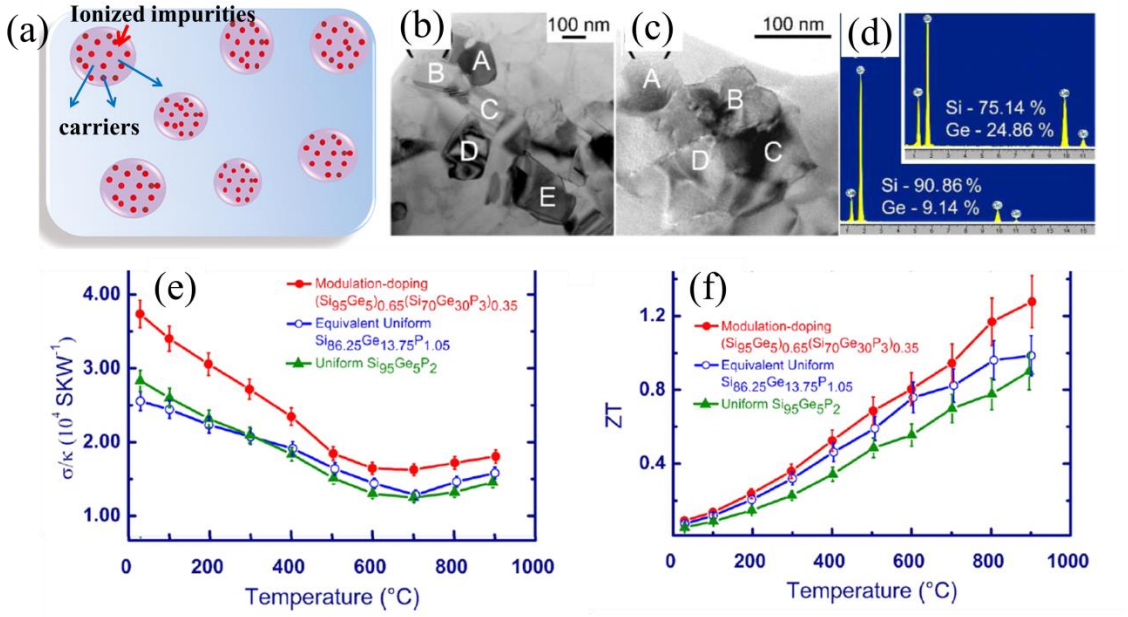

Figure 1.6 (a) Schematic diagram of modulation doping of Si-Ge alloy[32] (b)-(d) TEM images and EDAX analysis of adjacent grains of modulated doped Si-Ge (e) σ/κ plots and (f) ZT of the modulation-doping, the equivalent uniform and uniform samples. [33] (copyright American Chemical Society)

Hicks and Dresselhaus theoretically predicted that 2-D quantum wells and quantum wires could significantly increase the thermoelectric performance according to the shape of the density of states (DOS).[9, 10] As the materials size scale decreases and closes to nanometer or angstrom length scales, it is possible to induce huge alteration in DOS (see Figure 1.7). The altered DOS shapes in the low-dimensions can provide

chances to control S, σ and κ indecently. In addition, the utilization of low-dimensional materials can allow new physical phenomena, such as electron filtering[35-37], and the more efficient phonon scattering, in other words, the lower thermal conductivity, leading higher ZT. [38]

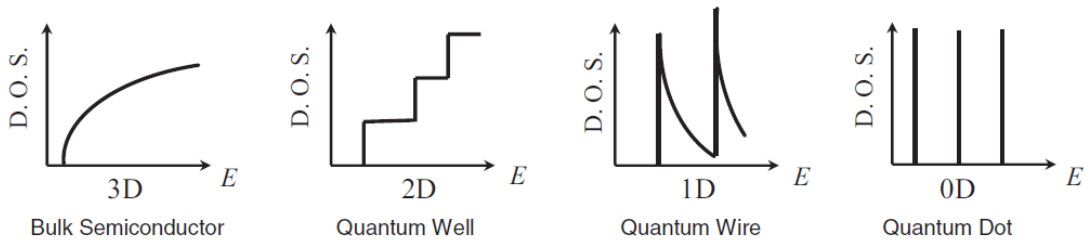

Figure 1.7 The relation between Energy and DOS for 3D (bulk material), 2D(thin films or quantum wells), 1D(nanowires) and 0D (quantum dots)[38] (copyright Wiley)

Some practical research about the band-structure engineering has been carried out and one of them is 'resonant levels'. Joseph et al. demonstrated that the introduction of thallium(Tl) impurities in lead telluride (PbTe) alloy caused the distortion of DOS, thus resulting in a 2 times higher ZT >1.5 at 776K.[39] Figure 1.8 describes a schematic DOS plot of valence band of PbTe without Tl impurities(dash line, see Figure 1.7 as well) and PbTe with Tl impurities(solid line). When the Fermi lever (E_F) can be lie within the energy range of the distortion (E_R) by energy-band engineering the figure of merit can be enhanced based on the Mahan-Sofo theory[40] and the Mott relation.

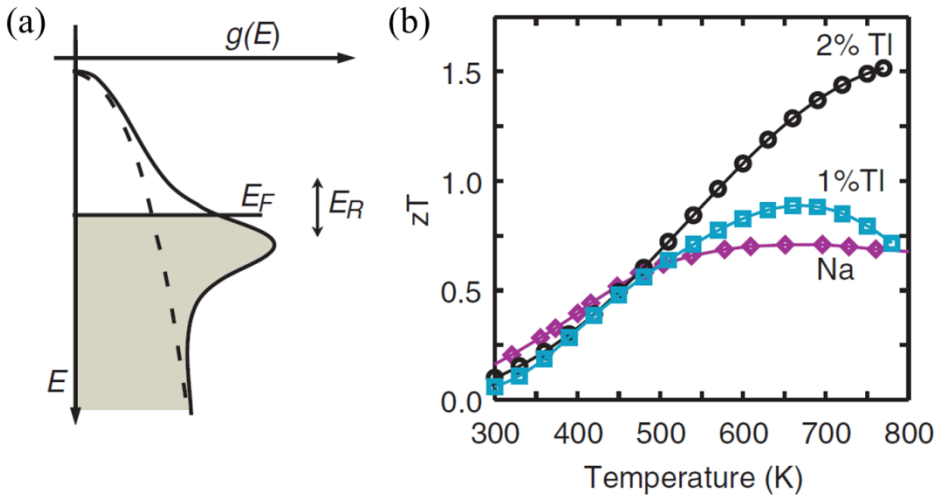

Figure 1.8 (A) Schematic plot between DOS (g(E)) vs. energy of pure PbTe (dashed line) and that of Tl-PbTe (solid line) (B) The ZT values from 300K to 800K for different composition samples (2% Tl+PbTe, 1% Tl+PbTe and Na-PbTe). (copyright AAAS)

1.2 Overview of Concentrating Solar Power

1.2.1 Introduction of Concentrating Solar Power

Concentrating solar power (CSP) systems utilize reflectors or lenses to focus a large area of sunlight, especially, solar thermal energy, onto a small area - a receiver. The mirrors focus solar thermal energy into a receiver with both a high absorptivity and a low heat loss in the operating temperature. In the meantime, a heat transfer fluid (HTF) flowing through the receiver metal tube absorbs the thermal energy and by using thermal energy transferred by HTF, high temperature compressed steam is generated to drive a turbine engine. The various liquid and vapor fluids, such as H_2O, air, oil and molten salts have been used as HTFs. There are the different types of CSP, such as power tower, parabolic trough (linear Fresnel system) and dish stirling system.

Large scale commercial facilities of CSP have been built in California, USA and Spain and now became successful models for many CSP promoting countries. Especially, the Ivanpah Solar Electric Generating System (SEGS) located in the middle of the Mojave Desert (California) employs 173,500 heliostats for concentrating sunlight in the solar power tower system. Since CSP technologies have been used to generate electricity for over 100 years, they have been demonstrated to be technically and economically practical in large scale facility and generating electricity. A large number of CSP plants are currently operating and under construction all over the World. [41-43]

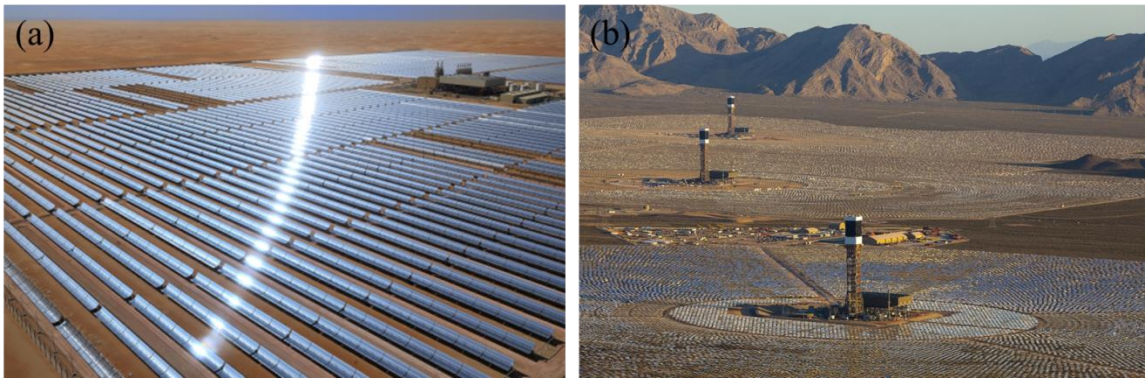

Figure 1.9 (a) The 100-megawatt Shams 1 concentrated solar power plant in the Western Region of Abu Dhabi and (b) the Ivanpah Solar Generating System (SEGS) with a grow capacity of 392-megawatt. (Image sources: http://www.beforeitsnews.com, http://breakingenergy.com)

The CSP systems contribute to avoid consuming fossil fuels and, for example, the Ivanpah SEGS has been providing reliable and clean electricity to more than 140,000 homes. Since the Ivanpah SEGS is generating solar electricity, millions of tons of carbon dioxide (400,000 tons per year) and other air pollutants can be avoided and it is equivalent of taking 70,000 cars off the road. Another economically advantage of a large CSP system is a job creation. This project created more than 2,100 jobs of workers and support staff for constructions and 86 jobs of workers for operation and maintenance. [44, 45]

1.2.2 Types of Concentrating Solar Power

CSP system can be categorized into mainly 3 different schemes consisting of different reflectors, receivers and operating temperatures. In order to maximize the efficiency and performance of CSP systems, the system designs and component selections should be optimized according to the different types.

(1) Parabolic Trough/ Linear Concentrator System

A parabolic trough is a type of solar thermal collector that is linear and curved. The solar energy reflects the mirror to its plane of symmetry and concentrates along the focal line in where the solar receivers are located. HTFs (water/steam or others) flows though the solar receiver tube to absorb thermal energy from the focused solar radiation and transfers to thermal storage tanks (or heat exchanger) or directly is used to drive turbine engines (Figure 1.10(a)) [46] Linear Fresnel reflector is similar to parabolic tough collector, but the reflecting mirrors are not curved but flat. These flat mirrors can be controlled by two-axis tracking systems to follow the Sun's movement thus increase the efficiency. Since the reflectors are flat and elastic, the linear Fresnel system is much cheaper than parabolic trough scheme. [47, 48]

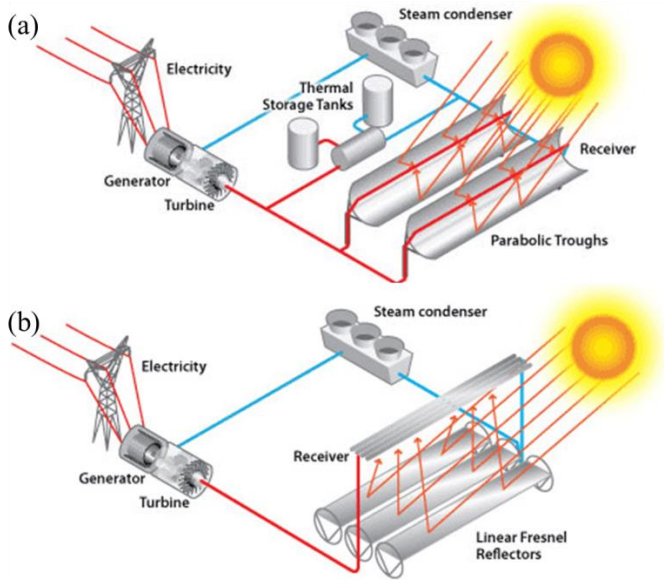

Figure 1.10 Schematic diagrams of (a) parabolic trough system and (b) linear Fresnel reflector systems.[46] (Image source: http://www.energy.gov)

The parabolic trough system is the most common and mature scheme of CSP systems. This system has commercially proven with over 500-megawatt installed

capacity. In U.S.A., parabolic trough solar power plants have been working for 20years. However, the maximum operating temperature is ~ 400^{o}C and the efficiency is limited. (see Table 1)

Table 1.1 Comparison between various types of CSP [47, 49, 50]

Collector Type	Rel. thermodynamic efficiency	Operating temp. range (^{o}C)	Relative cost	Concentration ratio (sun)
Parabolic Trough	Low	50–400	Low	15–45
Linear Fresnel	Low	50–300	Low	10–40
Power Tower	High	300–565	High	150–1500
Dish-Stirling	High	120–1500	High	100–1000

(2) Power tower system

The power tower CSP system is consisting of a large number of flat and sun-tracking mirrors (heliostats) concentrating sunlight onto a solar receiver at the top of a center tower (see Figure 1.10) and a tower receiver at the center of them. HTFs flowing through the receiver (metal tubes) are heated by the concentrated sunlight and transfer solar thermal energy to produce the steam or directly drive the conventional turbine engines. Many power towers use water/steam as the HTF but other recent systems are testing the functional HTFs, especially, a molten nitrate salt, since its excellent heat-transfer and energy storage abilities are very useful to improve the system efficiency. Two large-scale power tower CSP plants (Solar One and Solar Two) were installed in U.S.A. and have been operated. The Solar One proved the capability to produce a large amount of clean and reliable electricity (38 million kW-hr from 1982 to 1988). In order to provide a dispatchability of renewable energy, the thermal energy storage (TES) systems have been actively pursued. The Solar Two plant was had designed to employ

and test molten salt for HTF and TES, and successfully demonstrated to store thermal energy and shift the clean electricity generation to night time and cloudy days. [51] The dispatchability is the biggest advantage of CPS system, because other solar renewable energy technology such as photovoltaic is not capable of storing the solar energy or electricity without the extremely expensive battery system.

Figure 1.11 Schematic diagram and picture of the power tower system. (Image sources : http://www.brightsourceenergy.com/)

(3) Dish stirling system

The dish-shaped solar concentrator collects the sunlight and concentrates solar energy to a thermal energy receiver. (see Figure 1.12) The dish is controlled by a tracking system to continuously gather maximum solar energy. Therefore, the major components of the system are the dish-shaped concentrator and the stirling engine to generate power. The dish stirling system offer the highest efficiency from solar energy to electricity 31%~32% among all of CSP types. However, since the electricity is directly generated

by the concentrated radiations, there is no thermal energy storage system with the dish stirling system. Without TES, the dish stirling provides power in the same way as the photovoltaic, which is much cheaper.

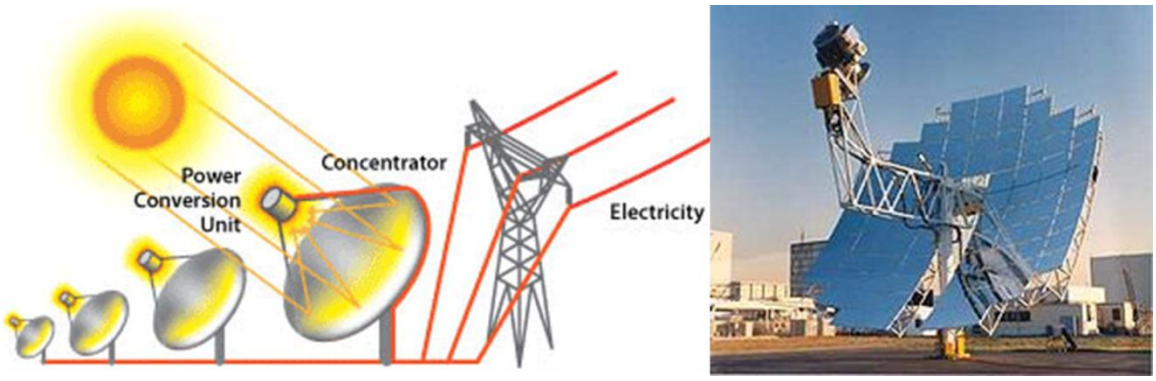

Figure 1.12 Schematic diagram(left) and photograph(right) of the dish stirling system[46] (Image source : http://www.energy.gov)

1.2 Thesis objectives

Thermal energy conversion technologies can play an important role to produce clean and reliable renewable energy. In this thesis, two main technologies, thermoelectrics and concentrating solar power (CSP), are discussed. In order to compete with other conventional energy generation systems, the efficiency of those technologies certainly needs to be enhanced. To achieve this goal, the following issues were addressed.

For thermoelectrics, the strategy for improving the power factor was demonstrated using energy-band engineering of Ge-Si core/shell nanowires with a gate voltage modulation scheme. The intrinsic Ge-Si core/shell nanowires showed high carrier mobility by minimizing ionized impurity scattering, thus induced the power factor enhancement. For CSPs, the surface modification and the material designs were carried out, in order to develop highly durable and efficient light absorbing coatings for CSP receivers. Multi-scaled surface showed the suppressed reflection and dramatically improved light absorption in visible and NIR range, in comparison to smooth surface of mono-dispersed particles coating layer. In addition, the black oxide nanopowders were synthesized and used to fabricate the high performance and high temperature durable coating layer. The scalable method was established using spray process and sacrificial polymer materials. Excellent durability at high temperature was confirmed by annealing at the desired temperature for 1000 hours.

1.3 Overview of the dissertation

Chapter 1 provides a brief introduction to principles of two thermal energy conversion technologies, thermoelectrics and concentrating solar powers.

Chapter 2 describes the experimental study demonstrating that the gate-modulated Ge-Si core/shell nanowires enhanced the carrier mobility due to suppressed ionized impurity scattering and led to improve the power factor.

Chapter 3 demonstrates the effect of multi-scaled structure of spectrally selective coating of CSP receivers.

Chapter 4 discusses the black oxide light absorbing coating for high temperature CPS receivers was successfully developed. The thermal efficiency was improved using a scalable and simple method. High temperature stability was proved by annealing at desired temperature for 1000 hours.

Chapter 5 summarized the dissertation and describes potential future directions.

1.4 References

1. Hoffert, M. I.; Caldeira, K.; Benford, G.; Criswell, D. R.; Green, C.; Herzog, H.; Jain, A. K.; Kheshgi, H. S.; Lackner, K. S.; Lewis, J. S.; Lightfoot, H. D.; Manheimer, W.; Mankins, J. C.; Mauel, M. E.; Perkins, L. J.; Schlesinger, M. E.; Volk, T.; Wigley, T. M. L. *Science* **2002,** 298, (5595), 981-987.

2. Hisatomi, T.; Kubota, J.; Domen, K. *Chemical Society Reviews* **2014**.

3. Lawrence Livermore National Laboratory, Estimated U.S. Energy Use in 2013.

4. Snyder, G. J.; Toberer, E. S. *Nat Mater* **2008,** 7, (2), 105-114.

5. Amatya, R.; Ram, R. J. *J Electron Mater* **2010,** 39, (9), 1735-1740.

6. Kraemer, D.; Poudel, B.; Feng, H. P.; Caylor, J. C.; Yu, B.; Yan, X.; Ma, Y.; Wang, X. W.; Wang, D. Z.; Muto, A.; McEnaney, K.; Chiesa, M.; Ren, Z. F.; Chen, G. *Nat Mater* **2011,** 10, (7), 532-538.

7. Xi, H. X.; Luo, L. G.; Fraisse, G. *Renew Sust Energ Rev* **2007,** 11, (5), 923-936.

8. Vineis, C. J.; Shakouri, A.; Majumdar, A.; Kanatzidis, M. G. *Adv Mater* **2010,** 22, (36), 3970-3980.

9. Hicks, L. D.; Dresselhaus, M. S. *Phys Rev B* **1993,** 47, (19), 12727-12731.

10. Hicks, L. D.; Dresselhaus, M. S. *Phys Rev B* **1993,** 47, (24), 16631-16634.

11. Poudel, B.; Hao, Q.; Ma, Y.; Lan, Y. C.; Minnich, A.; Yu, B.; Yan, X. A.; Wang, D. Z.; Muto, A.; Vashaee, D.; Chen, X. Y.; Liu, J. M.; Dresselhaus, M. S.; Chen, G.; Ren, Z. F. *Science* **2008,** 320, (5876), 634-638.

12. Hsu, K. F.; Loo, S.; Guo, F.; Chen, W.; Dyck, J. S.; Uher, C.; Hogan, T.; Polychroniadis, E. K.; Kanatzidis, M. G. *Science* **2004,** 303, (5659), 818-821.

13. Biswas, K.; He, J. Q.; Blum, I. D.; Wu, C. I.; Hogan, T. P.; Seidman, D. N.; Dravid, V. P.; Kanatzidis, M. G. *Nature* **2012,** 489, (7416), 414-418.

14. Joshi, G.; Lee, H.; Lan, Y. C.; Wang, X. W.; Zhu, G. H.; Wang, D. Z.; Gould, R. W.; Cuff, D. C.; Tang, M. Y.; Dresselhaus, M. S.; Chen, G.; Ren, Z. F. *Nano Lett* **2008,** 8, (12), 4670-4674.

15. Hochbaum, A. I.; Chen, R. K.; Delgado, R. D.; Liang, W. J.; Garnett, E. C.; Najarian, M.; Majumdar, A.; Yang, P. D. *Nature* **2008,** 451, (7175), 163-U5.

16. *CRC Handbook of Thermoelectrics*. CRC Press: Boca Raton, **1995**.

17. Matsubara, K. *Xxi International Conference on Thermoelectrics, Proceedings Ict '02* **2002**, 418-423.

18. Goldsmid, H. J., *Electronic refrigeration*. Pion: **1986**.

19. Chen, G., *Nanoscale Energy Transport and Conversion : A Parallel Treatment of Electrons, Molecules, Phonons, and Photons*. Oxford University Press: 2005.

20. Rowe, D. M.; Bhandar, C. M., *Modern Thermoelectrics*. Reston Publishing Company: **1983**.

21. Li, J. F.; Liu, W. S.; Zhao, L. D.; Zhou, M. *Npg Asia Mater* **2010,** 2, (4), 152-158.

22. *Thermoelectrics handbook: macro to nano*. CRC Press: Boca Raton, **2006**.

23. Tien, C.-L.; Majumdar, A.; Gerner, F. M., *Microscale Energy Transport*. Taylor&Francis: **1997**.

24. Qiu, B.; Bao, H.; Zhang, G. Q.; Wu, Y.; Ruan, X. L. *Comp Mater Sci* **2012,** 53, (1), 278-285.

25. Min, G.; Rowe, D. M. *Appl Phys Lett* **2000,** 77, (6), 860-862.

26. Cahill, D. G.; Watson, S. K.; Pohl, R. O. *Phys Rev B* **1992,** 46, (10), 6131-6140.

27. Slack, G. A. *Thermoelectric Materials - New Directions and Approaches* **1997,** 478, 47-54.

28. Slack, G. A.; Hussain, M. A. *J Appl Phys* **1991,** 70, (5), 2694-2718.

29. Schaffler, F. *Semicond Sci Tech* **1997,** 12, (12), 1515-1549.

30. Ismail, K.; Chu, J. O.; Arafa, M. *Ieee Electr Device L* **1997,** 18, (9), 435-437.

31. Dillen, D. C.; Kim, K.; Liu, E. S.; Tutuc, E. *Nat Nanotechnol* **2014,** 9, (2), 116-120.

32. Zebarjadi, M.; Joshi, G.; Zhu, G. H.; Yu, B.; Minnich, A.; Lan, Y. C.; Wang, X. W.; Dresselhaus, M.; Ren, Z. F.; Chen, G. *Nano Lett* **2011,** 11, (6), 2225-2230.

33. Yu, B.; Zebarjadi, M.; Wang, H.; Lukas, K.; Wang, H. Z.; Wang, D. Z.; Opeil, C.; Dresselhaus, M.; Chen, G.; Ren, Z. F. *Nano Lett* **2012,** 12, (4), 2077-2082.

34. Harman, T. C.; Spears, D. L.; Manfra, M. J. *J Electron Mater* **1996,** 25, (7), 1121-1127.

35. Wang, S.; Mingo, N. *Phys Rev B* **2009,** 79, (11).

36. Zide, J. M. O.; Vashaee, D.; Bian, Z. X.; Zeng, G.; Bowers, J. E.; Shakouri, A.; Gossard, A. C. *Phys Rev B* **2006,** 74, (20).

37. Ko, D. K.; Kang, Y. J.; Murray, C. B. *Nano Lett* **2011,** 11, (7), 2841-2844.

38. Dresselhaus, M. S.; Chen, G.; Tang, M. Y.; Yang, R. G.; Lee, H.; Wang, D. Z.; Ren, Z. F.; Fleurial, J. P.; Gogna, P. *Adv Mater* **2007,** 19, (8), 1043-1053.

39. Heremans, J. P.; Jovovic, V.; Toberer, E. S.; Saramat, A.; Kurosaki, K.; Charoenphakdee, A.; Yamanaka, S.; Snyder, G. J. *Science* **2008,** 321, (5888), 554-557.

40. Mahan, G. D.; Sofo, J. O. *P Natl Acad Sci USA* **1996,** 93, (15), 7436-7439.

41. Pitz-Paal, R.; Dersch, J.; Milow, B. *European Concentratiung Solar Thermal Road-Mapping*; ECOSTAR: **2003**.

42. Marsh, G. *Renewable Energy Focus* **2009,** 10, (3), 50-52,54,56-58.

43. Richter, C.; Teske, S.; Short, R. *Concentrating Solar Power Global Outlook 2009*; **2009**.

44. Danko, P., How The Ivanpah Solar Plant 'Powers 140,000 Homes'. *Renewable Energy, Solar Power* **2014**.

45. power-technology.com Ivanpah Solar Electric Generating System, United States of America. http://www.power-technology.com/projects/ivanpahsolarelectric/

46. DOE Sunshot Initiative, CSP SYSTEMS RESEARCH AND DEVELOPMENT. http://energy.gov/eere/sunshot/csp-systems-research-and-development

47. Barlev, D.; Vidu, R.; Stroeve, P. *Sol Energ Mat Sol C* **2011,** 95, (10), 2703-2725.

48. Mills, D. R.; Morrison, G. L. *Sol Energy* **2000,** 68, (3), 263-283.

49. International Energy Agency, *Technology Roadmap : Concentrating Solar Power*; International Energy Agency: **2010**.

50. Sargent & Lundy LLC Consulting Group, *Assessment of Parabolic Trough and Power Tower Solar Technology Cost and Performance Forecasts* NREL/SR-550-34440 National Renewable Energy Laboratory **2003**.

51. Wikipedia, The Solar Project. http://en.wikipedia.org/wiki/The_Solar_Project

CHAPTER 2 : Gate-Modulated Thermoelectric Power Factor of Hole Gas in Ge–Si Core–Shell Nanowires

2.1 Introduction

Thermoelectric power generation has attracted significant interest recently due to its promise in waste heat recovery and power generation [1]. There is a resurging effort to improve the energy conversion efficiency of thermoelectric devices, which is determined by the figure of merit ZT, defined as $S^2\sigma T/\kappa$, where S, σ, κ and T are thermopower (or Seebeck coefficient), electrical conductivity, thermal conductivity and the absolute temperature, respectively [2]. The most common approach to improve the ZT is to suppress the lattice component of the thermal conductivity (κ_L) by using complex[3] and/or nano-structures [4, 5] for enhanced phonon scattering. The numerator of the ZT formula, namely the power factor ($S^2\sigma$) has been more challenging to engineer, because S and σ are highly interdependent. As the carrier concentration is increased for higher σ, most commonly by chemical doping, S generally decreases[2]. Moreover, chemical doping inevitably suppresses carrier mobility (μ) due to the increased ionized impurity scattering in the degenerate doping regime[6]. Even though it has been theoretically predicted that the power factor could be enhanced in low dimensional systems such as quantum wells[7] and quantum wires[8], experimental observation of such enhancement has been very challenging. One of the associated difficulties lies in the surface charge states in small dimension nanostructures, which tend to suppress μ and σ via surface scattering[9].

A promising candidate for investigating the nanoscale thermoelectric phenomena and mitigating the surface charge scattering is core-shell heterostructure nanowires (NWs)[10]. Core-shell NWs have attracted tremendous interest recently due to their remarkable electronic, optical and thermal properties, as well as potential applications as building blocks for nano-devices[11-14]. Recently, core-shell NWs have also been suggested as a promising candidate for thermoelectric application primarily because of the suppressed L due to phonon scattering and possible phononic engineering at the core-shell interfaces[15-23]. It has been shown that intrinsic core-shell NWs exhibit high carrier mobility, even with small diameter [12], because of the suppression of ionized impurity scattering and surface charges. The high mobility could provide a unique opportunity to achieve a high power factor in NWs, however, to the best of our knowledge, power factor of individual core-shell NWs have not been experimentally studied.

To systematically investigate the power factor of NWs, it is necessary to study its dependence on carrier concentration. Field effect modulation provides a convenient means to facilitate such measurements, as has been shown previously on PbSe NWs [24], and very recently on InAs NWs [25]. Here, we report the first such measurements on gate modulated electrical conductivity and thermopower of individual core-shell heterostructure NWs as well as the relationship between thermoelectric power factor and carrier concentration. Unlike nanostructures measured previously, core-shell NWs provide a unique system in which the core contains high concentration of free holes due to surface Fermi level pinning even without chemical doping[12, 26]. In addition, the surface charge scattering can also be significantly mitigated by the passivation of the epitaxial shell. Therefore, it is expected that core-shell NWs could serve as an excellent platform

for investigating the thermoelectric-carrier concentration relationship of nanoscale interfacial carriers without the complication of ionized impurities, surface charge scatterings, as well as dopant segregation and non-uniformity, which are usually encountered in highly doped NWs [9, 24].

2.2 Experiments

2.2.1 Preparation of Ge/Si Core/Shell Nanowires

In this study, we used Ge-core Si-shell NWs as a material system to perform the gate modulation experiments. Single crystalline Ge-Si core-shell NWs studied here were synthesized by a chemical vapor deposition (CVD) method within the framework of vapor liquid solid (VLS) growth, as described in detail in earlier works [12, 26]. Briefly, colloidal Au nanoparticles of ~2-5 nm in diameter were deposited onto Si substrates as the growth catalysts and placed in a tube furnace (ET2000, CVD Corp.). Intrinsic Ge NWs were grown first by flowing 10% GeH_4 in H2 (30 standard cm^3 per min (sccm)) at 300 torr and 280 ^oC for ~15 min. Subsequently, the intrinsic Si shell was deposited within the same reactor immediately after the Ge core growth at 450 ^oC for 5 minutes by using SiH_4 (5 sccm) at 5 torr. Figure 2.1 (a) shows the schematic illustration of the core-shell structure, while Figure 2.1 (b) shows a representative high-resolution TEM (HRTEM) image of the Ge-Si core-shell NWs. As shown in the figures and based on our extensive TEM observations, the Ge cores have diameters of 10-30 nm while the Si shells including the amorphous native SiO_2 are typically 2±0.5 nm thick. In addition, the Si-Ge interface is epitaxial with no dislocations[12] and the cross section of the wires is circular [26].

2.2.2 Fabrication of Seebeck Measurement Device

Figure 2.1 (c) shows a scanning electron microscopy (SEM) graph of the device for the gated electrical conductivity and thermopower measurements. Electrode 1 is used as the heating element to create a temperature gradient along the NWs for the thermopower measurements. Electrodes 2 and 3 are used for 2-point I-V characterization as well as the voltage and temperature measurements. Doped Si substrates were used as the global gate electrode (bottom inset in Figure 2.1 (c)). To fabricate the devices, Ge-Si core-shell NWs were solution casted onto a Si substrate covered with a thermal SiO_2 insulation layer (30 or 300 nm thick). NW devices in the back-gated configuration were fabricated using standard lithography techniques. 5/55/30 nm Ti/Ni/Au was patterned onto a NW by e-beam lithography, liftoff and thermal evaporation (top inset in Figure 2.1 (c)). A brief (~1-5 seconds) buffered hydrofluoride (BHF) dip was performed immediately prior to the metal evaporation to remove the native oxides on the NWs. The devices were then annealed at 350 ^{o}C in a reforming gas (5% H_2 in N_2) for 30 seconds to improve the electrical contacts between the metal electrodes and the NWs.

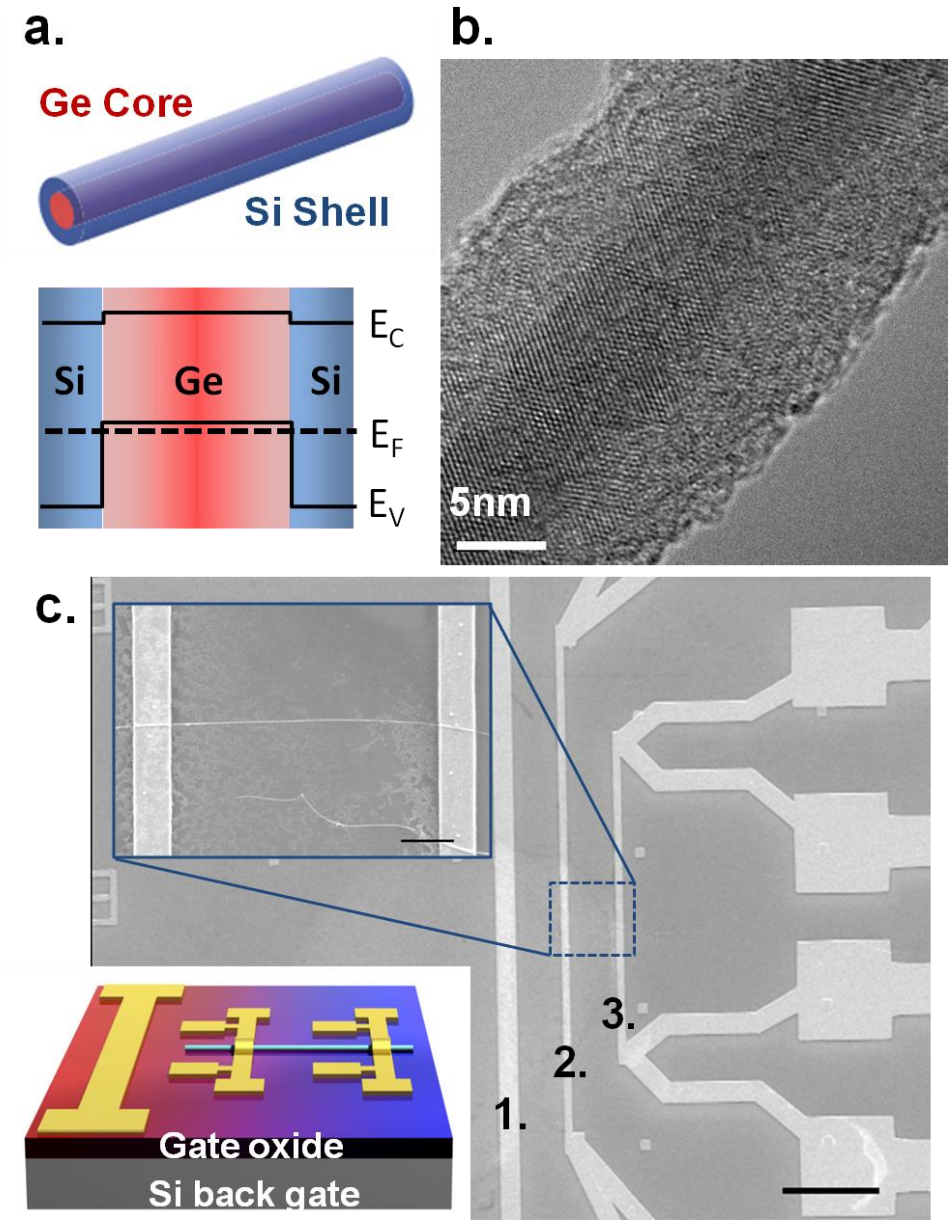

Figure 2.1 (a) Schematic of the band diagram in Ge-Si core-shell NWs and (b) high-resolution TEM (HRTEM) image of the Ge-Si core-shell NWs. (c) SEM image of the device used for the gated electrical conductivity and thermopower measurements. (copyright American Chemistry Society)

2.2.3 Analysis and Modeling of Seebeck Measurement Device

The temperature rise in the two resistive thermometer probes (electrodes 2 and 3 in Figure 2.1 (c)) was modeled using finite element analysis based on COMSOL® , and was compared with the experimentally measured values. Since the heater line is long compared to its width and thickness, a two-dimensional model can be used. The model consists of a Si substrate (thickness = 500 m), a thermal SiO_2 insulation layer (thickness is either 300 nm or 30 nm), and three metal electrodes (one heater and two thermometer probes, namely, probe 1, 2, and 3 in Figure 2.1 (c)).

Thermal conductivity of the Si substrate was measured to be 128 $Wm^{-1}K^{-1}$ as shown in the next section. Thermal conductivity of the thermal oxide layer is taken to be 1.3 W/m-K.[27] Thermal conductivity of the metal electrodes (5/55/30 nm, Ti/Ni/Au) are calculated from its measured electrical conductivity of 7.7×10^{6} $S.m^{-1}$ and the Wiedemann Franz law ($\kappa_e=L\sigma T$), where the Lorenz number L = 2.45×10^{-8} W K^{-2}. The calculated thermal conductivity is found to be 56.5 $Wm^{-1}K^{-1}$, lower than that of bulk Ni (91 $Wm^{-1}K^{-1}$) and Au (318 $Wm^{-1}K^{-1}$), as expected. As discussed below, the electrodes have a profound impact on the temperature field for the nanowire Seebeck measurement.

As shown in Figure 2.2 (b), the temperature decreases from the center of the heater (probe 1), first very rapidly and then gradually when the distance is greater than 2μm away from the heater. However, the temperature is relatively uniform beneath electrodes 2 & 3 (centered at x = 6 and 12 μm respectively, see the inset of Figure 2.2 (b)). This is because the metal electrodes have a much higher thermal conductivity compared with the underlying SiO_2 layer, thereby effectively spreading the heat. This is very desirable for the thermopower measurements conducted here: the temperature

measured by the electrodes, which represents the average temperature under the electrodes, is very close to the temperature at the inner edges of the electrodes. Since the measured Seebeck voltage (V_S) only accounts for the voltage drop across the inner edges of the electrodes due to the much higher electrical conductance of the metal compared to the NWs, the measured temperature difference represents the appropriate one corresponding to the measured voltage.

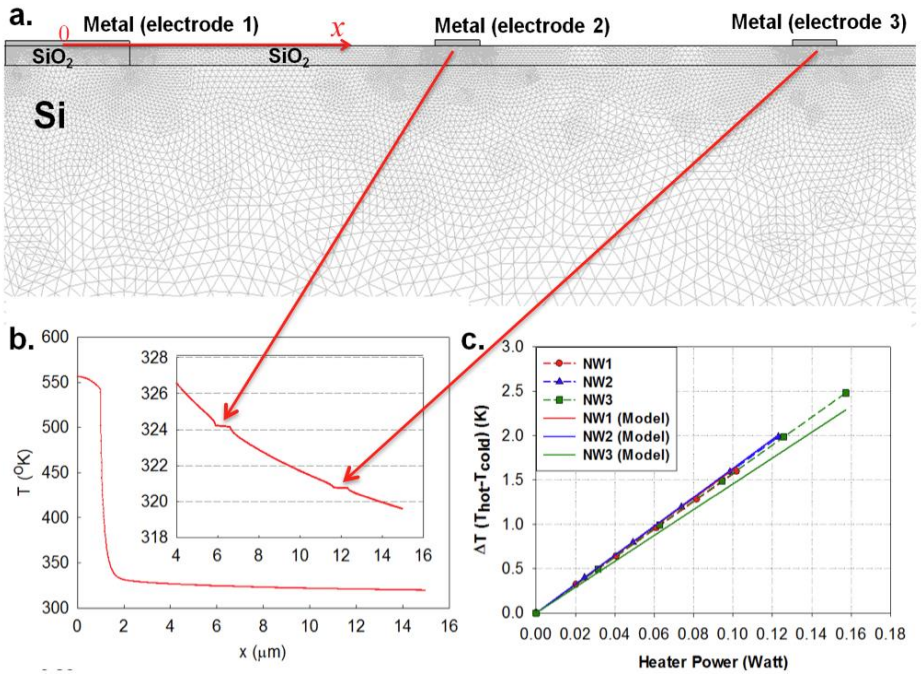

Figure 2.2 (a) Schematic of the finite element model of the temperature profile. (b) Modeled temperature profile along the *x* direction. (c) Modeled and measured temperature difference vs. heating power for the three NW samples. (copyright American Chemistry Society)

Figure 2.2 (c) shows the measured and modeled temperature difference as a function of applied power on the heater line (electrode 1 in Figure 2.1 (c)). It shows good agreement between the measured and modeled values for all three samples, validating our thermometry technique. We also found that the calculated temperature difference is

insensitive to the thermal oxide thickness within the range of 30 to 300 nm. This is because the temperature difference is governed by the thermal conductivity of the substrate (Si), even though the absolute temperature of the electrodes does depend on the oxide thickness.

For a simulation, we measured the thermal conductivity of the Si substrate using the 3ω method[28, 29]. Figure 2.3 shows the temperature rise (ΔT) as a function of the frequency of the heating current, where ΔT was calculated using:

$$\Delta T = 2\frac{dT}{dR}\frac{R}{V}V_{3w} \qquad (2.1)$$

where $R, V, V_{3\omega}$ are the resistance, 1ω voltage, and 3ω voltage of the heater, respectively, and dR/dT is the TCR of the heater.

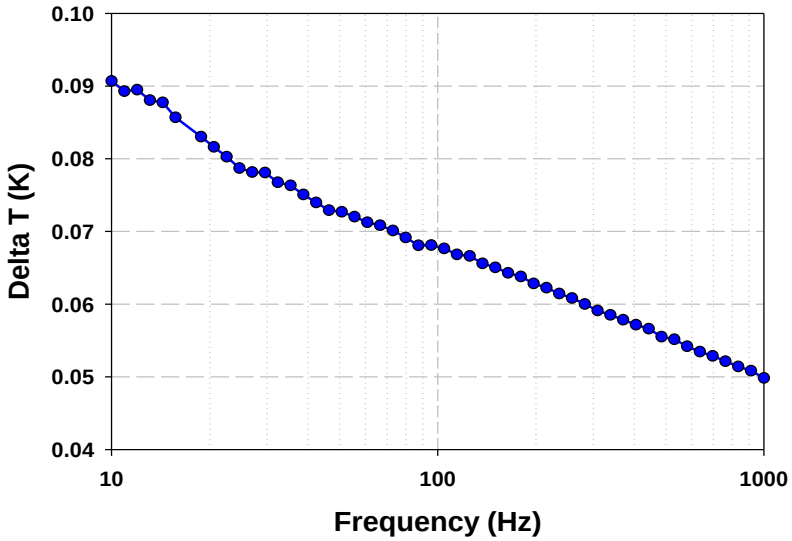

Figure 2.3 ΔT measured in the 3ω method at T=300K on a Si substrate used in a thermopower measurement device. (copyright American Chemistry Society)

Thermal conductivity of the Si substrate can be written as [28],

$$\kappa = \frac{V^3}{4\pi LR^2\left(\frac{dV_{3\omega}}{dln(f)}\right)}\frac{dR}{dT} \qquad (2.2)$$

where L is the length of the heater, and f is the frequency of the electrical current.

2.2.4 Thermopower Measurement and Nanowire Characterization

For thermopower measurements, in Figure 2.1 (c), electrode 1 is used as the heating element to create a temperature difference ΔT and a Seebeck voltage V_S at two ends of a NW, both are measured by the electrodes 2 and 3 to obtain the Seebeck coefficient:

$$S = -\frac{dV_s}{d\Delta T} \qquad (2.3)$$

The temperature difference from electrode 2 to 3 was obtained by measuring the change in four-point resistance of the electrodes. The temperature coefficient of resistance (TCR) for each resistive thermometer probe was calibrated during the measurements. Figure 2.4 shows the measured temperature dependence of resistance of electrodes 2 and 3.

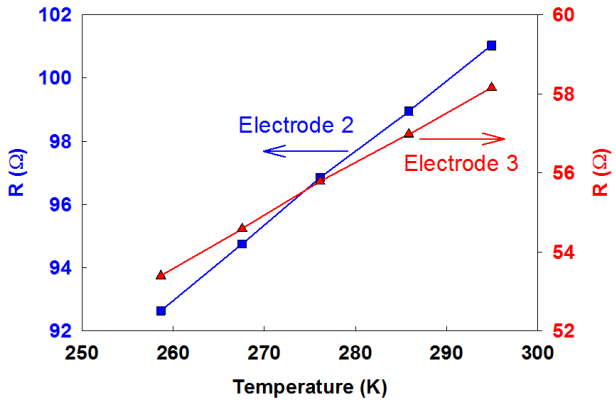

Figure 2.4 Measured temperature dependence of resistance of electrodes 2 and 3 in Figure3.1c, in order to obtain the TCR of each resistive thermometer probes. (copyright American Chemistry Society)

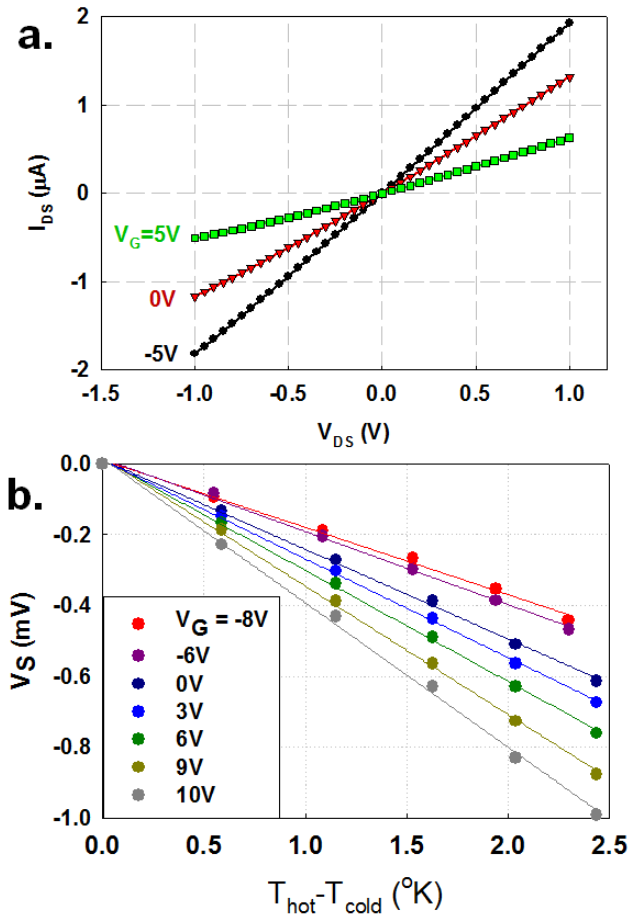

Figure 2.5 Gate modulated electrical and thermopower measurements of the NWs (a) I_{DS} vs. V_{DS} under different V_G (b) V_S vs. ΔT between electrodes 2 & 3 under various V_G. (copyright American Chemistry Society)

In the experiments, the heater power is gradually increased to approximately 0.2 Watt such that the temperature difference increases from 0 to ~2°K, as shown in Figure2. 5 (b). It is worth noting that the high thermal conductivity of metal electrodes 2 & 3 ensures a uniform temperature distribution beneath them, as demonstrated by finite element thermal modeling. Therefore, the temperature measured by each of the electrodes represents the appropriate temperature used in Equation 2.1 to extract the Seebeck coefficient. Figure 2.5 (b) shows the measured V_s vs. ΔT under various gate voltages. It

shows that the slope of V_s vs. ΔT, hence S, increases as the gate voltage increases, which is a result of p-type behavior.

Table 2.1 lists the NW samples measured in this study. The actual diameters of each NW were measured with an atomic force microscope (AFM) in tapping mode and AFM images and height profiles are shown in Figure 2.6. The Ge core diameters were estimated by subtracting twice the thickness of the Si shell (the shell is ~ 2 nm thick) from the overall diameters. The channel length, namely the distance between the two electrodes, is approximately 5 μm to ensure diffusive transport of carriers (top inset in Figure 2.1 (c)). The gate oxide thickness is 30 nm for NW1 and 300 nm for NW2 & NW3.

Table 2.1 A list of Ge-Si core-shell NW samples measured in this study

Sample ID	Overall Dia. (nm)	Ge core Dia. (nm)	Length (μm)	Gate Oxide Thickness (nm)	V_{th} (V)
NW1	28.0	24.0	5.70	30	5.8
NW2	19.1	15.1	5.01	300	10.0
NW3	15.4	11.4	4.82	300	7.0

As shown in Figure 2.5 (a), the I-V curves of the NWs under various gate voltages are linear, suggesting Ohmic contact between the semiconductor NWs and the metal electrodes due to the highly conductive nature of the NWs. It also shows that the conductance of the NWs decreases as the gate voltage increases, indicating p-type behavior as expected for similar Ge-Si core-shell NWs [12].

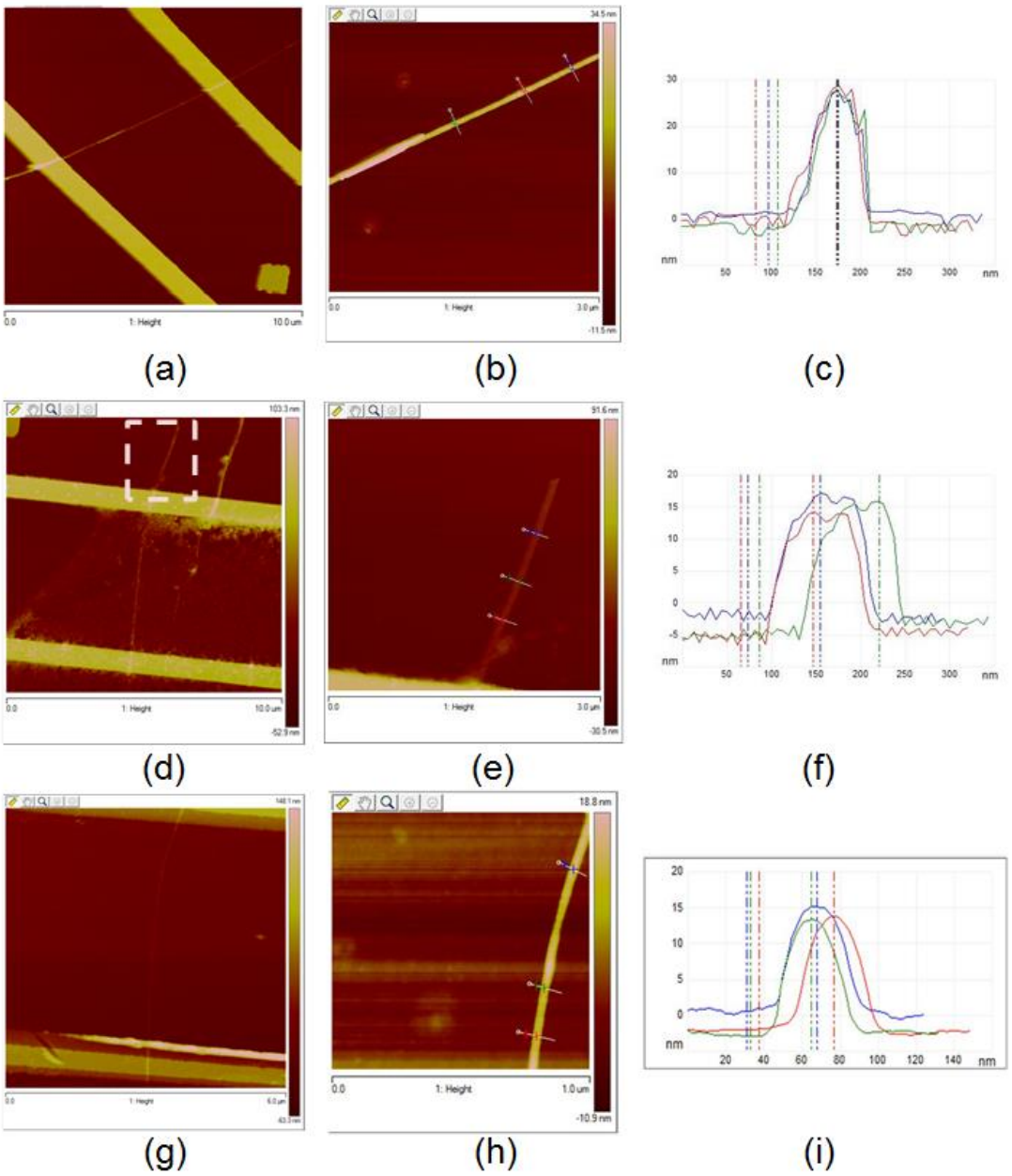

Figure 2.6 AFM images of the three measured NWs: (a)-(c) NW1; (d-f) NW2; (g-i) NW 3. (copyright American Chemistry Society)

2.3 Results and Discussion

2.3 Results and Discussion

2.3.1 Gate modulated electrical transport behavior of Ge/Si core/shell nanowires

We first discuss gate modulated electrical transport in the core-shell NWs. Figure 2.7 (a) shows the source-drain current (I_{DS}) as a function of gate voltage (V_G) for the NW samples. The data was collected with source-drain voltage V_{DS} = 1V. As expected, all the NWs show increased I_{DS} as V_G decreases, as a result of the p-type behavior and hole transport. The threshold voltages (V_{th}) for NW1, NW2 and NW3 are 5.8, 10 and 7 V, respectively (Table 2.1). At V_G=0, there is still a large current, indicating that free holes are accumulated in the dopant-free Ge cores. The large hole concentration is induced by the surface Fermi level pinning, as observed previously in similar Ge-Si core-shell NWs[12, 26]. As shown in the energy diagram of the core-shell heterostructures (Figure 2.1 (a)), due to the offset between the valence band edges(E_V) of Si and Ge (~0.5 eV), the Fermi level (E_F) lies somewhere close to the E_V of Ge, inducing a high concentration 'hole gas' inside the Ge core [12]. This resembles the two-dimensional electron gas (2DEG) in quantum well heterostructures [30]. As V_G shifts to higher voltages ($+10^{-15}$ V), E_F moves into the bandgap of Ge, thereby turning off the NWs (Figure 2.7 (a)) when $V_G > V_{th}$. On the other hand, as gate voltage decreases to negative values, E_F continues shifting down, injecting more carriers into the Ge core and leading to a higher current (Figure 2.7 (a)). Figure 2.7 (b) shows the electrical conductivity of the NWs, calculated from where A is the cross-sectional area of the Ge core and L is the NW length (see Table 2.1). The observed σ's are in the range of 10^4-10^5 $S.m^{-1}$ depending on the NW diameter and gate voltage, which is very high for NWs with such small diameters.

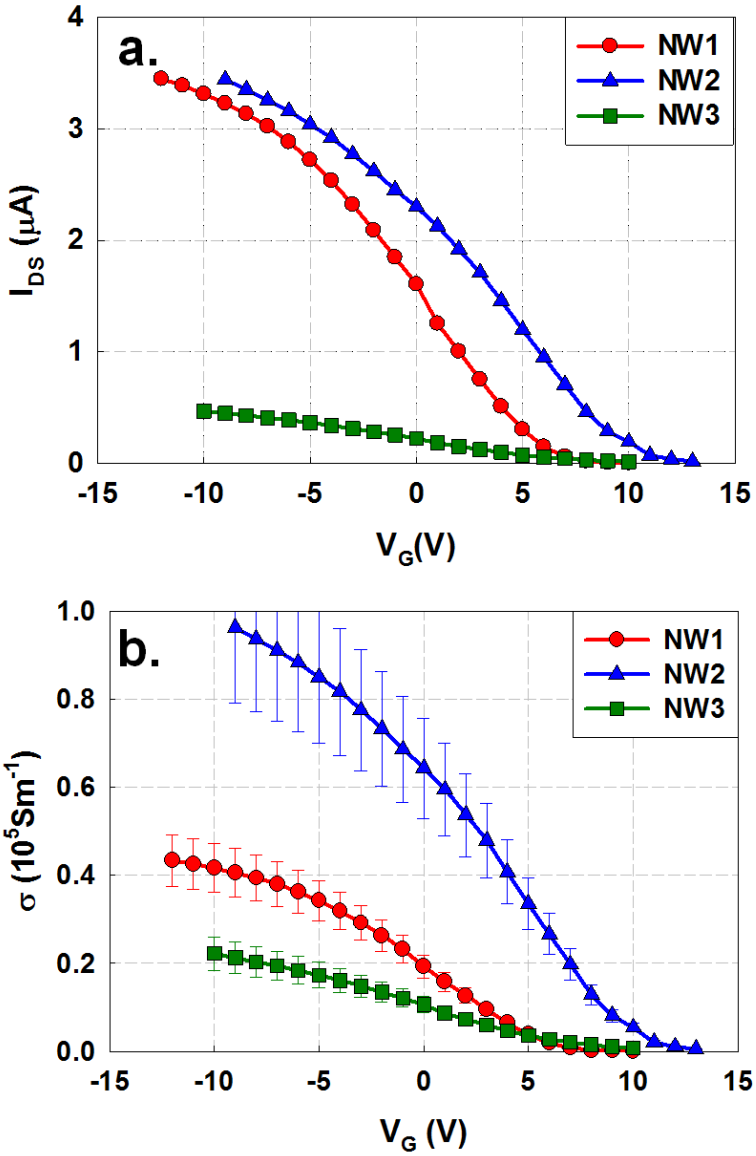

Figure 2.7 (a) Source drain current and (b) electrical conductivity of the NWs as a function of gate voltage. (copyright American Chemistry Society)

To investigate the origin of high conductivity in the NWs, we estimated the field-effect mobility and hole concentration [31]. From the on-state I_{DS}-V_G data shown in Figure 2.7 (a), we can calculate, for each given V_G, the transconductance of the NWs as:

$$g_m = \frac{dI_{DS}}{dV_G} \qquad (2.4)$$

and the hole mobility as:

$$\mu = \frac{g_m L^2}{V_{DS} C} \qquad (2.5)$$

where C is the capacitance of the gate oxide, calculated from:

$$C = \frac{2\pi\varepsilon_0\varepsilon_r}{\cosh^{-1}((R+h)/R)} \qquad (2.6)$$

where h is the gate oxide thickness, R is the NW radius, ε_0 is the permittivity of the vacuum, and ε_r is the relative dielectric constant of the gate oxide. An empirical effective ε_r of 2.2 has been shown to fit very well with the finite element analysis of the gate oxide [32], which accounts for the actual model where the bottom of the nanowire is silicon oxide (ε_r ~4) and the surrounding/top of the nanowire is air (ε_r = 1). From the calculated mobility, one can also estimate the carrier concentration in the NWs from

$$n=\sigma/\mu e \qquad (2.7)$$

where e is the charge per electron.

Figure 2.8 (a) shows the hole concentration n in the Ge core as the gate voltage is varied. The calculated n falls in the range of ~(2-5)×10^{18} to 5×10^{19} cm^{-3} for NW2 & NW3, and within ~10^{18} to 10^{20} cm^{-3} for NW1 because of the thinner gate oxide thickness. This shows that surface Fermi level pinning and gate modulation can be utilized to achieve a very high doping concentration in the degenerate regime in a nominally 'dopant-free' NW. This can only be achieved in small diameter NWs such as the ones studied here ($\leq$ 25 nm), because of the comparable screening depth of the field effect which is in the range of 10-20 nm.

Figure 2.8 (b) plots the mobility as a function of hole concentration for the NWs. For NW1 and NW2, μ varies with n and peaks at $(4\text{-}5)\times10^{18}$ cm^{-3} and for NW3 at 10^{19} cm-3. At higher n, μ decreases with increasing n, suggesting that acoustic phonon scattering is significant [6]. In the acoustic phonon scattering regime, μ can be written as $\mu \propto E^{(-1/2)}$ where E is the carrier energy and is larger for higher concentrations [6]. The downward bending of the μ vs. n plot at lower n is perhaps due to the contact and series resistance presented in the two-point I-V measurements, and hence may not be the true representative of the μ at low n. The mobility is lower in the thinnest nanowire (NW3) compared to the thicker ones (NW1 & NW2), suggesting that surface scattering becomes significant when the diameter is very small. On the other hand, the reduction in mobility from NW2 to NW1 is presumably due to variation in defect concentration in the NWs, which could have been unintentionally induced during NW growth. The contact and series resistance possibly presented in the two-terminal I-V measurements could have also contributed to the variation in the observed mobility. Nevertheless, if we compare the mobility of the NWs with bulk Ge (Figure 2.8 (b)), we find that the mobility of the NWs is comparable and in the case of NW2 , even higher than that of bulk Ge. The high mobility is a result of the two important attributes of the core-shell NWs discussed previously: first, the NWs are nominally dopant-free such that the impurity scattering is suppressed; second, the passivation of the Ge core by the Si shell significantly decreases the surface charge density and hence weakens the surface scattering. The lower mobility in NW1 and NW3 suggests that further optimization of the NW quality and surface passivation will be needed in order to more consistently achieve high mobility in the core-shell NWs.

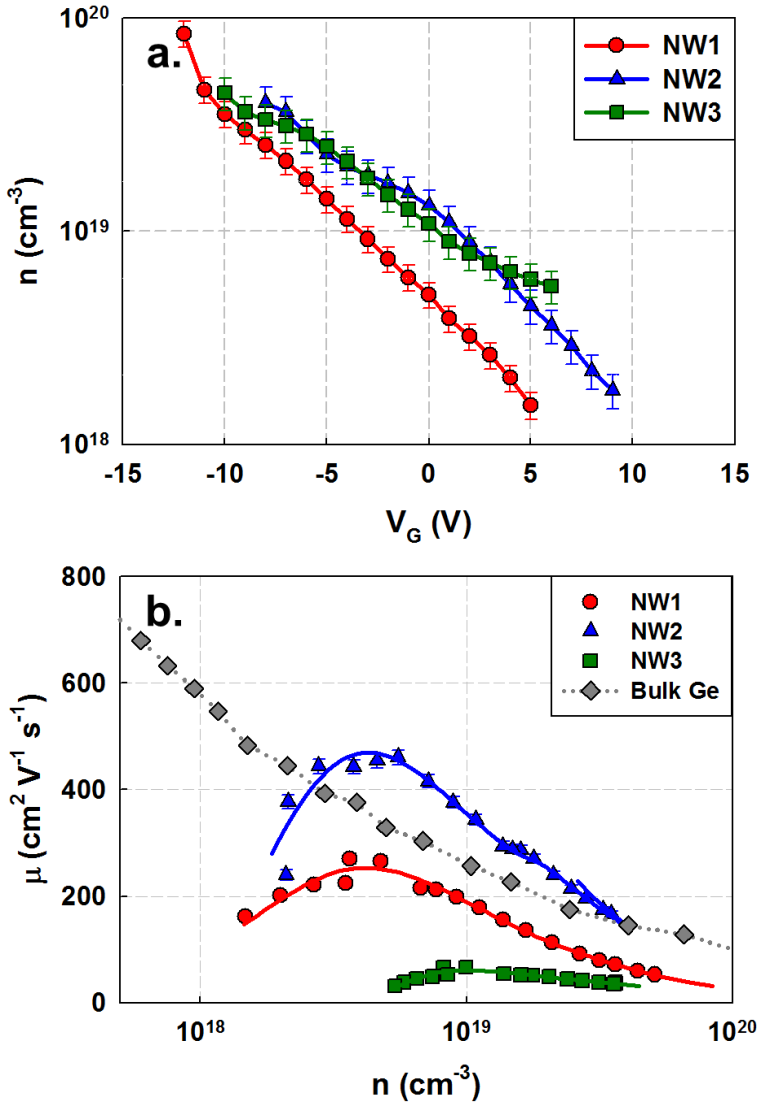

Figure 2.8 Gate modulated hole concentration and mobility of the NWs. (a) Hole concentration as a function of gate voltage (b) Mobility vs. hole concentration of the NWs along with p-type Ge (from Ref. [33]). (copyright American Chemistry Society)

To further illustrate the relative roles of phonon scattering and impurity scattering, the temperature dependent mobility of the NWs was measured and compared to p-type bulk Ge [33, 34], as shown in Figure 2.9 (low temperature data for NW3 was not available). The NW mobility is the average mobility obtained from the linear I_{DS}-V_G regime at each

temperature. For bulk Ge, the mobility increases as the dopant concentration decreases while it generally decreases with temperature due to acoustic phonon scattering. For the NWs studied here, the absolute values as well as the temperature dependence of μ are similar to that of bulk Ge with dopant impurity concentrations ranging from 1.1 to 4.9×10^{18} cm^{-3} for NW2 and 1.2×10^{19} to $5.8\times10^{19}cm^{-3}$ for NW1, clearly showing that the effective impurity concentration in the NWs are much lower than the carrier concentrations n. It also suggests a higher impurity concentration in NW2 compared to NW1, presumably due to unintentional doping, as discussed above.

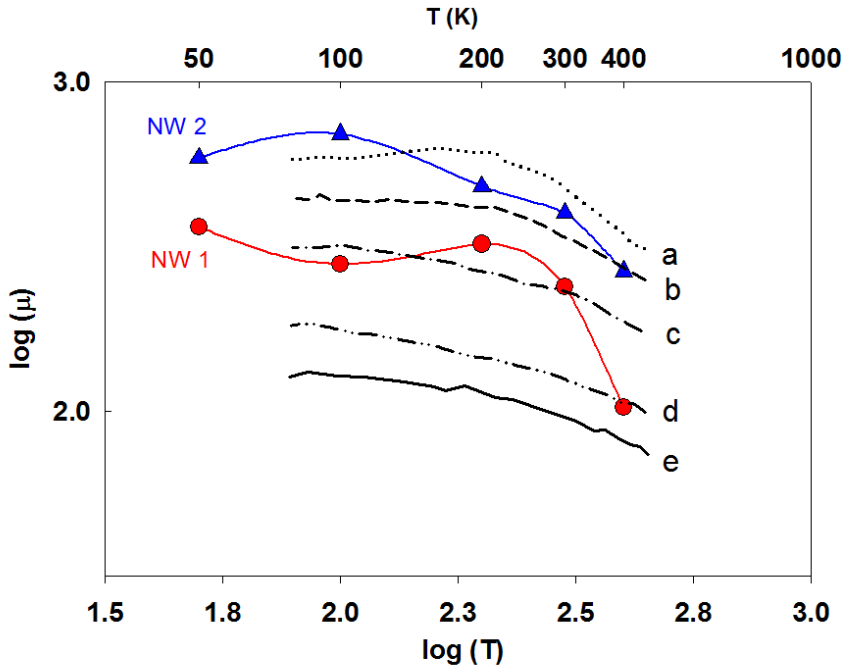

Figure 2.9 Temperature dependent mobility of the NWs and bulk p-Ge. Bulk Ge data was adapted from Ref. [33] with the following dopant (Gallium) concentrations: (a) 1.1×10^{18} cm^{-3}, (b) 4.9×10^{18} cm^{-3}, (c) 1.2×10^{19} cm^{-3}, (d) 5.8×10^{19} cm^{-3}, (e) 1×10^{20} cm^{-3}. (copyright American Chemistry Society)

2.3.2 Thermopower of Ge/Si core/shell nanowires

Now we turn our discussion to the gate modulated thermopower in the core-shell NWs. As shown in Figure 2.5 (b), the thermoelectric voltage is linearly related to the measured temperature difference between the two electrodes (2 and 3) under various gate voltages. We have also checked the leakage current between the gate electrode (Si substrate) and the NWs, and found it to be negligible, which is shown in Figure 2.10. The measured S under various gate voltages is shown in Figure 2.11 (a). The measured positive values of S show that holes are the majority carriers (Note: S is defined as $-\frac{dV_S}{d\Delta T}$), consistent with the I_{DS}-V_G measurements. Besides, S increases as V_G is raised to larger positive values, which is also consistent with the p-type characteristics of the NWs. For the NWs studied here, S can be modulated within a range of 175±2 to ~ 409±6 V/K by changing the gate voltage.

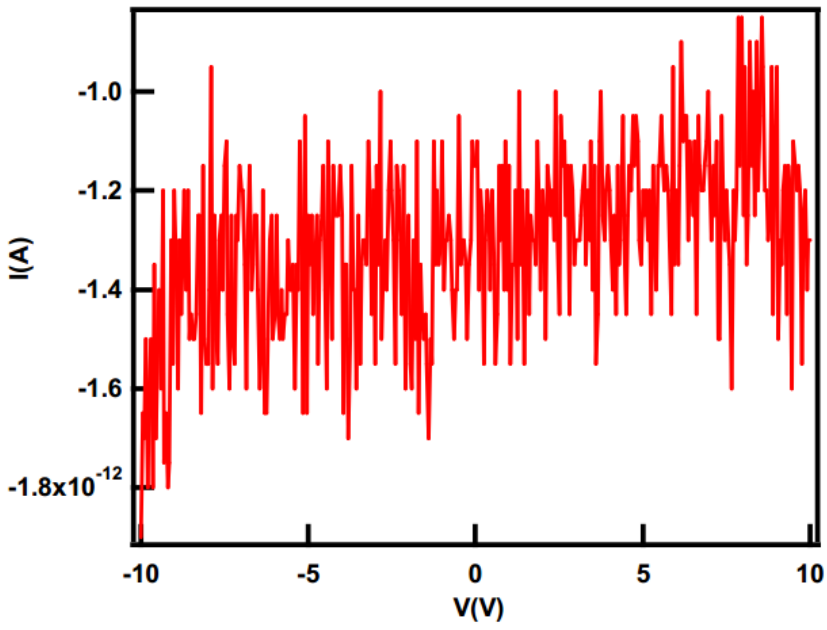

Figure 2.10 Typical measured I-V between a Si substrate (gate electrode) and a nanowire, showing a well-insulated gate oxide (copyright American Chemistry Society)

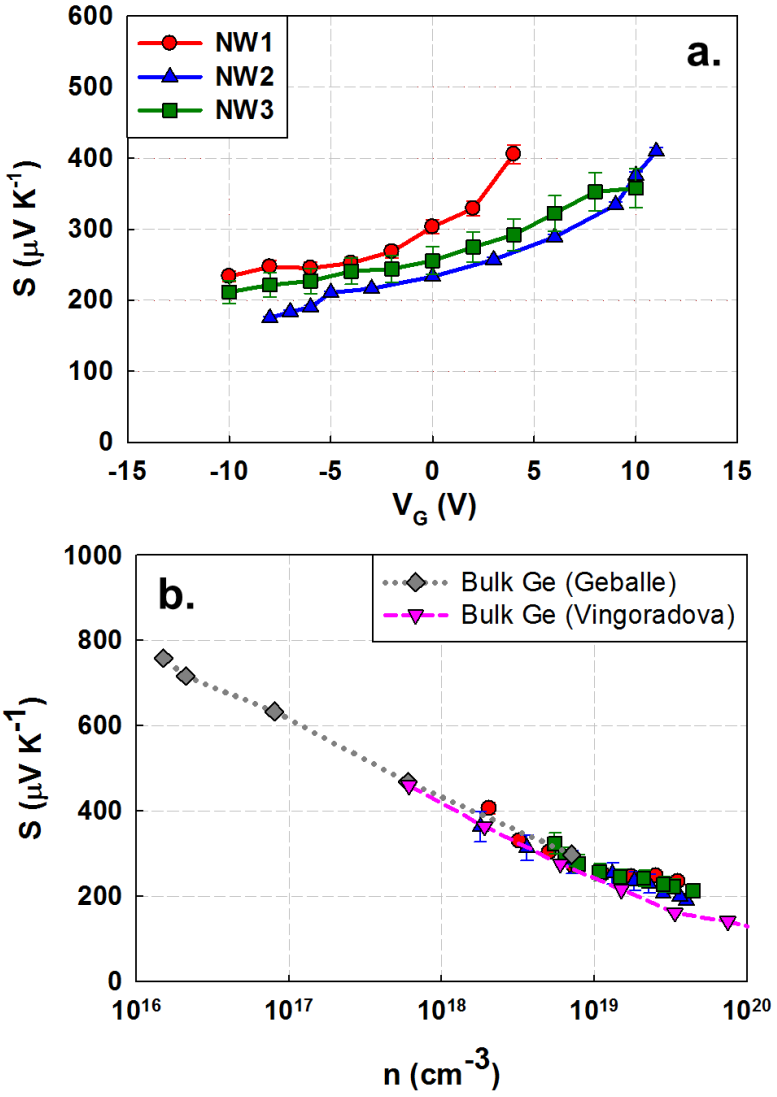

Figure 2.11 Gate modulated thermopower of Ge-Si core-shell NWs. (a) Seebeck coefficient of the NWs under various gate voltages. (b) Seebeck coefficient as a function of hole concentration of the NWs and bulk p-Ge. (copyright American Chemistry Society)

The gate modulation provides an effective means to investigate the relationship between *S* and carrier concentration within a range of ~(1-5)×10^{18} to ~5×10^{19} cm^{-3}. As shown in Figure 2.11 (b), *S* decreases monotonically as *n* increases, as expected. More

interestingly, *S* vs. *n* plots of the NWs fall into the same curve as that of p-type bulk Ge [35, 36], suggesting that *S* in the NWs, even with diameters down to ~11 nm, does not deviate significantly from that of a bulk system, even though the mobility in the NWs behaves quite differently.

The similarity of thermopower between the Ge NWs and bulk Ge suggests that the electronic structure in these NWs is still bulk-like and that the quantum confinement effect is not significant. As studied by Liang *et al.*[37], the subband energy separation is only a few meV for a 15 nm Ge NW, much smaller than k_BT (~ 26 meV) at 300 K. The diameter of a Ge NWs has to be smaller than 5 nm in order to see a pronounced quantum confinement effect[37]. Therefore, we do not expect the quantum confinement effect plays a large role in the observed Seebeck coefficient at room temperature, similar to the case of ~20-nm-diameter InAs NWs where the quantum effect was only observed at low temperature [25].

2.3.3 Power factor of Ge/Si core/shell nanowires

Finally, we present the power factor ($S^2\sigma$) vs. carrier concentration in the Ge/Si core-shell NWs and compare them with bulk Ge, as shown in Figure 2.12. Similar to bulk Ge, there is an optimal carrier concentration for the peak power factor for NWs. The optimal concentration lies within (2-4)×$10^{19}$$cm^{-3}$. The peak values of the power factor are the highest in NW2 (36±6 μW.cm^{-1}.K^{-2}), similar between NW1 (24±4 μW.cm^{-1}.K^{-2}) and bulk Ge (27 μW.cm^{-1}.K^{-2}), and finally lowest in NW3 (10±2 μW.cm^{-1}.K^{-2}). This shows that the power factor is clearly correlated with the mobility (Figure 2.11 (b)).

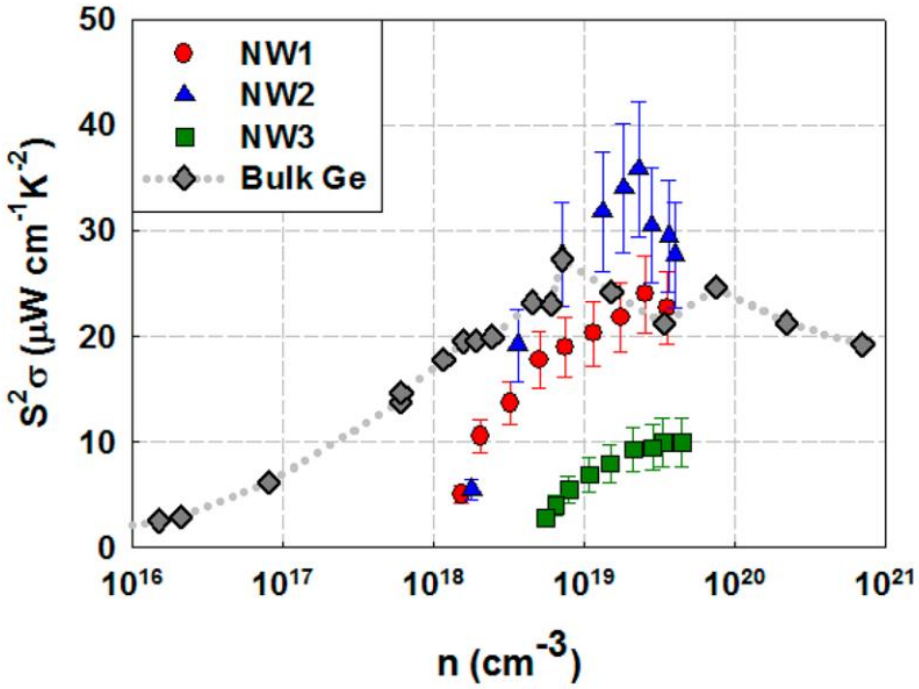

Figure 2.12 Power factor ($S^2\sigma$) vs carrier concentration of the NWs and bulk p-Ge. (copyright American Chemistry Society)

This can be readily understood from the formula for S and σ, as the former depends on the n (and slightly on scattering mechanism [6]) and the latter on both n and μ. Thereby, at constant n, a higher μ leads to a higher power factor. In particular, for NW2, the peak power factor is increased by more than 30% over that of p-type bulk Ge, suggesting the promise of exploiting the high carrier mobility of the hole gas in core-shell heterostructure NWs to enhance the power factor. Previously, a similar approach has been explored by using modulation-doped nanocomposites of Si-Ge alloys, which showed improved power factor via increased carrier mobility[38, 39]. Our present study, however, represents the 'extreme' case of modulation doping, namely, strongly degenerate hole gas in nominally 'dopant-free' Ge NWs. As a result, the relative

enhancement ratio as well as the absolute value of the power factor for NW2 is considerably higher in our case.

2.4 Conclusion

In conclusion, we have presented the first modulated thermoelectric power factor measurement on single Ge/Si core-shell NWs with Ge core diameters ranging from 11-25 nm. It was found that surface Fermi level pinning introduces a high concentration interface hole gas in the dopant-free Ge core and the field effect further increases the concentration into the strong degenerate regime. As a result, the gate modulated core-shell NWs offer an excellent and convenient platform to probe the relationship between the thermoelectric power factor and carrier concentration. Absolute values as well as the temperature dependence of carrier mobility for the NWs were compared to bulk Ge, and it was revealed that the suppressed ionized impurity and surface charge scattering could lead to higher mobility in certain nanowires. The dependence of the Seebeck coefficient on the carrier concentration for the NW samples studied here still follows the behavior of bulk Ge, indicating that the electronic structure is still bulk-like and that the quantum confinement effect is not significant at room temperature within the NW diameter range studied here. The results also suggest that core-shell heterostructures coupled with field effect modulation is an effective way to fine tune and to enhance the power factor, providing a new mechanism to improve the thermoelectric figure of merit in NWs in addition to the existing phonon boundary scattering approach[40-42]. Meanwhile, further optimization of the NW quality as well as better control over surface passivation will likely lead to higher mobility and power factor.

2.5 Acknowledgements

This chapter, in full, is a reprint of the material as it appears in Nano Letters, Volume 13, 2013. Jaeyun Moon, Ji-Hun Kim, Zack CY Chen, Jie Xiang, Renkun Chen. The dissertation author was the primary investigator and author of this paper.

2.6 References

1. Majumdar, A. *Science* **2004,** 303, (5659), 777-778.

2. Rowe, D. M., *Thermoelectrics handbook : macro to nano*. CRC/Taylor & Francis: Boca Raton, **2006**.

3. Snyder, G. J.; Toberer, E. S. *Nat Mater* **2008,** 7, (2), 105-114.

4. Vineis, C. J.; Shakouri, A.; Majumdar, A.; Kanatzidis, M. G. *Adv Mater* **2010,** 22, (36), 3970-3980.

5. Lan, Y. C.; Minnich, A. J.; Chen, G.; Ren, Z. F. *Adv Funct Mater* **2010,** 20, (3), 357-376.

6. Lundstrom, M., *Fundamentals of carrier transport*. 2nd ed.; Cambridge University Press: Cambridge, U.K. ; New York, 2000; p xix, 418 p.

7. Hicks, L. D.; Dresselhaus, M. S. *Phys Rev B* **1993,** 47, (19), 12727-12731.

8. Hicks, L. D.; Dresselhaus, M. S. *Phys Rev B* **1993,** 47, (24), 16631-16634.

9. Garnett, E. C.; Tseng, Y. C.; Khanal, D. R.; Wu, J. Q.; Bokor, J.; Yang, P. D. *Nat Nanotechnol* **2009,** 4, (5), 311-314.

10. Lieber, C. M.; Wang, Z. L. *Mrs Bull* **2007,** 32, (2), 99-108.

11. Xiang, J.; Vidan, A.; Tinkham, M.; Westervelt, R. M.; Lieber, C. M. *Nat Nanotechnol* **2006,** 1, (3), 208-213.

12. Xiang, J.; Lu, W.; Hu, Y. J.; Wu, Y.; Yan, H.; Lieber, C. M. *Nature* **2006,** 441, (7092), 489-493.

13. Wu, Y.; Xiang, J.; Yang, C.; Lu, W.; Lieber, C. M. *Nature* **2004,** 430, (6995), 61-65.

14. Tian, B. Z.; Zheng, X. L.; Kempa, T. J.; Fang, Y.; Yu, N. F.; Yu, G. H.; Huang, J. L.; Lieber, C. M. *Nature* **2007,** 449, (7164), 885-889

15. Chen, J.; Zhang, G.; Li, B. W. *Nano Lett* **2012,** 12, (6), 2826-2832.

16. Wingert, M. C.; Chen, Z. C. Y.; Dechaumphai, E.; Moon, J.; Kim, J. H.; Xiang, J.; Chen, R. K. *Nano Lett* **2011,** 11, (12), 5507-5513.

17. Hu, M.; Giapis, K. P.; Goicochea, J. V.; Zhang, X. L.; Poulikakos, D. *Nano Lett* **2011,** 11, (2), 618-623.

18. Hu, M.; Zhang, X. L.; Giapis, K. P.; Poulikakos, D. *Phys Rev B* **2011,** 84, (8), 085442

19. Markussen, T. *Nano Lett* **2012,** 12, (9), 4698-4704.

20. Chen, J.; Zhang, G.; Li, B. W. *J Chem Phys* **2011,** 135, (10), 104508.

21. Prasher, R. *Appl Phys Lett* **2006,** 89, (6), 063121.

22. Yang, R. G.; Chen, G.; Dresselhaus, M. S. *Nano Lett* **2005,** 5, (6), 1111-1115.

23. Pokatilov, E. P.; Nika, D. L.; Balandin, A. A. *Phys Rev B* **2005,** 72, (11), 113311.

24. Liang, W. J.; Hochbaum, A. I.; Fardy, M.; Rabin, O.; Zhang, M. J.; Yang, P. D. *Nano Lett* **2009,** 9, (4), 1689-1693.

25. Tian, Y.; Sakr, M. R.; Kinder, J. M.; Liang, D.; MacDonald, M.; Qiu, R. L. J.; Gao, H. J.; Gao, X. P. A. *Nano Lett* **2012,** 12, (12), 6492-6497.

26. Lu, W.; Xiang, J.; Timko, B. P.; Wu, Y.; Lieber, C. M. *Proceedings of the National Academy of Sciences of the United States of America* **2005,** 102, (29), 10046-10051.

27. Lee, S. M.; Cahill, D. G.; Allen, T. H. *Phys Rev B* **1995,** 52, (1), 253-257.

28. Cahill, D. G. *Rev Sci Instrum* **1990,** 61, (2), 802-808.

29. Cahill, D. G. *Rev Sci Instrum* **2002,** 73, (10), 3701-3701.

30. Vanwees, B. J.; Vanhouten, H.; Beenakker, C. W. J.; Williamson, J. G.; Kouwenhoven, L. P.; Vandermarel, D.; Foxon, C. T. *Phys Rev Lett* **1988,** 60, (9), 848-850.

31. Khanal, D. R.; Wu, J. *Nano Lett* **2007,** 7, (9), 2778-2783.

32. Wunnicke, O. *Appl Phys Lett* **2006,** 89, (8).

33. Golikova, O. A.; Moizhes, B. Y.; Stil'bans, L. S. *Sov. Phys. -Solid State* **1962,** 3, (10), 2259-2265.

34. Jacoboni, C.; Nava, F.; Canali, C.; Ottaviani, G. *Phys Rev B* **1981,** 24, (2), 1014-1026.

35. Geballe, T. H.; Hull, G. W. *Phys Rev* **1954,** 94, (5), 1134-1140.

36. Vinogradova, M. N.; Golikova, O. A.; Dubrovskaya, I. N.; Moizhes, B. Y. *Sov. Phys. -Solid State* **1963,** 5, 1204.

37. Liang, G. C.; Xiang, J.; Kharche, N.; Klimeck, G.; Lieber, C. M.; Lundstrom, M. *Nano Lett* **2007,** 7, (3), 642-646.

38. Yu, B.; Zebarjadi, M.; Wang, H.; Lukas, K.; Wang, H.; Wang, D.; Opeil, C.; Dresselhaus, M.; Chen, G.; Ren, Z. F. *Nano Lett* **2002,** 12, 2077-2082.

39. Zebarjadi, M.; Joshi, G.; Zhu, G. H.; Yu, B.; Minnich, A.; Lan, Y. C.; Wang, X. W.; Dresselhaus, M.; Ren, Z. F.; Chen, G. *Nano Lett* **2011,** 11, (6), 2225-2230.

40. Hochbaum, A. I.; Chen, R. K.; Delgado, R. D.; Liang, W. J.; Garnett, E. C.; Najarian, M.; Majumdar, A.; Yang, P. D. *Nature* **2008,** 451, (7175), 163-U5.

41. Li, D. Y.; Wu, Y. Y.; Kim, P.; Shi, L.; Yang, P. D.; Majumdar, A. *Appl Phys Lett* **2003,** 83, (14), 2934-2936.

42. Boukai, A. I.; Bunimovich, Y.; Tahir-Kheli, J.; Yu, J. K.; Goddard, W. A.; Heath, J. R. *Nature* **2008,** 451, (7175), 168-171.

CHAPTER 3 : High performance multi-scaled nanostructured spectrally selective coating for concentrating solar power

3.1 Introduction

Solar energy can potentially play a significant role in the global energy supply. [1] There are two main methods for generating electricity from sunlight: direct solar-electricity conversion using photovoltaic (PV) solar cells and concentrating solar power (CSP) which generates electricity from solar thermal energy.[2, 3] Despite PV technology's rapid development, CSP still offers several unique advantages: higher energy-conversion efficiency, higher thermal energy storage capability (specifically, a higher capacity factor[4]), and the potential to retrofit current coal power plants. Therefore, large-scale deployment of CSP could enable a higher overall penetration of solar energy. [5] As of 2011, the cumulatively installed CSP capacity reached ~1.17GW,and ~17GW of CSP is under development worldwide. [6]

Among the various components in a CSP system, the solar absorber plays a critical role in overall system performance. To increase the Carnot efficiency of the power generation system, it is desirable that the temperature of the heat transfer fluid (HTF) is 600℃ or higher. [7] In order to increase the temperature of the receiver, a solar absorber has to maximally absorb solar energy while minimizing losses due to black body emission. At a receiver temperature of 500-800℃, black body emission peaks at wavelengths longer than 2μm. Most energy within the solar spectrum is located at

wavelengths below 2μm, allowing for the possibility of optimizing receiver performance through tuning the spectral absorptivity (equivalent, at equilibrium, to spectral emissivity). As most materials do not naturally have the desired behavior, engineered composites are needed. Figure 3.1 (a) illustrates the schematic diagram of a solar absorber with a SSC. An ideal SSC has to exhibit high spectral absorptivity, α_s, in the solar spectrum (0.3-2.0μm wavelengths), and low spectral emissivity, ε_{IR}, in the IR spectrum (2.0μm to 15μm wavelengths) (Figure 3.1 (b)).

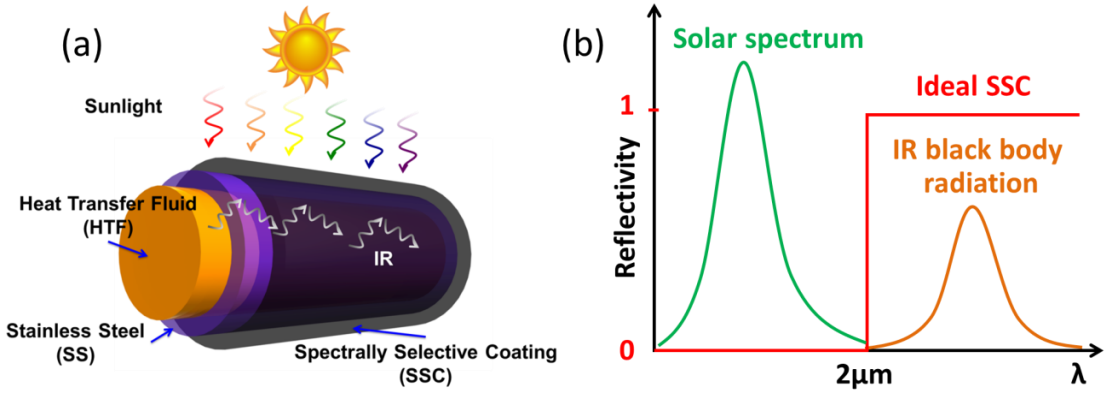

Figure 3.1 Spectrally selective coating (SSC) for concentrated solar power. (**a**) Schematic of a solar absorber with stainless steel (SS) tube coated with the SSC. (**b**) Optical reflectance of an ideal SSC. (copyright Elsevier)

The optical performance of the SSC is usually characterized by the ratio of solar absorptivity and IR emissivity at a given operation temperature, which directly dictates the photo-thermal conversion efficiency of solar receivers, [8]

$$\eta_{th} = 1 - \frac{Q_{loss}}{Q_{in}} = \alpha_{S,eff} - \frac{\varepsilon_{IR,eff}\sigma(T_R^4 - T_0^4)}{CI} \qquad (3.1)$$

where the effective IR emissivity, $\varepsilon_{IR,eff}$, is defined as,

$$\varepsilon_{IR,eff} = \frac{\int_0^\infty \varepsilon(\lambda)\left[I_\lambda(T_R,\lambda) - I_\lambda(T_0,\lambda)\right]d\lambda}{\int_0^\infty \left[I_\lambda(T_R,\lambda) - I_\lambda(T_0,\lambda)\right]d\lambda} \quad (3.2)$$

and the effective solar absorptivity, $\alpha_{s,eff}$,is determined by,

$$a_{S,eff} = \frac{\int_0^{¥} a(/)I_S(/)d/}{\int_0^{¥} I_S(/)d/} \quad (3.3)$$

In the equations, Q_{in} is heat input from the concentrated solar flux, and Q_{loss} is heat loss due to radiation, conduction, and convection heat transfer (negligible when the receiver is placed in an evacuated enclosure). The Stefan-Boltzmann constant, is σ (=5.67×10^{-8} $Wm^{-2}K^{-4}$,), C stands for the solar concentration ratio and I is the solar insolation. $I_S(\lambda)$ and I_λ (T, λ) are the spectral intensities of solar insolation and blackbody radiation at T, respectively. T_R and T_0 correspond to the temperature of the receiver and ambient, respectively. The spectral absorptivity and emissivity of the SSC are denoted by α(λ) and ε(λ), respectively. When the temperature of the HTF is 600°C or higher for high Carnot efficiency[7], the surface temperature of the SSC would be 700℃ or higher. It is therefore important for SSCs to possess high $\alpha_{s,eff}$ and low $\varepsilon_{IR,eff}$ to satisfy both high operation temperature and power conversion efficiency.

There has been an extensive search for mid- to high- temperature SSC materials. [9] Typical SSC structures fall into one or several of the following schemes: 1. Intrinsic selective materials, the simplest structure usually in the form of thin films with proper intrinsic material selectivity[9]. 2. Semiconductor-metal tandems, which are made from semiconductors with proper bandgaps (Eg ~ 0.5eV–1.26 eV) that absorb solar radiation

in tandem with an underlying metal that provides high IR reflectance. The main drawbacks of this structure include the need for an anti-reflection coating, oxidation of the semiconductors at elevated temperatures, and non-scalable processes for producing semiconductor thin films such as CVD[10] or vacuum sputtering. 3. Multilayer absorbers, which use multilayer stacks of metals and dielectrics to achieve high selectivity due to the interference effect. This scheme is limited by the high cost of the multi-stack fabrication process, such as sputtering and CVD, [11, 12] as well as high-temperature instability. [13] 4. Textured surfaces, which consist of porous and nano-scale structures for the required spectral selectivity through optical trapping of sunlight. [14] The spectral emittance can be adjusted by modifying the microstructure of the coating. However, these highly textured metal surfaces tend to degrade quickly at elevated temperature. [15, 16] 5. Metal-dielectric composites, which utilize a highly solar-absorbent and IR-transparent material deposited onto a highly IR-reflective metal substrate. The 'black' absorbing layer is a cermet of fine metal particles in a dielectric matrix. [17-19] This design offers a very high degree of flexibility for tuning the absorption and scattering cutoff wavelengths by particle and matrix constituents, particle sizes and concentrations, coating thickness, etc.

Based on the above discussion, it is evident that an ideal and practical SSC material and scheme has yet to be identified. [20, 21] Current SSCs typically have a high solar absorptivity but they either need high cost and vacuum processes, such as CVD and sputtering, or do not have a good spectral selectivity at around 1-2μm. In addition, most SSC materials degrade after prolonged operation at high temperatures, which is unsatisfactory for future CSP operation at high temperature ($\geq$700 ^{o}C). In this Letter, we demonstrated a high-performance SSC based on a novel design of multi-scaled

semiconductor particles with sizes ranging from ~10 nm to ~10μm. The micro/nano multi-scale structures, made from a low-cost and scalable coating process, were shown to yield high optical performance by both theoretical modeling and optical measurements.

3.2 Experiments and Modeling

3.2.1 Modeling of Multi-scaled SSCs

The design of the multi-scaled SSC described in this Letter combines several features offered by the existing SSCs summarized above. As shown in Figure 3.2, our approach is based on semiconductor nanoparticles deposited on highly IR-reflective metal surfaces, which utilizes the concepts of the 'intrinsic semiconductor', ‘textured surface’ and 'metal-dielectric composite' approaches. First, we employed a semiconductor material with a suitable band gap for the selectivity at around 1-2 μm wavelength, which is similar to the 'intrinsic semiconductor' scheme. Secondly, we utilized multi-scale structures with a wide range of particle sizes in order to induce an appropriate surface morphology leading to higher light absorption. Since the multi-scaled nanostructures increase light trapping efficiency ('textured surfaces' scheme), there is no need for an additional anti-reflection coating layer. This is parallel to an extremely efficient anti-reflection coating in PV solar cells by using nanostructures to reduce the impedance mismatch and enhance light trapping. [22] However, our multi-scaled structures can be readily achieved by a simple coating process, which is more cost effective than previously reported methods[22] using lithography and etching processes in crystalline Si.

Lastly, the composite structure of semiconductor powders and dielectric matrix reported here was inspired by the 'metal-dielectric composite' concept that is flexible and versatile.

As a guideline for the fabrications of the SSC structures, we simulate optical properties of a SSC material that is comprised of nanoparticles embedded in a dielectric host with its representative cross-sectional view shown in Figure 3.2 (a). An effective-medium-theory-based model was applied by approximating the nanostructured SSC to a two-layer geometry as shown in Figure 3.2 (b). The effective medium approximation treats the uniform nano-composite metamaterial (nanoparticles in the dielectric host) as an isotropic medium with a thickness of L1 and an effective permittivity determined by the permittivities of individual components, i.e. ε_p for nanoparticles and εh for the dielectric host, [23-25] and respective volumetric ratios. The surface-structured metamaterial with a thickness of L_2 can thus be treated as a gradient-refractive-index (GRIN) layer mixed between the uniform metamaterials and air. The GRIN layer is modeled by discretizing the material into infinitesimally thin layers in the vertical direction, each of which may be considered as a uniform medium. Determined by the particle filling ratio of the coating, the effective dielectric function for both uniform and GRIN layers follows the Maxwell–Garnett formalism or the Bruggeman mixing theory.[24] The GRIN layer gradually smoothes out the permittivity discontinuity between air and the uniform metamaterial layer, thus serving as a perfect anti-reflection layer.

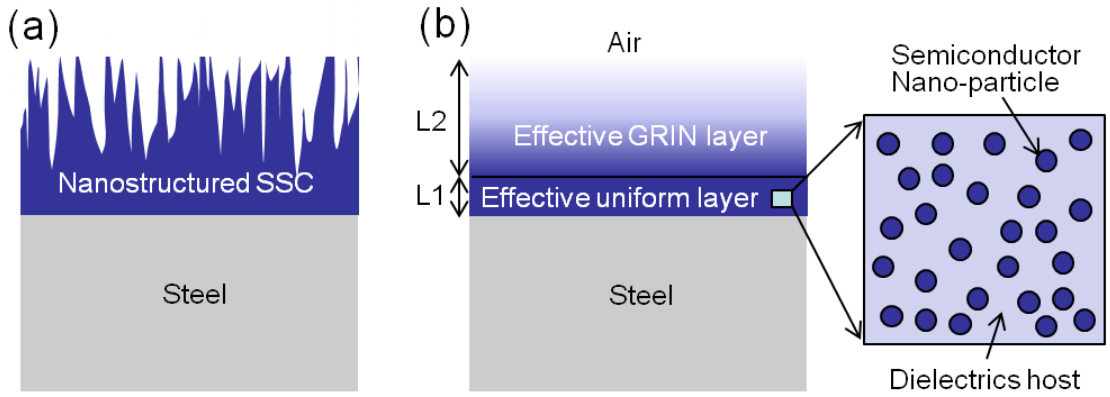

Figure 3.2 Optical modeling system for the SSC. (**a**) The nanostructured SSC is modeled by a multilayer system which is schematically shown in (**b**). The effective layer corresponds to the semiconductor nanoparticles in the dielectric host. (copyright Elsevier)

The reflectance of the total structure can be calculated using a transfer matrix method once the effective permittivities are known.[26] Figure 3.3 (a) shows numerically simulated reflectance spectra of the SSC with different nanoparticle filling ratios at normal incidence based on the Bruggeman mixing theory.[27] In the simulation, the uniform metamaterial layer is assumed to be made of intrinsic Si nanoparticles embedded in a SiO_2 host, with the corresponding permittivities taken from refs. 28 and 29. The GRIN layer is divided into 100 individual uniform layers with effective permittivities varying smoothly from air to that of the bulk layer. When the particle filling ratio exceeds 50%, a sharp change is observed in the reflectance spectra of the simulated coating near wavelengths of 1.1μm, corresponding to the bandgap of Si. Figure 3.3b shows a reflectance curve when the Si filling ratio is 75% as compared with the standard solar spectrum and the blackbody radiation spectrum at 700℃. The comparison indicates that the solar absorptivity, α, for the SSC device is close to 99% while its IR emissivity, ε, is about 4%. It is worth noting that the optical properties of the SSC layer with different

semiconductor and dielectric combinations are always similar, except that the cutoff wavelengths may shift according to the bandgap of the semiconductor.

From the calculations, it is clear that the following factors are the primary causes of the overall high performance. Firstly, the effective GRIN layer acts as a perfect light trapping or anti-reflection layer. In practice, the Bruggeman mixing theory used here will be a valid approximation when features of the layer are sub-wavelength to incident radiation (<300nm for visible light). Secondly, an appropriate nanoparticle material and its volumetric filling ratio are the key parameters for tuning the cutoff wavelength in the reflectance spectra. Lastly, a smooth steel layer underneath improves reflectance at IR wavelengths. The surface roughness of steel should be deep sub-wavelength at IR frequencies (typically <100nm) to reduce the IR absorption due to surface light trapping. Although not shown here, the calculated reflectance is almost invariant to light polarizations and incident angles, indicating the robustness of the SSC layer.

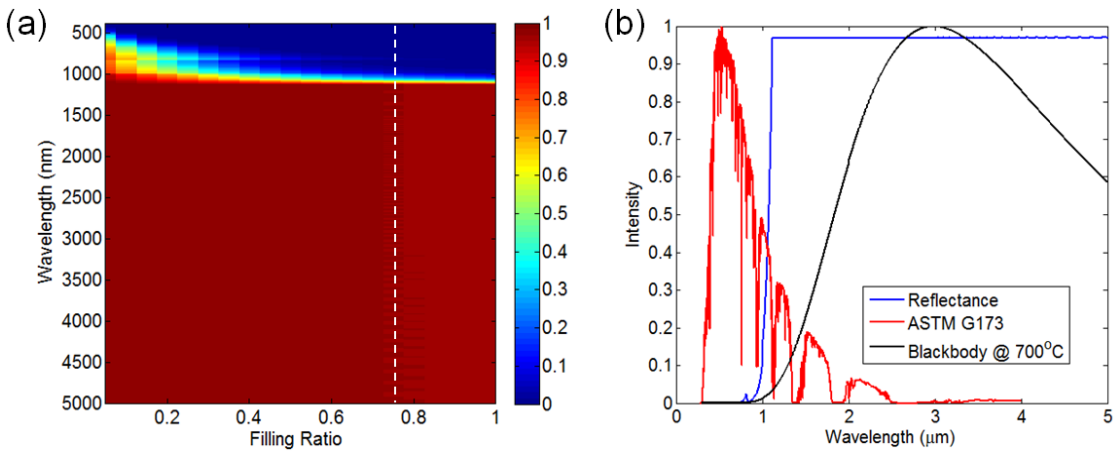

Figure 3.3 (**a**) Reflectance with respect to incident wavelengths and the volumetric filling ratios of the nanoparticles. (**b**) Reflectance of the SSC layer when the filling ratio of the nanoparticles is equal to 0.75, i.e., at the location marked by the dashed vertical line in (**a**). (copyright Elsevier)

3.2.2 Fabrication of Multi-scaled SSCs

To validate the new design, we used $Si_{0.8}Ge_{0.2}$ as a representative semiconductor material to fabricate SSCs. $Si_{0.8}Ge_{0.2}$ is expected to yield the desirable light absorptivity in VIS-NIR range (<1um) due to the intrinsic bandgap of $Si_{0.8}Ge_{0.2}$, ~1.04eV [30]. The $Si_{0.8}Ge_{0.2}$ powders of various sizes were prepared by a spark erosion process. Spark erosion is a process originally developed by Berkowitz and Walter[31] for rapid production of semiconductor and metallic powders. We recently modified the process for high-yield production of nano-sized powders.[32] Figure 3.4 (a) is a schematic diagram of the spark erosion process. Two electrodes of $Si_{0.8}Ge_{0.2}$ are mounted in a cell and connected to a pulsed power source. During the spark erosion process, a high temperature spark (micro-plasma) is produced and vaporizes the materials of charges (small pieces) and electrodes in the localized region. When the spark collapses, vaporized material and molten droplets are ejected into the dielectric liquid (liquid Ar in this case), where they are rapidly

quenched to produce clean nanoparticles with different sizes. In order to induce sparks, the charges and electrodes should be electrically conductive. Therefore, $Si_{0.8}Ge_{0.2}$ materials used for a spark erosion process were slightly doped by phosphorus (P). Following spark erosion, attrition milling was carried out with the spark eroded $Si_{0.8}Ge_{0.2}$ particles for optimizing the particle size distribution to increase the proportion of powders of several hundred nanometers, which are strong scatterers of the range of incident light wavelengths.

Figure 3.4 (b) and (c) show SEM and TEM pictures of the spark-eroded $Si_{0.8}Ge_{0.2}$ particles. These images show that the particles have a wide range of powder sizes, ranging from ~10 nm to 10 μm due to the high quenching rate presented in the spark erosion process. This is a distinct difference from many other particle synthesis techniques [33, 34], which usually yield mono-dispersed particle sizes. As we shall show later, the multi-scaled particles are very beneficial to SSC applications compared to the uniform ones.

A simple coating process was employed to deposit the particles onto a polished stainless steel (SS) surface. As shown in Figure 3.4 (d), the as-made $Si_{0.8}Ge_{0.2}$ particles were dispersed into an organic solvent, and the solution was sonicated to make a uniform mixture. Concentration of the solutions was controlled and kept consistent. The nanoparticle solution was then coated onto targeted substrates by drop casting. After the solvent dried, a coating film made of $Si_{0.8}Ge_{0.2}$ particles was formed on the SS substrate. The film thickness was controlled to ~100μm by adjusting the drop casting conditions. In order to demonstrate the effect of particle-size distribution, ~100-μm-thick films made

from commercial Si powders (Alfa Aesar) with average diameter of ~100 nm were also prepared using the same process.

We also performed brief high temperature tests for the SiGe coating at 750 ^{o}C for 1 hour in air environment. The particular condition was chosen because 750 ^{o}C is higher than the current operation temperature of the high temperature CSP (550 ^{o}C) but lower than the melting point of $Si_{0.8}Ge_{0.2}$ (~1270℃). Even though this material can be used in a vacuum enclosure, the oxidation resistance is also desired in case the vacuum was unintentionally breached. Further systematic high temperature durability tests as well as oxidation protective coating need to be performed to evaluate the applicability of the new SSC for future CSP systems.

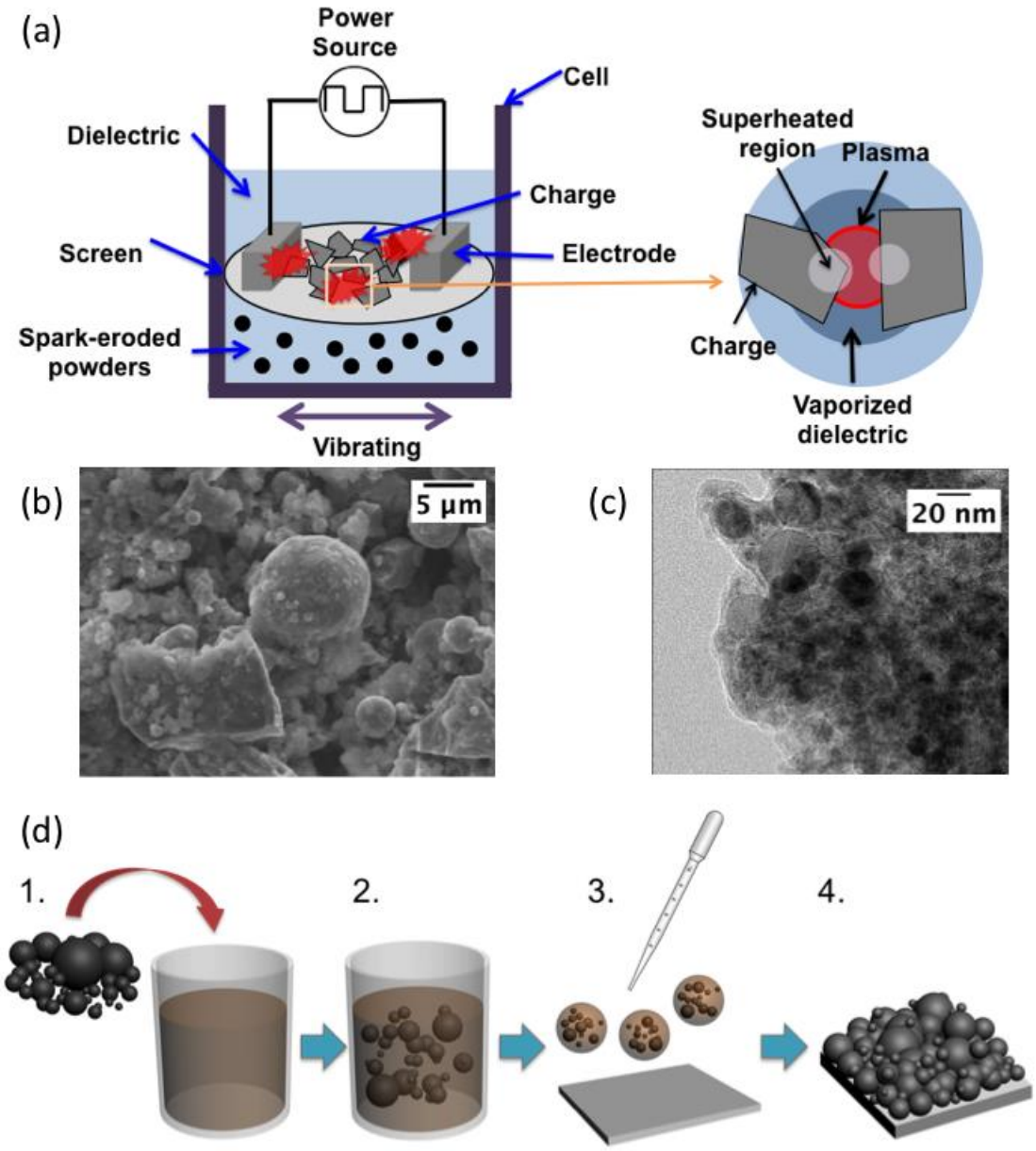

Figure 3.4 SSC sample preparation. (**a**) Schematic diagram of the spark erosion process. (**b**) SEM, (**c**) TEM of the spark-eroded $Si_{0.8}Ge_{0.2}$powders. (**d**) Schematic of the coating process for making SSC samples (copyright Elsevier)

3.3 Results and Discussion

The fabricated SSC samples were characterized by SEM. Figure 3.5 (a) and (b) show top-view SEM images of the SSC layer made by using spark-eroded Si-Ge particles. After deposition, micro-scale dome-shaped structures are built up by micro-sized spark-eroded particles. These micro-scale particles are covered with nano-scale powders as shown in Figure 3.5 (b), thus creating the multi-scale features. In order to study the effect of multi-scaled structure on light absorption, we also prepared mono-dispersed powder sample which was made using Si nanoparticles with uniform size- of ~100 nm, as shown in Figure 3.5 (c) and (d). Unlike spark-eroded Si-Ge particles, the top surface of the Si coating is quite smooth except for the roughness at the particle size scale. Figure 3.5 (e) and (f) show the SEM images of the same SSC before and after annealing at 750 ^{o}C for 1 hour in air, respectively. It is evident that the morphology of the SSC remains similar after the annealing test.

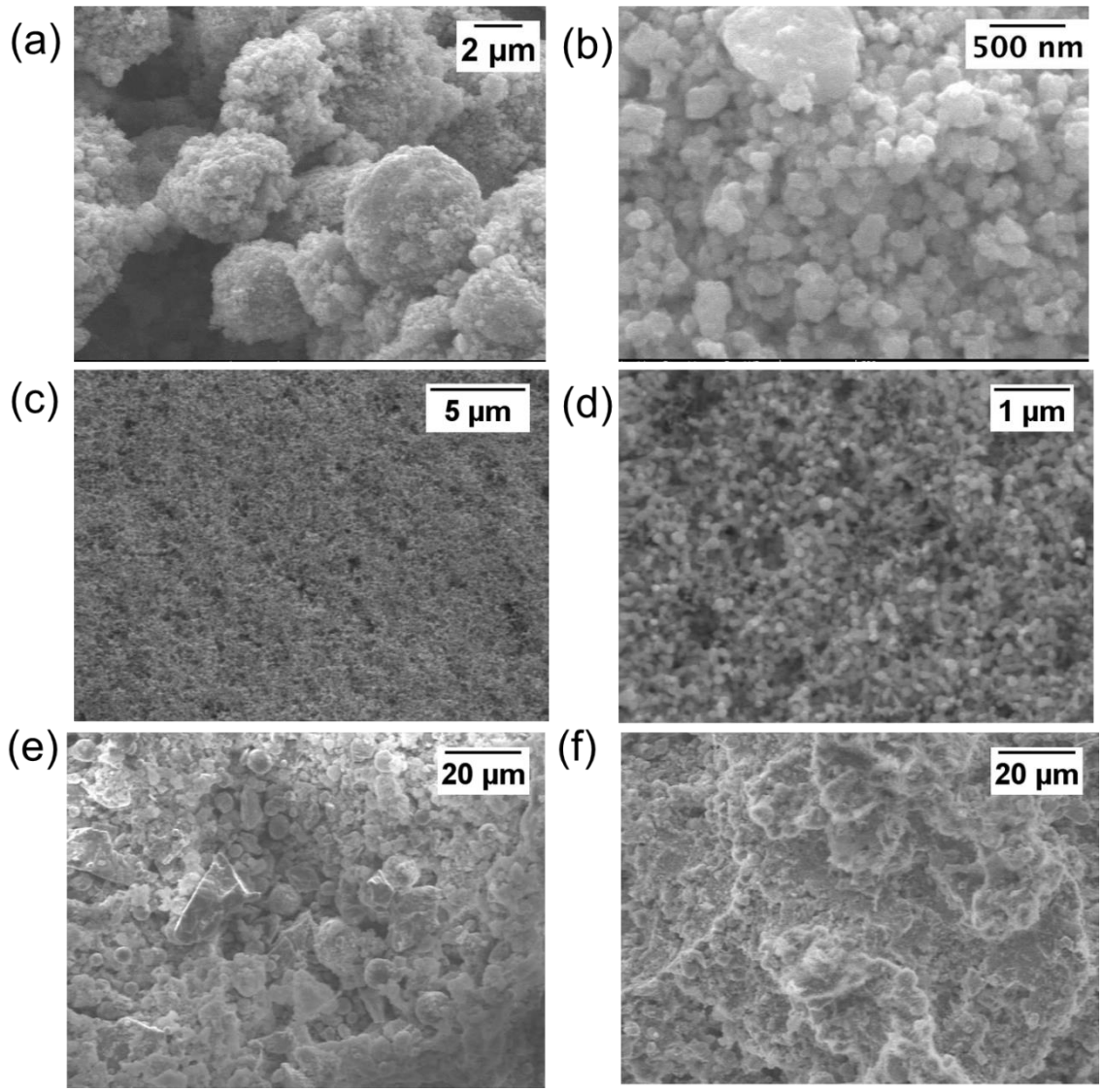

Figure 3.5 (**a-b**) SEM images of the SSC based on spark-eroded $Si_{0.8}Ge_{0.2}$ particles. (**c-d**) SEM images of the SSC made by mono-dispersed powders. SEM images of the same Si-Ge sample (**e**) before and (**f**) after annealing at 750 ^{o}C in air for 1 hour. (copyright Elsevier)

The optical reflectance of the SSCs was measured by a UV-visible spectrometer and directional emission at a temperature of 500℃ measured in a Fourier transform infrared (FTIR) spectrometer, with the results presented in Figure 3.6 (a) and (b), respectively. To characterize the SSCs in the UV-visible range, incident light from Xenon

lamp was focused onto the sample surface which was contained within an integration sphere capable of collecting all angles of scattered light. Collected spectra were analyzed by an ANDOR^{TM} Shamrock 303i spectrograph equipped with a Newton 920 CCD detector. High temperature IR emittance was characterized by an FTIR spectrometer (Mattson Galaxy5020) with custom built heated sample stage. The samples were kept under vacuum during measurement to reduce heat loss, and a maximum temperature of samples reached 500℃. A sample of Pyromark 2500 (Tempil) was used as a standard reference for the measurement, with directional emissivity data taken from ref [35]. As shown in Figure 3.6 (a), the multi-scaled SSC layers made from the spark-eroded powders have low reflectivity of 5-10% across the UV-NIR solar spectrum. In contrast, the SSC made from uniform Si nanoparticles shows much higher reflectivity (13-80%). This demonstrates the high light-trapping efficiency of the multi-scaled structures: if the particles are all micro-sized, light will be reflected from the surface of large particles; on the other hand, if the particles are all nano-sized, the uniform surface of the SSC layer will result in inefficient light trapping, as in the case of the control sample made by 100-nm Si nanoparticles. Similar multi-scaled structure has been achieved using lithographic patterning for enhanced light absorption in PV devices. [22, 36, 37] In addition to the light trapping effect, the lower bandgap of Si-Ge particles enables more absorption than Si particles in the spectrum range below bandgap of Si-Ge (~1.2 μm). And in the aspect of mass production, the approach we developed is based on multi-scaled particles naturally formed during the spark-erosion process and the following attrition milling, and hence is more readily applicable for large-scale applications such as CSP. Further optimization of the coating, including material selection, particle size distribution, and coating

morphology, is likely to reduce the solar reflectivity further, as shown in our simulation results (Figure 3.3 (a)). The optimal parameters such as the particle size range and distribution warrant further investigation.

Figure 3.6 (b) shows the directional spectral emittance of SiGe SSC layers at IR frequencies. Rough surfaces generally display isotropic (Lambertian) scattering and we can therefore expect the presented data to be representative of all-angle emission spectra. The SiGe sample shows low emission below 0.3 near the peak of 500℃ black body radiation which stems from the low absorption coefficient obtained by the light with energy below the bandgap of $Si_{0.8}Ge_{0.2}$,(~1.04 eV or 1.2 μm). The discrepancy between simulated and experimental emission spectra at IR is mainly attributed to the excitation of considerable hot carriers at elevated temperature.

We also evaluated the potential of the mutliscale structural SSCs for high temperature operation (≥700 ^{o}C). The blue curves in Figure 3.6 (a) and (b) show the reflectance of the Si-Ge SSC sample after annealing at 750℃ for 1hour in air. Even though $Si_{0.8}Ge_{0.2}$ can be oxidized at high temperature in air environment, we observed the annealed sample exhibited a small increase in the reflectance in the UV-Vis-NIR range. This coincides with the structural observation showing minimal morphological and structural changes of the particles after the annealing [Figure 3.5(e)-(g)]. In order to improve high temperature stability, a comprehensive study and oxidation degradation needs to be conducted in future researches. Furthermore, the application of high temperature durable materials having appropriate band gaps, such as conductive oxides, will be a promising approach.

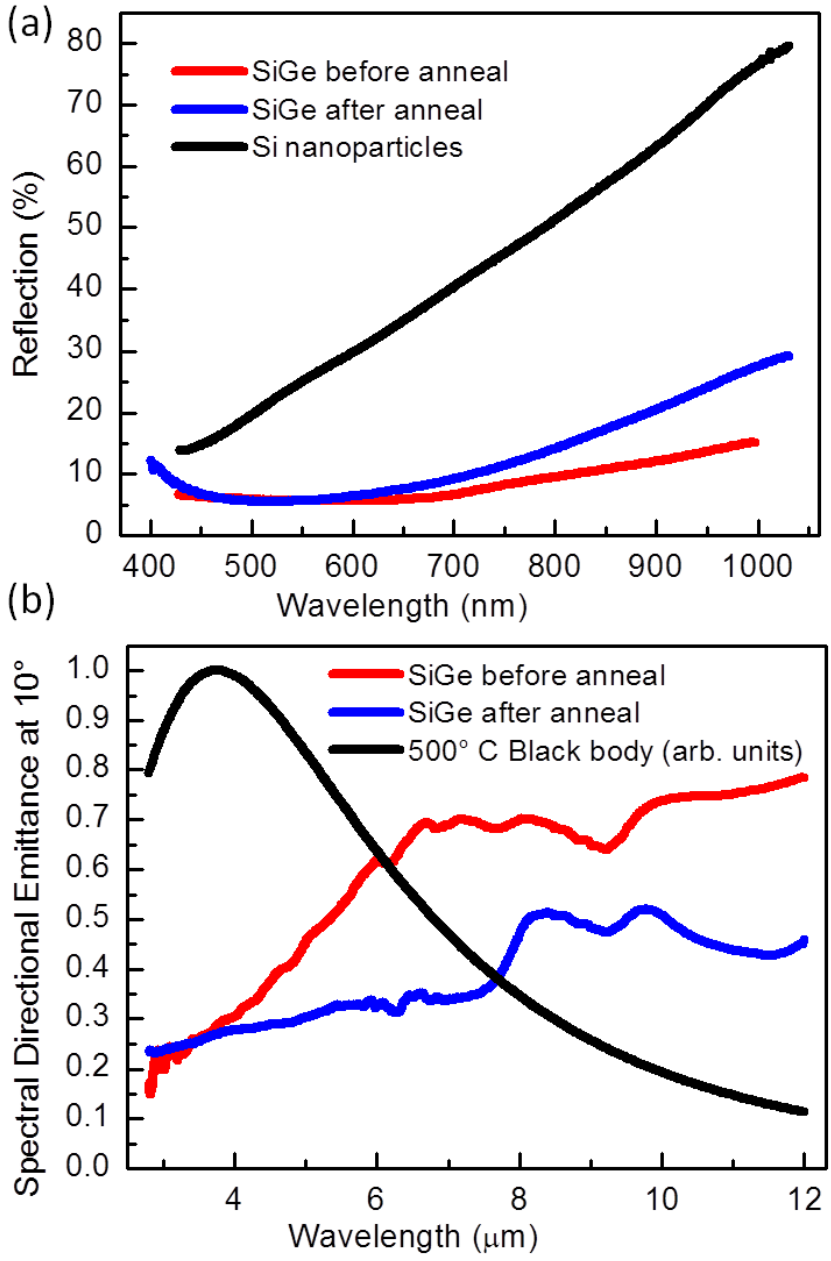

Figure 3.6 (a) Measured reflectance of the SSCs in the UV to near-IR regime. (**b**) Measured IR emission spectra at 500°C. The black curve in (**b**) is the normalized blackbody spectrum at 500 ^{o}C. (copyright Elsevier)

3.4 Conclusions

We reported the design and fabrication of a new SSC structure based on multi-scaled semiconductor nanostructures. The Si-Ge SSC is highly absorbent for short-wavelength photons (with energy higher than the semiconductor bandgap) and efficiently reflective for long-wavelength photons. The measured spectral solar reflectance (5-10%) and IR emissivity (<30%) of the SSC indicate high performance for CSP applications. We also found that the multi-scale features (10 nm–10 μm) of the particles have significantly enhanced the solar absorptivity compared to uniform nanoparticles due to the more efficient light trapping. The particles and the SSC are made by spark erosion and low-cost drop casting process, which is applicable for making large-scale solar absorbers. We anticipate the high solar absorptance and low IR emittance of the developed SSC will significantly benefit future high temperature CSP technologies by improving their maximum attainable temperature and thermal efficiency. In addition, the SSC shows the potential to maintain the multi-scale structure and optical properties after high temperature process. Further applications of the multi-scaled structure on high temperature materials and systematic high temperature durability tests will be performed to evaluate the applicability of the new SSC for future high temperature CSP systems.

3.5 Acknowledgements

This chapter, in full, is currently being prepared for submission for publication of Nano Energy. Jaeyun Moon, Dylan Lu, Bryan VanSaders, Tae Kyoung Kim, Seong Deok

Kong, Sungho Jin, Renkun Chen and Zhaowei Liu. The dissertation author was the primary researcher and first author of this paper.

3.6 References

1. Lewis, N. S., Toward cost-effective solar energy use. *Science* **2007**, 315, 798-801.

2. Price, H.; Lupfert, E.; Kearney, D.; Zarza, E.; Cohen, G.; Gee, R.; Mahoney, R., Advances in parabolic trough solar power technology. *J Sol Energ-T Asme* **2002**, 124, 109-125.

3. Quaschning, V., Technical and economical system comparison of photovoltaic and concentrating solar thermal power systems depending on annual global irradiation. *Sol Energy* **2004**, 77, 171-178.

4. Gur, I.; Sawyer, K.; Prasher, R., Searching for a Better Thermal Battery. *Science* **2012**, 335, 1454-1455.

5. Denholm, P.; Mehos, M. *Enabling Greater Penetration of Solar Power via the Use of CSP with Thermal Energy Storage*; National Renewable Energy Laboratory: **2011**.

6. Wang, U. The Rise of Concentrating Solar Thermal Power *Renewable Energy World .com* [Online], **2011** June. http://www.renewableenergyworld.com/rea/news/article/2011/06/the-rise-of-concentrating-solar-thermal-power.

7. Chu, S.; Majumdar, A., Opportunities and challenges for a sustainable energy future. *Nature* **2012**, 488, 294-303.

8. Duffie, J. A.; Beckman, W. A., *Solar engineering of thermal processes*. 2nd ed.; Wiley: New York, **1991**; p xxiii, 919 p.

9. Orel, Z. C.; Orel, B.; Gunde, M. K., Spectrally Selective SnO2-F Film on Glass and Black Enameled Steel Substrates - Spray Pyrolytical Deposition and Optical-Properties. *Sol Energ Mat Sol C* **1992**, 26, 105-116.

10. Donnadieu, A.; Seraphin, B. O., Optical Performance of Absorber-Reflector Combinations for Photothermal Solar-Energy Conversion. *J Opt Soc Am* **1978**, 68, 292-297.

11. Allred, D. D.; Jacobson, M. R.; Chain, E. E., Spectrally Selective Surfaces by Chemical Vapor-Deposition. *Sol Energ Mater* **1985**, 12, 87-129.

12. Seraphin, B. O., Chemical Vapor-Deposition of Spectrally Selective Surfaces for High-Temperature Photothermal Conversion. *Thin Solid Films* **1979**, 57, 293-297.

13. Thornton, J. A.; Lamb, J. L., Thermal-Stability Studies of Sputter-Deposited Multilayer Selective Absorber Coatings. *Thin Solid Films* **1982**, 96, 175-183.

14. Thomas, L. K.; Chain, E. E., Spectrally Selective Black Tungsten Films. *Thin Solid Films* **1983**, 105, 203-211.

15. Lira-Cantu, M.; Sabio, A. M.; Brustenga, A.; Gomez-Romero, P., Electrochemical deposition of black nickel solar absorber coatings on stainless steel AISI316L for thermal solar cells. *Sol Energ Mat Sol C* **2005**, 87, 685-694.

16. Patel, S. N.; Inal, O. T.; Singh, A. J.; Scherer, A., Optimization and Thermal-Degradation Study of Black Nickel Solar Collector Coatings. *Sol Energ Mater* **1985**, 11, 381-399.

17. Andersson, A.; Hunderi, O.; Granqvist, C. G., Nickel Pigmented Anodic Aluminum-Oxide for Selective Absorption of Solar-Energy. *J Appl Phys* **1980**, 51, 754-764.

18. Teixeira, V.; Sousa, E.; Costa, M. F.; Nunes, C.; Rosa, L.; Carvalho, M. J.; Collares-Pereira, M.; Roman, E.; Gago, J., Spectrally selective composite coatings of Cr-Cr_2O_3 and Mo-Al_2O_3 for solar energy applications. *Thin Solid Films* **2001**, 392, 320-326.

19. Kennedy, C. E.; Price, H. In *Progress in development of high-temperature solar-selective coating* Proceedings of International Solar Energy Conference, Orlando, Florida USA, Orlando, Florida USA, **2005**.

20. Randich, E.; Allred, D. D., Chemically Vapor-Deposited ZrB_2 as a Selective Solar-Absorber. *Thin Solid Films* **1981**, 83, 393-398.

21. Kennedy, C. E. *Review of Mid- to High-Temperature Solar Selective Absorber Materials.*; National Renewable Energy Laboratory: **2002**.

22. Toor, F.; Page, M. R.; Branz, H. M.; Yuan, H.-C. In *17.1%-Efficient Multi-Scale-Textured Black Silicon Solar Cells without Dielectric Antireflection Coating*, 37th IEEE Photovoltaic Specialists Conference, Seattle, Washington, Seattle, Washington, **2011**.

23. Cai, W.; Genov, D. A.; Shalaev, V. M., Superlens based on metal-dielectric composites. *Phys. Rev. B* **2005**, 72, 193101.

24. Sancho-Parramon, J.; Janicki, V.; Zorc, H., On the dielectric function tuning of random metal-dielectric nanocomposites for metamaterial applications. *Opt. Express* **2010**, 18, 26915.

25. Lu, D.; Kan, J.; Fullerton, E. E.; Liu, Z., Tunable surface plasmon polaritons in Ag composite films by adding dielectrics or semiconductors. *Appl. Phys. Lett.* **2011**, 98, 243114.

26. Yeh, P., *Optical waves in layered media*. Wiley: Hoboken, NJ, **2005**.

27. Eugenio, S.; Rangel, C. M.; Vilar, R.; do Rego, A. M. B., Electrodeposition of black chromium spectrally selective coatings from a Cr(III)-ionic liquid solution. *Thin Solid Films* **2011**, 519, 1845-1850.

28. Aspnes, D. E.; Studna, A. A., Dielectric functions and optical parameters of Si, Ge, GaP, GaAs, GaSb, InP, InAs, and InSb from 1.5 to 6.0 eV. *Phys Rev B* **1983**, 27, 985.

29. Weber, M. J., *Handbook of Optical Materials*. CRC Press: **2003**.

30. Braunstein, R.; Moore, A. R.; Herman, F., Intrinsic Optical Absorption in Germanium-Silicon Alloys. *Phys Rev* **1958**, 109, 695-710.

31. Berkowitz, A. E.; Walter, J. L., Spark erosion: A method for producing rapidly quenched fine powders. *Journal of Materials Research* **1987**, 2, 12.

32. Nguyen, P.-K.; Lee, K. H.; Moon, J.; Kim, S. I.; Ahn, K.; Chen, L.-H.; Lee, S. M.; Chen, R.; Jin, S.; Berkowitz, A., Spark Erosion – a high production rate method for producing Bi0.5Sb1.5Te3 nanoparticles with enhanced thermoelectric performance. *Nanotechnology* **2012**, 23, 415604.

33. Gerion, D.; Zaitseva, N.; Saw, C.; Casula, M. F.; Fakra, S.; Van Buuren, T.; Galli, G., Solution synthesis of germanium nanocrystals: Success and open challenges. *Nano Lett* **2004**, 4, 597-602.

34. Joshi, G.; Lee, H.; Lan, Y. C.; Wang, X. W.; Zhu, G. H.; Wang, D. Z.; Gould, R. W.; Cuff, D. C.; Tang, M. Y.; Dresselhaus, M. S.; Chen, G.; Ren, Z. F., Enhanced Thermoelectric Figure-of-Merit in Nanostructured p-type Silicon Germanium Bulk Alloys. *Nano Lett* **2008**, 8, 4670-4674.

35. Ho, C. K.; Mahoney, A. R.; Ambrosini, A.; Bencomo, M.; Hall, A.; Lambert, T. N., Characterization of Pyromark 2500 Paint for High-Temperature Solar Receivers. *Journal of Solar Energy Engineering* **2014**, 136.

36. Parker, A. R.; Hegedus, Z.; Watts, R. A., Solar-absorber antireflector on the eye of an Eocene fly (45 Ma). *P Roy Soc Lond B Bio* **1998**, 265, 811-815.

37. Parker, A. R.; Townley, H. E., Biomimetics of photonic nanostructures. *Nat Nanotechnol* **2007**, 2, 347-353.

38. Cox, C. R.; Winkler, M. T.; Pijpers, J. J. H.; Buonassisi, T.; Nocera, D. G., Interfaces between water splitting catalysts and buried silicon junctions. *Energy & Environmental Science* **2013**, 6, 532-538.

39. Pijpers, J. J. H.; Winkler, M. T.; Surendranath, Y.; Buonassisi, T.; Nocera, D. G., Light-induced water oxidation at silicon electrodes functionalized with a cobalt oxygen-evolving catalyst. *Proceedings of the National Academy of Sciences* **2011**, 108, 10056-10061.

40. Sun, K.; Shen, S.; Cheung, J. S.; Pang, X.; Park, N.; Zhou, J.; Hu, Y.; Sun, Z.; Noh, S. Y.; Riley, C. T.; Yu, P. K. L.; Jin, S.; Wang, D., Si photoanode protected by a metal modified ITO layer with ultrathin NiOx for solar water oxidation. *Physical Chemistry Chemical Physics* **2014**, 16, 4612-4625.

CHAPTER 4 : Black Oxide Nanoparticles as Durable Solar Absorbing Material for High-Temperature Concentrating Solar Power System

4.1 Introduction

The development and deployment of renewable energy sources is becoming an increasingly urgent need for human society[1, 2]. Concentrating solar power (CSP) systems (or solar thermal systems) are becoming an important part of the major portfolio of renewable energy generation. One of the key potential advantages of CSP over many other forms of the renewables is the possibility of inexpensive energy storage, for example, as a part of thermal energy storage systems (TES), which are useful for control of energy distribution in the grid system. The TES can extend the electricity generation capability to periods with no sunlight available, thereby significantly expanding the value and usage of solar energy[3]. CSP systems have also been considered for possible combination with other alternative energy systems, such as solar photovoltaic generation or thermoelectric generation, to increase penetration of renewable energy power[4, 5]. Despite the perceived benefits, the levelized cost of energy (LCOE) of CSP is still too high to compete with traditional thermal power plants and some other alternative energy technologies (such as photovoltaics).

In order to develop a cost-competitive CSP technology, it is imperative to increase the system power conversion efficiency. To maximize the efficiency of CSP, it is desirable to raise the operating temperature for higher Carnot efficiency. As a result, the temperature of heat transfer fluids (HTFs) needs to be 700^{o}C or higher[6]. Toward this aim, all of the components of CSP systems, such as solar field, HTFs, power block, TESs, and solar receivers need to be made compatible with the higher-temperature operation.

As far as the solar receiver is concerned, the light-absorbing coatings on the receiver play an important role by absorbing solar thermal energy and raising the temperature of the HTFs to above 700^{o}C. Although spectrally selective coatings (SSCs) with multilayers/graded cermets or tandem structures have been developed and stably operated in vaccum in parabolic trough CSP systems[7-12], none of these SSC structures can operate at high temperatures in air, which is needed in future solar-tower based CSP systems. The state-of-the-art solar absorbing material used in solar towers is based on a commercially available black paint called Pyromark 2500®. Pyromark 2500® is known to have ~0.97 solar absortance and ~0.8 thermal emittance above 600 ^{o}C and has been used for central solar receivers of CSP plants. However, according to the prior studies, the absorptivity degraded after high temperature exposure due to crystal structure changes and phase instability.[13, 14] Therefore it is clear that a new light absorbing coating material having high absorption efficiency, excellent durability at elevated temperature in air environment and scalability is strongly desired for the next generation CSP systems.

Since the light absorption is directly related to solar energy generation efficiency, a large number of studies about optical absorption enhancement have been actively

pursued. Several light trapping approaches were studied, such as a traditional texturing[15, 16] and emergent methods employing photonic[17-19] and plasmonic structures[20, 21]. However, most of studies about light trapping have been applied on photovoltaic applications using vacuum deposition methods. As the result, these processes are not necessarily compatible with CSP applications, where spray coating is generally used to coat the light absorbing layers[14, 22], for example, Pyromark 2500® in Solar One and Solar Two central towers.[23, 24]

Here, we report highly durable and efficient light absorbing coatings for concentrating solar power receivers. The cobalt oxide nanopowders were synthesized via a facile hydrothermal process and utilized as the light-absorbing material in the coating layers. The coating layers consist of cobalt oxide nanopowders dispersed in silica matrix, and are deposited on metal substrates via a simple and scalable spray coating process, which is compatible with CSP applications. We employed novel and yet simple surface texturing techniques, based on sacrificial polymer beads that can be easily integrated with the spray coating process, to improve the light absorption. Finally, the developed coating layer exhibited unprecedented high-temperature durability, showing no degradation in structural or optical properties after annealing at 750^{o}C in air for 1,000 hours.

4.2 Results and Discussion

4.2.1 Cobalt Oxide Nanopowders Synthesis and Coating Process

Cobalt oxide nanoparticles were synthesized by the hydrothermal process. Both the as-synthesized and annealed cobalt oxide nanoparticles were examined with scanning electron microscopy (SEM) as shown in Figure 4.1(a). The diameter of the as-synthesized

powders ranges from 100 to 300 nm after a stabilizing heat treatment. According to X-ray diffraction (XRD) analysis shown in Figure 4.1(b), the synthesized chemical compound is confirmed as Co_3O_4, which is one of the polymorphs of cobalt oxide.[15,16] Pure CoO is difficult to synthesize, because CoO can easily acquire oxygen and convert to a higher level oxide. While Co_2O_3 can be created when the cobalt compounds are annealed at a low temperature, it can easily be converted to Co3O4 when heated above 538K in oxygen-containing environment. [17]

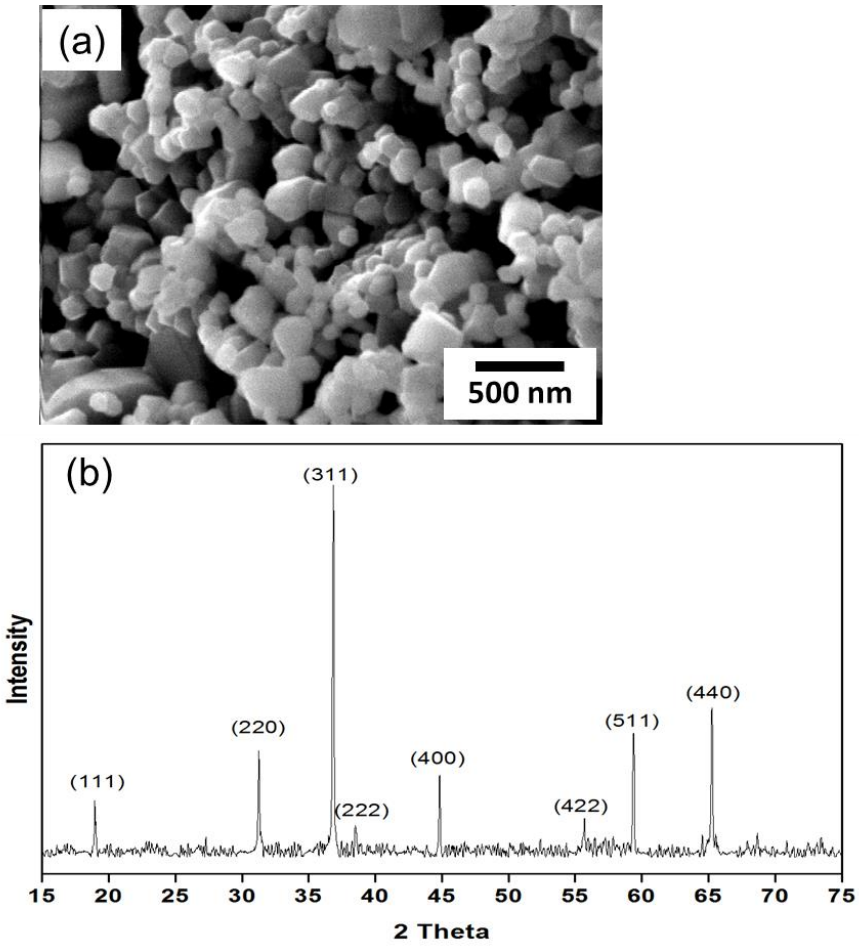

Figure 4.1 Cobalt oxide nanopowders characterization: (a) SEM image of as-synthesized powders and (b) X-ray diffraction pattern of Co oxide powders after stabilizing at 750^{o}C for 2 hours

Therefore, we have concentrated our effort on the most stable form of cobalt oxide, i.e., Co_3O_4. The coating process was carried out using a gravity-feed spray gun. All of the coating layers were deposited onto high-temperature Inconel substrate (type 625) coupons (½" × ½" in area) pre-treated with sand blasting. Inconel was chosen because it is currently used for high-temperature CSP due to its high-temperature durability[25]. The schematic diagram of the coated structure is shown in Figure 4.2(a), and the photographs of an Inconel substrate and a base-layer coated sample are shown in Figure 4.2(b).

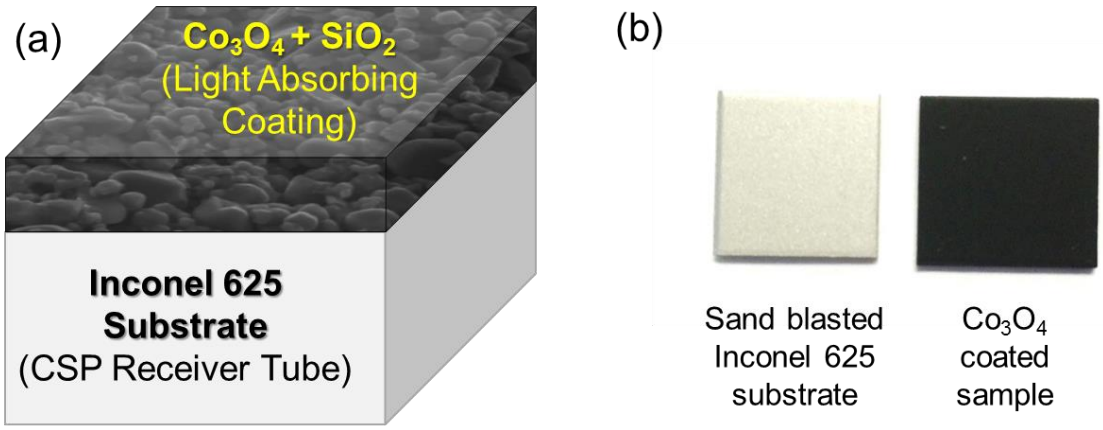

Figure 4.2 (a) Schematic diagram of Co oxide light absorbing coating structure and (b) photographs of a sand blasted Inconel 625 metal substrate and a Co_3O_4 coated sample (designated as Co_3O_4-1 sample).

4.2.2 Light Absorbing Coating Structure Modification

To improve the sunlight absorption efficiency, we first examine the effect of surface morphology on the light absorption performance of the coating. In order to evaluate the solar absorber, the figure of merit (FOM) is defined as Equation 1.

$$F = \frac{\int_0^\infty \big(1 - R(\lambda)\big) I(\lambda) d\lambda - \frac{1}{C}\left[\int_0^\infty (1 - R(\lambda)) B(\lambda, T) d\lambda\right]}{\int_0^\infty I(\lambda) d\lambda} \quad (1)$$

where R(λ) is the spectral reflectivity, I(λ) is the spectral solar radiance per square meter as defined by the reference solar spectral irradiation(ASTM G173), B(λ,T) is the spectral thermal emission of a black body at temperature T, and C is the concentration ratio. In this study, the temperature of the solar receiver is assumed to be 750℃, which is a desired operating temperature to enhance CSP efficiency.

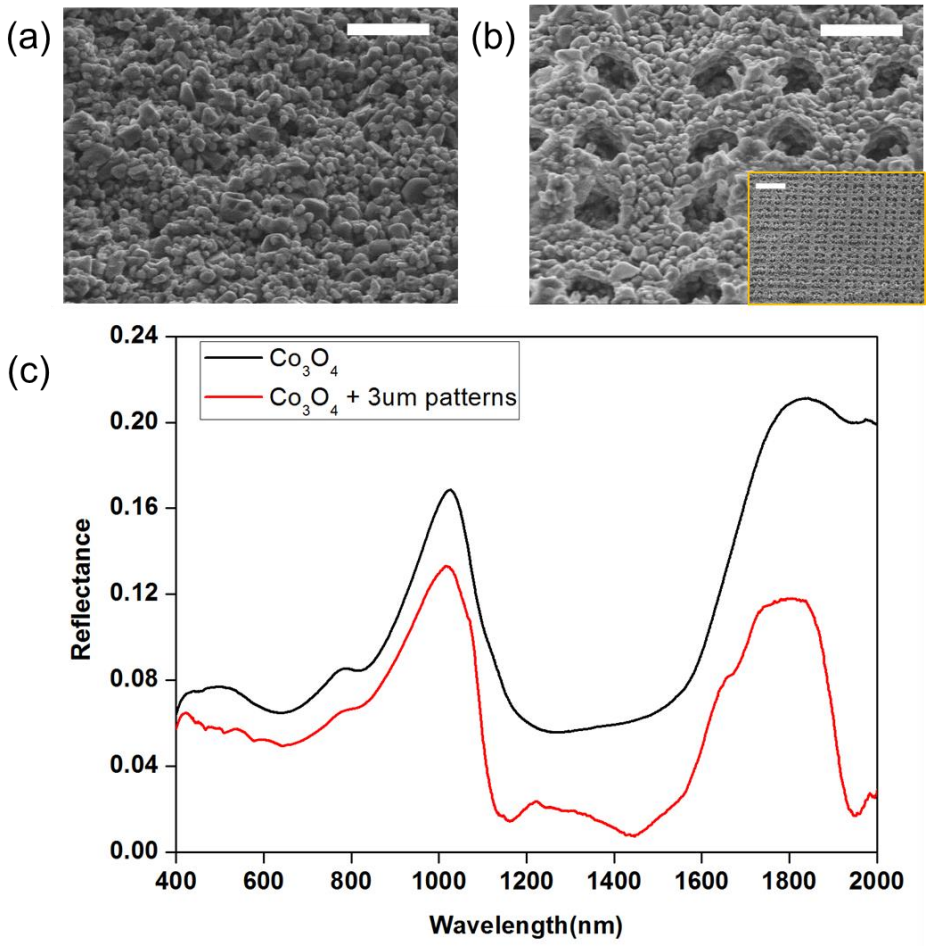

Figure 4.3 SEM images of (a) Co_3O_4 coating (scale bar : 5μm) and (b) Co_3O_4 coating layer with 3μm hole patterns (scale bar : 5μm, inset, 20μm) and the reflectance in visible and NIR range of regular Co_3O_4 SSC and Co_3O_4 with 3μm diameter hole patterns.

Figure 4.3(a) and (b) show SEM images of Co_3O_4 coating layer without and with embedded hole patterns (pores), respectively. The measured specular reflectance of the coating within the spectral range of 400nm to 2μm was shown in Figure 4.3(c) and the FOM was calculated according to Equation 4.1. The FOMs of the non-patterned and patterned coatings are 0.8542 and 0.8730, respectively. The suppressed reflectance due to the patterned sample led to ~2.2% increase in FOM, which is substantial and can be attributed to enhanced light trapping in the patterned holes. The incident light goes into the holes and diffracts at oblique angles within the Co_3O_4 absorbing coating, thus the light absorption is improved. Previously, computational and experimental studies have shown similar optical light-trapping[11,19] phenomena with various surface patterns, mostly with microscale pillars. Even though hole patterns may not be as efficient for scattering light in comparison to dense vertical pillar array structures due to the smaller surface area that an oblique light can reach, the process of making hole patterns is easier to implement with the spray coating process.

Table 4.1 Sample fabrication condition and figure of merits (FOM)

Sample Name	Volume ratio			FOM (Figure of merits)
	Co_3O_4 nanopowders	SiO_2 dielectric matrix	Polystyrene polymer beads	
Co_3O_4-1	1	1.5	0	**0.854**
Co_3O_4-2	1	4.5	3	**0.877**
Co_3O_4-3	1	6.5	5	**0.882**

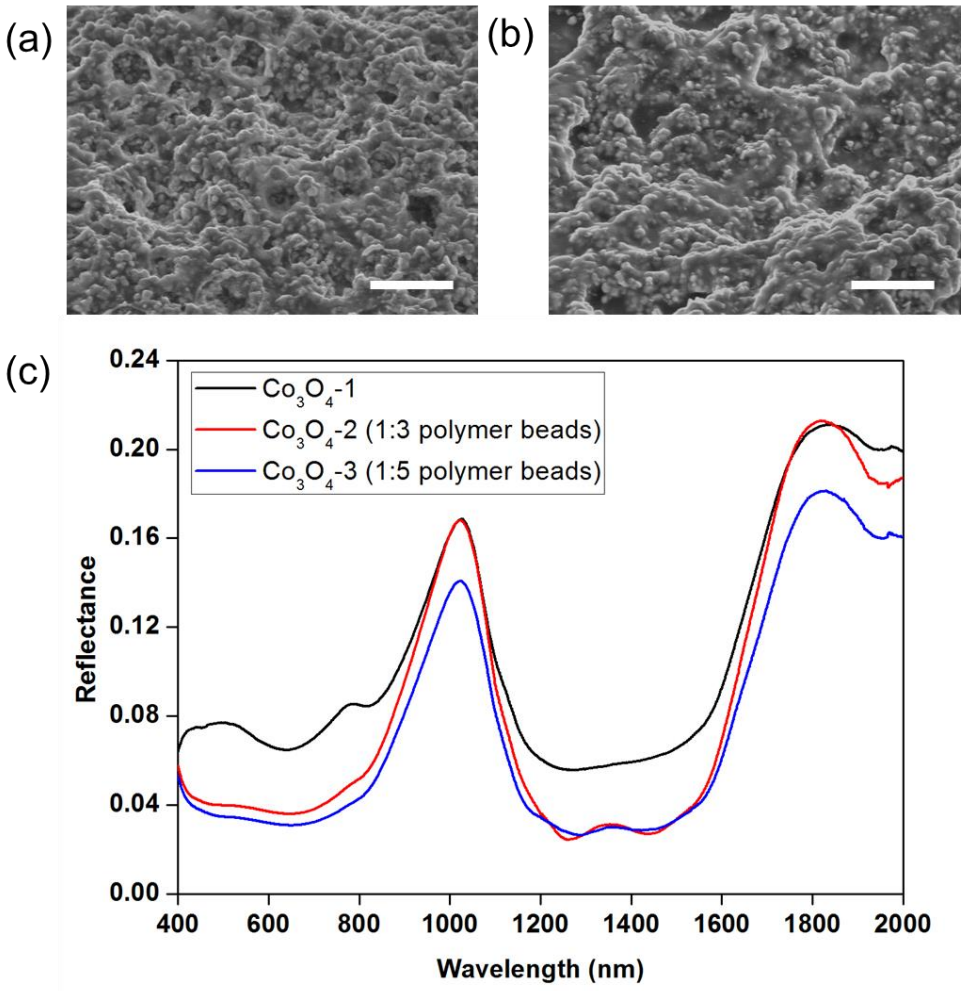

Figure 4.4 SEM images of (a) Co_3O_4-2 (vol. ratio=1(Co_3O_4) :3 (polymer beads), see Table 4.1) coating (scale bar : 5μm) and (b) Co_3O_4-3(vol. ratio =1(Co_3O_4) :5 (polymer beads)) coating layer (scale bar = 5μm) and the reflectance in visible and NIR range of Co_3O_4-1, Co_3O_4-2 and Co_3O_4-3.

After establishing the principle of enhanced light absorption with surface hole patterning, we developed a more scalable process based on sacrificial polymer beads, as described in section 4. The details of the samples are provided in Table 4.1. From the SEM images shown in Figure 4.4(a) and (b), the surface roughness of the coating layer was increased after introducing the polymer beads in Co_3O_4 coating layer, compared to the original coating (Figure 4.3(a)). The increased roughness results in reduced

reflectance (Figure 4.4 (c)) and enhanced FOMs (Table 4.1). The FOM of the Co_3O_4-2 and Co_3O_4-3 samples are increased by 2.7% and 3.3%, respectively, compared to the initial Co_3O_4 sample. The roughened surfaces can be regarded as being close to Lambertian surface, which is defined as a surface reflecting light with equal intensity in all directions, namely diffusely reflecting surface. Similar mechanism has been utilized for enhanced absorption in solar cells, for example, by creating 'black Si' using anisotropic etching of surface[15], hydrogen etching[26], or mechanical grinding[16, 27]. Furthermore, random roughness helps scatter light more efficiently than periodic structure due to a break in mirror symmetries (i.e. suppressed diffractive effects), as the prior simulation studies demonstrated the random or skewed pyramid structures outperformed regular pyramidal texturing.[15, 28] Compared to these reported processes (etching or mechanical grinding), our process of using sacrificial polymer beads can be easily integrated with the spray coating process without any additional micromachining steps, with the polymer particles automatically burned away to create pores during the subsequent heating to the CSP operating temperature. Therefore, the process developed here is cost-effective and scalable to meet the needs of CSP applications.

4.2.3 High Temperature Stability of Co_3O_4 Light Absorbing Coating

The receiver coating in the next generation CSP systems should possess not only high thermal efficiency but also high temperature stability because of the anticipated trend of higher operating temperature (above 700 - 750^{o}C)[29, 30]. The high-temperature stability of the coating depends on both the intrinsic material properties (e.g., phase transformation at high temperature) and structural integrity of the porous coating, as well

as its adhesion to the substrate. We carried out the high-temperature annealing test in air as described in Section 4 for both the coating sample and the nanopowders. For the coated sample, the one with 1:5 volume ratio of cobalt oxide powders to polymer beads (Co_3O_4-3) was used because it showed the best FOM in this study.

The microstructural and XRD analysis results are displayed in Figure 4.5. Figure 5(a) and (b) show the SEM images of the nanoparticles after the 750^{o}C annealing test. The images indicate that the surface roughness was not changed and the nanopowders were not agglomerated upon annealing, demonstrating the structural stability of the material. Figure 4.5(c) shows the XRD results of the sample before vs after annealing. The XRD diffraction peaks for all the samples (as-prepared, 10 hr aged, and 100 hr aged samples) indicate that the samples consist of identical single phase Co_3O_4. These results clearly show that the cobalt oxide nanopowders synthesized by the hydrothermal process in this study were stable at the set temperature of 750^{o}C. Cobalt usually forms two oxide structures, namely, CoO with NaCl crystal structure and Co_3O_4 with spinel structures.[31] According to the thermodynamic diagram of the Co-O system, Co_3O_4 was a stable phase at 750^{o}C in ambient atmosphere (0.21atm O_2 partial pressure).[32] In this environment, Co_3O_4 is stable from room temperature up to 840^{o}C and converts to CoO above 840 ^{o}C.

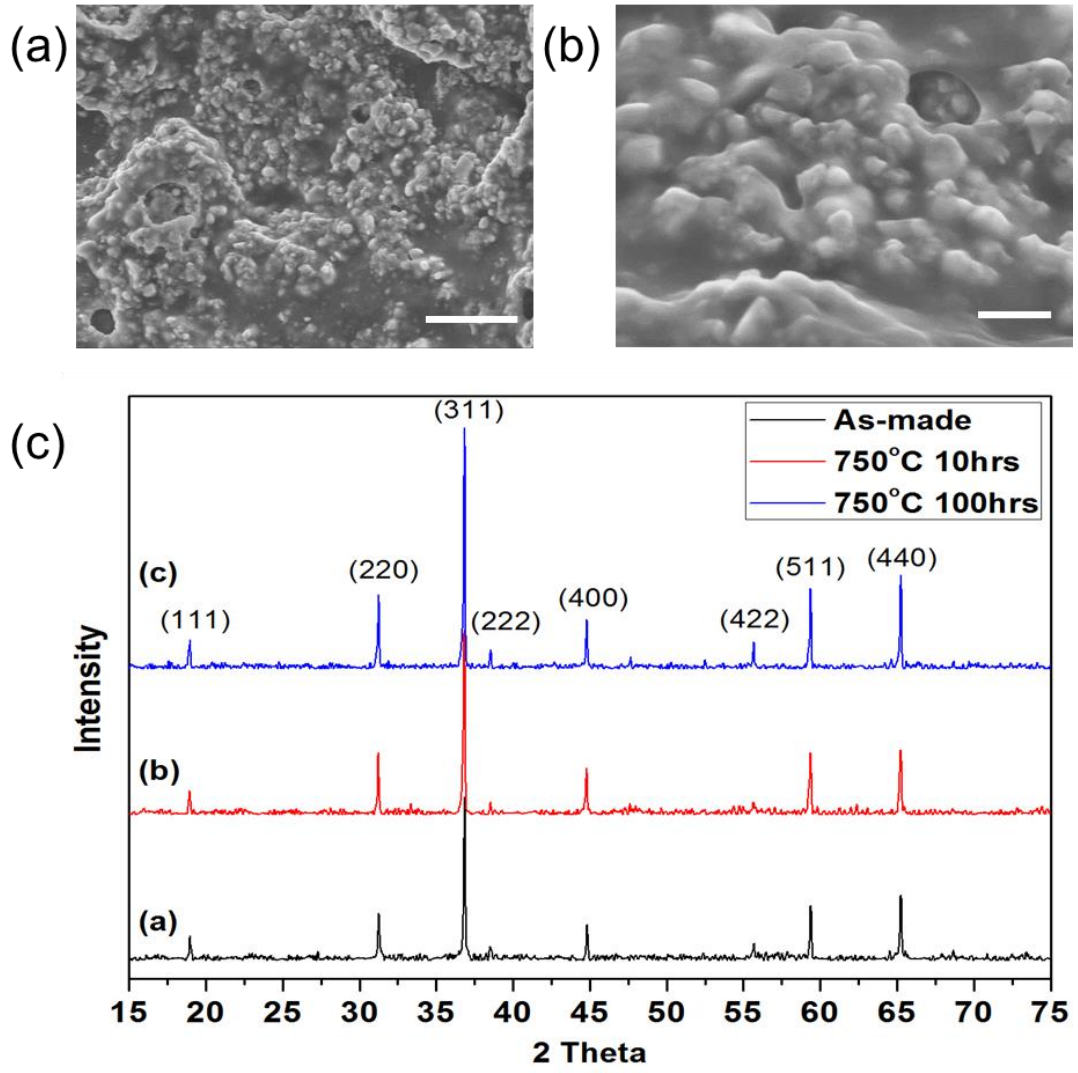

Figure 4.5 (a) (b) SEM image of Co_3O_4 coating after annealing at 750°C 1000 hours (scale bar: (a)5um and (b)1um) and (c) XRD diffraction patterns of Co oxides, as-made (black), after 750°C exposure for 10hrs (red) and 100hrs (blue)

Finally, we show the FOMs of the best-performing samples with 1:5 volume ratio of black oxide powders to polymer beads (designated as Co_3O_4-3A and Co_3O_4-3B samples) after various annealing durations ranging from 0 to 1,000 hours in Figure 4.6. The result clearly demonstrates that the FOM remains the same after 1,000 hours of high temperature exposure, indicating that the main features of the high optical performance,

including cobalt oxide phase composition, surface roughness and porous structure were still intact after extended annealing. Therefore, Co_3O_4 black oxide is a promising solar absorption candidate material for 750°C CSP operating environment. In contrast, Pyromark coating, which is the state of the art coating for CSP applications, shows ~3% degradation of solar absorptance at 750°C after 300 hours[14].

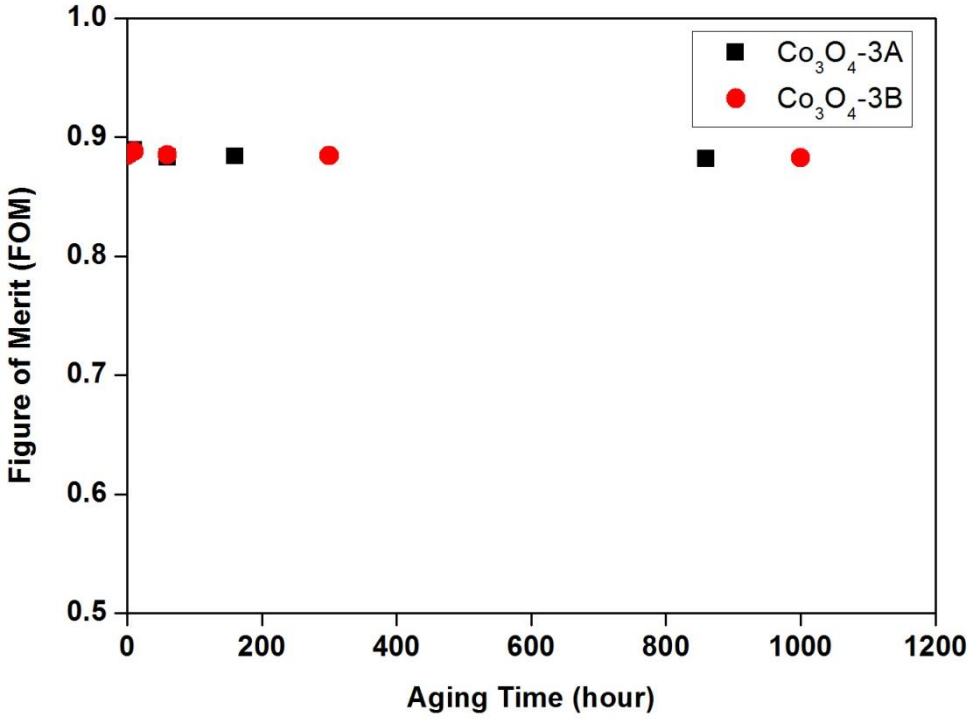

Figure 4.6 Figure of merits (FOMs) of two samples of Co_3O_4-3 condition (in Table 4.1) as a function of exposure time at 750°C

4.3 Conclusion

In summary, we have synthesized nanoscale Co_3O_4 black oxide using a hydrothermal process and developed novel designs and fabrication of light-absorbing coating structure for highly efficient CSP receiver. By introducing sacrificial polymer fillers into the nanopowder-based coating slurry, the surface texturing was successfully obtained and the optical performance was improved by over 3%, reaching a high thermal absorption figure of merit of 88.2%. For high temperature stability, a long-term aging test was performed and the results revealed that the light-trapping structure remained intact after 750oC exposure in air for 1,000 hours. Consequently, the FOM showed negligible decrease after 750oC exposure. Based on these results, Co_3O_4 textured coating is a promising candidate as a solar absorbing layer for future high-temperature CSP systems. The Co_3O_4 layer can easily be spray-coated in a manner suitable for large-scale CSP receiver applications as well as for on-site repairability if needed.

4.4 Experimental Section

4.4.1 Cobalt oxide nanopowders synthesis and sample preparation

Cobalt oxide nanoparticles were synthesized via hydrothermal process using cobalt chloride salt ($CoCl_2 \cdot 6H_2O$) as the precursor. 10 M solution of sodium hydroxide (NaOH) was gradually dropped into 1 M solution of cobalt chloride to induce precipitation of cobalt hydroxide until pH value of the reacted solution reached 11. The hydrothermal synthesis was performed at 150^oC for 20 hours in order to transform the precipitated cobalt hydroxide into cobalt oxide. The cobalt oxide particles were then

washed with de-ionized water using a centrifuge and dried using a freeze-dryer. The as-synthesized nanoparticles were annealed at 750^{o}C for 2 hours for phase stabilization. For the fabrication of Co_3O_4 slurry, methyl phenyl polysiloxane resin (SILIKOPHEN® P 80/X) was utilized as precursor of SiO_2 matrix. The volume ratio between the active material (cobalt oxide nanopowders) and the SiO_2 matrix was systematically varied and optimized. The required amount of resin was diluted with an organic solvent mixture consisting of two miscible solvents, xylene and isobutanol (volume ratio 3:1). The optimum dilution was important to ensure good quality of the coating layers, because too viscous slurry could not make a smooth spray stream while very dilute slurry could not make a stable spray-coating onto substrates. In order to dissolve the resin in the solvent, the mixture was sonicated for 30 minutes with a probe type sonicator. During sonication, the solution container was cooled in an ice-bath to avoid concentration change due to the evaporation of organic solvents. Co_3O_4 powders were mixed with the prepared solution and yttria stabilized zirconia (YSZ) grinding balls were also added into the blend. The ball milling was conducted for 24 hours in order to make the mixture homogeneous.

The black oxide spray coating was performed using a spray gun on a high temperature Ni alloy (Inconel 625) sheet coupons (½" × ½" in size). The spray pressure was set at 40 psi and the distance between the spray gun and the Inconel substrate is about 10 cm, which has been optimized for the best coating quality. After spray coating, the samples were heated at 250^{o}C for 1 hour for curing of SiO_2 resin. All of the coating samples consist of two layers: the base layer of approximately 30 μm thick and a top layer with surface-topography-modified structure described in the next paragraph.

4.4.2 Coating surface texturing

The first method to alter the surface texturing and topography of the top layer to improve optical absorption was to employ imprinting stamps with SU-8 polymer pillars which were prepared by using standard microfabrication processes. The polymer pillars were 3µm in both diameter and spacing and 10µm in height. The stamps were then applied on coated Co_3O_4 coating surface and left as imprinted prior to the resin curing step. Then, the sample was annealed at 750^oC for 1 hour to burn away and remove the remaining polymer pillars.

The second method employed to create roughened surface is by incorporating into and subsequently removing micron-sized sacrificial polymeric beads out of the Co_3O_4 coating layer. The volumetric concentration of Co_3O_4, polymer beads and silicone resin was optimized to get the best optical performance (as shown in Table 4.1), and the mixtures were again sonicated with a probe type sonicator for proper mixing. Then, a desired amount of silicone resin was added, followed by the same ball milling and spray coating processes described in the prior paragraphs. Finally, the coated layers were annealed at 750^oC for 1 hour to remove the polymeric beads and leave behind the porous and topographically rough top surface of Co_3O_4 layer.

4.4.3 Optical performance evaluation and High Temperature Aging Tests in Air

The thermal efficiency of a solar receiver, which measures the ratio of the energy absorbed relative to the incident solar energy, and FOMs can be calculated from Equation 1. All integrals to calculate FOMs are evaluated in the range from 300nm to 20µm, as only negligible quantities of solar power are present outside this range. Reflection data

were measured using a Labsphere® 4" integration sphere to collect all angles of reflection from samples and Andor® 303i spectrometer equipped with a Si based (spectral range 300-1100nm) and InGaAs based (spectral range 900nm-2500nm) detector. Reflection behavior of samples outside of the range 400nm- 2.5um was extrapolated for use in Equation 4.1.

To characterize the durability of the coating at elevated temperature, the long-time annealing tests at 750oC in air were carried out on the coated samples as well as the Co_3O_4 nanopowders with the annealing time up to 1,000 hours. The composition of the material before vs after the annealing was analyzed using XRD (Bruker D8 Discover) using a scan speed of $0.037^o s^{-1}$ in the 2θ range of $15\sim75^o$; the structural integrity was examined using optical microscope and SEM (Phillips XL30 FEG); and finally the optical properties of the samples were measured with the same procedure as above.

4.5 Acknowledgements

This chapter, in full, is currently being prepared for submission for publication of Advanced Energy Materials. Jaeyun Moon*, Tae Kyoung Kim*, Bryan VanSader*, Chulmin Choi, Zhaowei Liu, Sungho Jin, and Renkun Chen. The dissertation author was the primary researcher and first author of this paper.

4.6 References

1. Hoffert, M. I.; Caldeira, K.; Jain, A. K.; Haites, E. F.; Harvey, L. D. D.; Potter, S. D.; Schlesinger, M. E.; Schneider, S. H.; Watts, R. G.; Wigley, T. M. L.; Wuebbles, D. J. *Nature* **1998,** 395, (6705), 881-884.

2. U. S. Energy Information Administration, *United States Energy Information Administration (EIA), International Energy Outlook 2013*; **2013**.

3. Morisson, V.; Rady, M.; Palomo, E.; Arquis, E. *Chem Eng Process* **2008,** 47, (3), 499-507.

4. Denholm, P.; Mehos, M. *Enabling Greater Penetration of Solar Power via the Use of CSP with Thermal Energy Storage*; National Renewable Energy Laboratory: **2011**.

5. Wan, P. D. Y.-H.; Hummon, M.; Mehos, M. *An Analysis of Concentrating Solar Power with Thermal Energy Storage in a California 33% Renewable Scenario*; National Renewable Energy Laboratory: **2013**.

6. Kolb, G. J.; Ho, C. K.; Mancini, T. R.; Gary, J. A. *Power Tower Technology Roadmap and Cost Reduction Plan*; DE-AC04-94AL85000.; Sandia National Laboratories: **2011**.

7. Selvakumar, N.; Barshilia, H. C. *Sol Energ Mat Sol C* **2012,** 98, 1-23.

8. Barshilia, H. C.; Kumar, P.; Rajam, K. S.; Biswas, A. *Sol Energ Mat Sol C* **2011,** 95, (7), 1707-1715.

9. Cao, F.; McEnaney, K.; Chen, G.; Ren, Z. F. *Energ Environ Sci* **2014,** 7, (5), 1615-1627.

10. Cespedes, E.; Wirz, M.; Sanchez-Garcia, J. A.; Alvarez-Fraga, L.; Escobar-Galindo, R.; Prieto, C. *Sol Energ Mat Sol C* **2014,** 122, 217-225.

11. Barshilia, H. C.; Selvakumar, N.; Rajam, K. S.; Biswas, A. *J Appl Phys* **2008,** 103, (2), 023507.

12. Barshilia, H. C.; Selvakumar, N.; Rajam, K. S.; Rao, D. V. S.; Muraleedharan, K.; Biswas, A. *Appl Phys Lett* **2006,** 89, (19), 191909.

13. Ho, C. K.; Mahoney, A. R.; Ambrosini, A.; Bencomo, M.; Hall, A.; Lambert, T. N. In *Characterizatio of Pyromark 2500 for High-Temperature Solar Receivers*, ASME 2012 6th International Conference on Energy Sustainability & 10th Fuel

Cell Science, Engineering and Technology Conference ESFuelCell2012, San Diego, **2012**; San Diego.

14. Ho, C. K.; Mahoney, A. R.; Ambrosini, A.; Bencomo, M.; Hall, A.; Lambert, T. N. *J Sol Energ-T Asme* **2014,** 136, (1), 14502.

15. Campbell, P.; Green, M. A. *J Appl Phys* **1987,** 62, (1), 243-249.

16. Bender, H.; Szlufcik, J.; Nussbaumer, H.; Palmers, G.; Evrard, O.; Nijs, J.; Mertens, R.; Bucher, E.; Willeke, G. *Appl Phys Lett* **1993,** 62, (23), 2941-2942.

17. Bozzola, A.; Liscidini, M.; Andreani, L. C. *Opt Express* **2012,** 20, (6), A224-A244.

18. Zhou, D. Y.; Biswas, R. *J Appl Phys* **2008,** 103, (9), 093102.

19. Mallick, S. B.; Agrawal, M.; Peumans, P. *Opt Express* **2010,** 18, (6), 5691-5706.

20. Ferry, V. E.; Verschuuren, M. A.; Li, H. B. T.; Verhagen, E.; Walters, R. J.; Schropp, R. E. I.; Atwater, H. A.; Polman, A. *Opt Express* **2010,** 18, (13), A237-A245.

21. Atwater, H. A.; Polman, A. *Nat Mater* **2010,** 9, (3), 205-213.

22. Lampert, C. M. *Sol Energ Mater* **1979,** 2, (1), 1-17.

23. Ho, C. K.; Pacheco, J. E. *Levelized Cost of Coating (LCOC) for Selective Absorber Materials* Sandia National Laboratories: **2013**.

24. Bradshaw, R. W.; Dawson, D. B.; Rosa, W. D. l.; Gilbert, R.; Goods, S. H.; Hale, M. J.; Jacobs, P.; Jones, S. A.; Kolb, G. J.; Pacheco, J. E.; Prairie, M. R.; Reilly, H. E.; Showalter, S. K.; Vant-Hull, L. L. *Final Test and Evaluation Results from the Solar Two Project*; Sandia National Laboratories: **2002**.

25. Lata, J. M.; Rodriguez, M.; de Lara, M. A. *J Sol Energ-T Asme* **2008,** 130, (2), 021002.

26. Ha, J. M.; Yoo, S. H.; Cho, J. H.; Cho, Y. H.; Cho, S. O. *Nanoscale Research Letters* **2014,** 9, 9.

27. Willeke, G.; Nussbaumer, H.; Bender, H.; Bucher, E. *Sol Energ Mat Sol C* **1992,** 26, (4), 345-356.

28. Han, S. E.; Chen, G. *Nano Lett* **2010,** 10, (11), 4692-4696.

29. Chu, S.; Majumdar, A. *Nature* **2012,** 488, (7411), 294-303.

30. Ho, C. K.; Iverson, B. D. *Renew Sust Energ Rev* **2014,** 29, 835-846.

31. Birks, N.; Meier, G. H.; Pettit, F. S., *Introduction to the High Temperature Oxidation of Metals*. 2nd ed.; Cambridge University Press: **2006**.

32. Chen, M.; Hallstedt, B.; Gauckler, L. J. *J Phase Equilib* **2003,** 24, (3), 212-227.

CHAPTER 5 : Conclusions and Future Works

5.1 Summary

Thermal energy conversion technologies have been attractive ways to generate clean and reliable energy. Regardless of the advantages of thermoelectrics and concentrating solar powers, a higher efficiency and a lower cost still need to be satisfactory. In this thesis, the approaches to improve the efficiency and reduce the cost of the thermal energy conversion technologies have been suggested and experimentally demonstrated remarkable results.

First, gate modulated thermopower measurements on intrinsic Ge/Si core-shell nanowires have been carried out. The Fermi level pinning induced by surface states of Si shell causes the accumulation of hole gas within the intrinsic Ge core nanowire and the gate voltage controls the carrier concentration. The gate modulated Ge-Si core-shell nanowires provide an efficient and useful solution to demonstrate the relationship between the thermopower and electrical transport properties, such as carrier concentration and mobility. The carrier mobility of the nanowires depending on temperatures were compared to bulk Ge and it reveals that the less ionized impurity scattering and surface passivation could lead the higher carrier mobility. The relationship between the Seebeck coefficient and the hole concentration of the various Ge-Si core/shell nanowire samples was investigated and showed to follow the behavior of bulk Ge. This result could also mean that the quantum confinement effect is not valid within 11-25nm core diameters at room temperature. It is also worth mentioning that the gate-

voltage modulation with Ge-Si core/shell nanowires can be utilized to examine and optimize the power factor and electrical properties for the development of advanced thermoelectric materials.

Second, the new scheme of a spectrally selective coating (SSC) structure of a fractal structure of semiconductor nanopowders was reported. The optimum band-gap semiconductor materials could absorb sunlight in the desired wavelength range, because the semiconductor material absorbs the short wavelength radiation which has higher photon energy than the band gap of the semiconductor while it can be reflective for long-wavelength radiation due to lower photon energy. The $Si_{0.8}Ge_{0.2}$ alloy nanopowders were synthesized using a spark erosion process and the SSC sample of $Si_{0.8}Ge_{0.2}$ was prepared via a drop casting method. The excellent light absorptivity (~90~95%) in visible range and relatively low IR emissivity (<30%) of the SSC showed potential for CSP solar receiver applications. The multi-scale structure consisting of the semiconductor powders in a wide range of particle size (10 nm–10 μm) significantly improved the solar absorptivity in comparison to the SSC fabricated with mono-dispersed nanoparticles because of the efficient light trapping. The development of the high solar absorptance and low IR emittance is considerably necessary for the next generation CSP technologies to increase the CSP efficiency.

Lastly, the black oxide, Co_3O_4, nanopowders were synthesized via a hydrothermal process and the efficient and durable light absorbing coating for high temperature CSP was developed using the Co_3O_4 nanopowders. In order to create surface texturing on the coating surface, sacrificial polymer stamps and beads were introduced into the black oxide nanopowder-based coating slurry. The rough surface was successfully attained and

the optical performance was enhanced by over 3%, achieving a high thermal figure of merit of 0.882, according to the definition of the figure of merit in this study. Furthermore, the high temperature stability results evaluated by a long-term aging process (1000 hours) showed that the phase composition of Co_3O_4 layer was not changed after 100 hours annealing process and the surface texturing was also still undamaged after a high temperature exposure (750^oC) in air environment for 1000 hours. As a result, the figure of merit demonstrated negligible reduction after a long-term annealing (at 750^oC in air for 1000 hours). Thus, Co_3O_4 coating with a surface modification can be a promising candidate as the light absorbing coating for future high-temperature CSP systems. Furthermore, the spray coating process used in this study can be easily applicable for large-scale CSP receivers and provides on-site repairability as well.

5.2 Future work

There are several potential approaches to deeply understand phenomena or to enhance the efficiency and scalability of thermoelectrics and concentrating solar power systems, which are discussed in detail below.

As presented in CHAPTER 2, the thermopower of Ge-Si core shell nanowires showed same behavior as bulk Ge with 11~20nm core diameter, which means that a quantum confinement effect was not valid within this range. According to prior studies[1], the quantum confinement could cause a dramatic change of the density of state, thereby leading a significant improvement of the power factor of thermoelectrics materials. Since a gate modulated intrinsic Ge-Si core/shell nanowires provide a powerful and convenient

platform to examine the thermoelectric properties, especially, the thermopower and electrical transport properties, the smaller intrinsic Ge-Si core/shell nanowires (<<10nm) will be a very attractive material system for further studies of a quantum effect on thermoelectric performance.

With regard to scalability and cost reduction of thermoelectrics, there is a rising interest on printable thermoelectrics. The conductive polymers such as PEDOT:PSS, have been successfully developed[2, 3], and the organic-inorganic thermoelectrics materials also have been investigated[4, 5]. However, the thermoelectric performance of the printable thermoelectrics ink and the hybrid composite is still not good as an inorganic thermoelectric material. The performance can be improved by selecting and designing optimum organic and inorganic materials because the composite material system provides design flexibility.

In CHAPTER 3 and 4, the efficient light absorbing coatings for future CSP systems were proposed and experimentally demonstrated. Recently, the volumetric receiver appears to be a best alternative to traditional metal tube receivers[6]. The volumetric receivers absorb the solar radiation via porous absorbing materials transferring absorbed heat energy to a gas steam passing through the porous structure. The light absorbing material with nano-sized pores can efficiently trap light and increase the output temperature of a fluid. Since a structure modification using sacrificial polymer beads was developed in this study, further optimization will allow the nanoporous light absorbing coatings to be utilized for next generation volumetric CSP receivers with high operating temperature, thus leading a better efficiency.

Furthermore, the deep understanding of thermal behaviors on energy materials will be significantly useful. A couple of examples are introduced. High thermal insulation coatings are necessary to increase the engine efficiency. [7, 8] The other example is that materials for phase change storage have to possess a large latent heat and high thermal conductivity. However, it could be challenging to find the materials satisfying all requirements. In case of paraffin, it is cost-efficient and has a suitable thermal energy storage capacity, but thermal conductivity needs to increase[9]. Examination of thermal phenomena of materials will improve the thermal storage material properties and help to develop the efficient thermal energy storage system.

5.3 References

1. Hicks, L. D.; Dresselhaus, M. S. *Phys Rev B* **1993,** 47, (19), 12727-12731.

2. Bubnova, O.; Khan, Z. U.; Malti, A.; Braun, S.; Fahlman, M.; Berggren, M.; Crispin, X. *Nat Mater* **2011,** 10, (6), 429-433.

3. Kim, G. H.; Shao, L.; Zhang, K.; Pipe, K. P. *Nat Mater* **2013,** 12, (8), 719-723.

4. Madan, D.; Wang, Z. Q.; Chen, A.; Juang, R. C.; Keist, J.; Wright, P. K.; Evans, J. W. *Acs Appl Mater Inter* **2012,** 4, (11), 6117-6124.

5. Zhang, B.; Sun, J.; Katz, H. E.; Fang, F.; Opila, R. L. *Acs Appl Mater Inter* **2010,** 2, (11), 3170-3178.

6. Avila-Marin, A. L. *Sol Energy* **2011,** 85, (5), 891-910.

7. Clarke, D. R.; Oechsner, M.; Padture, N. P. *MRS Bull* **2012,** 37, (10), 891-902.

8. Padture, N. P.; Gell, M.; Jordan, E. H. *Science* **2002,** 296, (5566), 280-284.

9. Farid, M. M.; Khudhair, A. M.; Razack, S. A. K.; Al-Hallaj, S. *Energ Convers Manage* **2004,** 45, (9-10), 1597-1615.